A Search for the Lepton Flavour Violation Process $e \rightarrow \mu$ via Leptoquarks in $e^{\pm}p$ Scattering with the H1 Detector at HERA

Mudhahir Ismail

March 2005

THE UNIVERSITY
of MANCHESTER

High Energy Group
Department of Physics and Astronomy

A thesis submitted to The University of Manchester for the degree of
Doctor of Philosophy in the Faculty of Science and Engineering

Contents

1 Introduction **21**

2 The H1 Experiment at HERA **24**

2.1 The HERA Storage Ring 24

2.2 The H1 Detector 26

2.2.1 The H1 Coordinate System 28

2.3 Tracking 28

2.3.1 The Central Track Detector 31

2.3.2 The Forward Tracker Detector 33

2.3.3 The Backward Drift Chamber 35

2.4 Calorimetry 35

2.4.1 The Liquid Argon Calorimeter 37

2.4.2 The SpaCal 38

2.4.3 The Plug 39

2.4.4 The Tail Catcher 40

2.5 Muon Detection 41

2.5.1 The Central Muon Detector 42

2.5.2 The Forward Muon Detector 42

2.6 The Time of Flight System 43

2.7 The H1 Luminosity System 46

2.8 The H1 Trigger System and Data Acquisition 47

2.9 Detector Monte Carlo Simulation 49

3 Theoretical Overview 51

3.1 Standard Model 51

3.2 Deep Inelastic Scattering 54

3.2.1 Kinematics 55

3.2.2 Kinematic Reconstruction 58

3.2.3 Cross Section and Structure Functions 60

3.2.4 Scaling Violation and Quantum Chromodynamics 62

3.3 Photoproduction 67

3.4 Lepton Flavour Violation in the SM 68

3.5 Lepton Flavour Violation in BSM Theories 70

3.5.1 LFV in Gauge and Extra Dimension Theories 71

3.5.2 Leptoquarks 71

3.6 LFV Signal Processes 76

3.7 Background Processes 78

3.7.1 Lepton Pair Production 78

3.7.2 Photoproduction 80
3.7.3 Neutral Current 81
3.7.4 Charged Current 82
3.7.5 W Boson Production 82

4 General Data Analysis **85**
4.1 Run Selection and Detector Status 85
4.2 Vertex Position 86
4.3 Rejection of Non-*ep* Background 86
4.4 Trigger Selection 87
4.4.1 LAr Trigger 88
4.4.2 Muon Trigger 89
4.5 Particle Identification 90
4.5.1 Muon Identification 90
4.5.2 Electron identification 91
4.5.3 The Hadronic System 92

5 Kinematic Variables and Background Processes **94**
5.1 P_T^{calo} 95
5.2 P_T^X 97
5.3 P_T^μ 97
5.4 P_T^{miss} 99

5.5 Acoplanarity 99

5.6 $\frac{V_{ap}}{V_p}$ 100

5.7 D_{jet} and D_{track} 103

5.8 θ^{μ} and θ^{X} 103

5.9 Reconstructed Mass 106

6 Isolated Muon Selection **110**

6.1 Selection Criteria 110

6.2 Discussion 111

6.3 Results 122

7 $LQ \to \mu + X$ Selection **124**

7.1 Selection Criteria 124

7.2 Discussion 129

7.3 Selection Efficiency 134

7.3.1 Low mass LQs 134

7.3.2 LQs with masses $\gg \sqrt{s}$ 137

8 Interpretation **141**

8.1 Systematic Uncertainties 141

8.2 Limit Procedure 143

8.2.1 Confidence Level 143

8.2.2 The Modified Frequentist Approach 144

8.3 Limit Results 145

8.3.1 Low mass LQs 145

8.3.2 LQs with masses $\gg \sqrt{s}$ 149

9 Conclusions and Future Work **153**

9.1 Conclusions 154

9.2 Future Work 155

9.2.1 Future Potential 155

Bibliography **155**

List of Figures

2.1 The HERA accelerator with all four experiments (left) and an enlarged view of the PETRA pre-accelerator complex (right). 25

2.2 A 3D cut-away view of the H1 Detector 27

2.3 A longitudinal view of the H1 tracking system. 30

2.4 A transverse view of the H1 central tracking system. 31

2.5 A longitudinal view of the FTD (top). A transverse view of the FTD showing all its components (bottom). 34

2.6 A longitudinal view of the LAr (top). A transverse view of the LAr showing all eight sections (bottom). 38

2.7 One layer of LST in the Tail Catcher. A single wire is pictured in the middle of each tube. 40

2.8 A transverse view of the Instrumented Iron (top) and its structure showing the pads and strips used in the hadron and muon detection (bottom). 41

2.9 (a) A side view of the FMD system with its drift chambers and the toroidal magnet. (b) A theta chamber of the FMD. (c) Particle passage through two different cells. 43

2.10 The location of the ToF scintillators and Veto Walls. 44

2.11 Beam gas (top) and beam halo (bottom) event displays. 45

2.12 The H1 Luminosity system. 47

2.13 A schematic view of the H1 trigger system. 48

3.1 Left: NC process. Right: CC process. In the NC process the electron scatters with momentum k' and the exchanged boson is a photon or Z. The exchanged boson in the CC process is W and the scattered particle is a neutrino. 56

3.2 The differential cross section of the NC and CC processes for e^-p and e^+p interactions. Both processes have higher cross sections in the e^-p interactions at high Q^2 than the e^+p interactions. 62

3.3 The $F_2(x, Q^2)$ structure function distribution as a function of Q^2 with different values of x for different experiments. 63

3.4 The gluon density distribution with respect to x. 65

3.5 Plots of the pdfs of the proton using CTEQ5 for different quark contributions. As x increases the pdfs decrease steeply. 65

3.6 (a) Quark splitting into gluon and quark. (b) Gluon splitting into two quarks. 66

3.7 Left: Direct photoproduction process. Right: Resolved photoproduction process. 67

3.8 Feynman diagram for $\mu \to e\gamma$. 70

3.9 Left: s-channel LFV process. Right: u-channel LFV process. Positron (electron) interacts with a valence quark in the s-channel and with a sea antiquark in the u-channel. The LQ in both channels is of $F = 0$ ($F = 2$) type. A sea quark can be involved in the s-channel and a valence quark in the u-channel. 72

3.10 $LQ \to \mu + q$ MC event display in transverse (top) and radial (bottom) views. 77

3.11 Lepton pair process. 78

3.12 Lepton pair event display. The two muons in this event have escaped the LAr through the central and forward muon systems. A muon is also visible in the hadronic final state. 79

3.13 Photoproduction event display. The scattered electron is tagged in the ET and particles from the two jets are absorbed in the hadronic and electromagnetic LAr. 80

3.14 Neutral Current event display. The electron is absorbed in the electromagnetic part of the LAr whereas the jet is absorbed in the hadronic and electromagnetic parts of the LAr. 81

3.15 Charge Current event display. Particles produced in the hadronic shower are deposited in the LAr. 82

3.16 W production Feynman diagram. 83

3.17 W production event display. The muon escapes the LAr and traverses through the FMD system. 84

4.1 Cosmic muon traversing the detector. 87

4.2 LAr trigger efficiency for Pseudo CC data and MC simulation in P_T and polar angle of the hadronic system. 89

4.3 Efficiency of trigger elements used for muon triggering as a function of P_T^{μ} (top) muon polar angle (bottom): muon barrel trigger (left), endcaps muon trigger (middle) and muon trigger signals from endcaps or barrel (right). 90

5.1 Distributions of P_T^{calo} after the muon selections for e^-p (left) and e^+p (right) collisions. Since the muons barely deposit their energy into the calorimeters they do not contribute very much to this quantity. The SM expectation falls steeply with P_T^{calo}. Most background processes have low P_T^{calo}. 96

5.2 P_T^X distributions after the muon selections for e^-p (left) and e^+p (right) collisions. This looks similar to the P_T^{calo} (Figure 5.1) especially for the signal MC. In P_T^X the track information is included in contrast to P_T^{calo} which makes them similar in the case of the LQ signal which contains an isolated muon. 98

5.3 P_T^{μ} distributions after the muon selections for e^-p (left) and e^+p (right) collisions. The P_T^{μ} is calculated from the curvature of the muon track. The SM expectation falls steeply with P_T^{μ}. 98

5.4 P_T^{miss} distributions after the muon selections for e^-p (left) and e^+p (right) collisions. Most W-decay (EPVEC) and CC (DJANGO) events have high P_T^{miss} values since they contain neutrinos in the final state. 100

5.5 Acoplanarity, $\Delta\phi_{\mu-X}$, is defined as the angle between the muon and the hadronic system in $r-\phi$. 101

5.6 $\Delta\phi_{\mu-X}$ distribution after the muon selections for e^-p (left) and e^+p (right) collisions. The lepton pair (GRAPE+EPJPSI) events show a peak at about 180° indicating that the highest P_T^μ muon balances the hadronic final state in the final state. The smaller peak at very low angles are for events with no jets. 101

5.7 $\frac{V_{ap}}{V_p}$ distribution after the muon selections for e^-p (left) and e^+p (right) collisions. The lack of isotropy in the LAr can be seen in the lepton pair (GRAPE+EPJPSI), CC (DJANGO) and W-decay (EPVEC) events which contain particles which escape the LAr in their final state such as neutrions and muons. Selecting events with $\frac{V_{ap}}{V_p} < 0.3$ removes the majority of background events coming from photoproduction (PYTHIA+AROMA) and NC (RAPGAP) processes as will be described in the next chapter. 102

5.8 D_{jet} (top) and D_{track} (bottom) distributions after the muon selections for e^-p (left) and e^+p (right) collisions. The lepton pair (GRAPE+EPJPSI) events show a peak at around π in the D_{jet} and D_{track} since the highest P_T^μ and the hadronic system are back-to-back. 104

5.9 θ^μ (top) and θ^X (bottom) distributions after the muon selections for e^-p (left) and e^+p (right) collisions. 105

5.10 LQ mass distribution for e^+p at mass = 250 GeV reconstructed using the double angle method after the muon selections. The broad peak can be understood from a convolution of the Breit-Wigner distribution of the LQ mass with the pdf of the proton. It is caused by the resonantly produced LQ events from the incoming leptons and the sea quarks which have low Bjorken-x values. A high coupling constant was used to generate the LQ. Compare this with plots on the next page. This shows the effect of the coupling constant on LQ masses near the kinematic limits. 108

5.11 Different LQ mass distributions for e^-p at masses = 150, 250 and 350 GeV reconstructed using the double angle method after the muon selections. The broad peak for the LQ of mass 350 GeV shows that the LQ is produced from the tail of the Breit-Wigner distribution accessible into the kinematic region. The 350 GeV mass corresponds to $x > 1$ (Eq. 5.4) and hence cannot peak at the generated value. . . 109

6.1 P_T^{calo} distributions after the isolated muon selections for e^-p (left) and e^+p (right) collisions with scalar and vector LQs respectively. . . 112

6.2 P_T^X distributions after the isolated muon selections for e^-p (left) and e^+p (right) collisions. The LQ mass is 250 GeV. 113

6.3 P_T^X distributions after the isolated muon selections for e^-p collisions. The LQ generated mass is 350 GeV. 113

6.4 P_T^μ distributions after the isolated muon selections for e^-p (left) and e^+p (right) collisions. 114

6.5 P_T^μ distributions after the isolated muon selections for e^-p collisions. 115

6.6 P_T^{miss} distributions after the isolated muon selections for e^-p (left) and e^+p (right) collisions. 115

6.7 P_T^{miss} distributions after the isolated muon selections for e^-p collisions. 116

6.8 $\Delta\phi_{\mu-X}$ distributions after the isolated muon selections for e^-p (left) and e^+p (right) collisions. The smaller peak at very low angles are for events with no jets. 116

6.9 $\frac{V_{ap}}{V_p}$ distributions after the isolated muon selections for e^-p (left) and e^+p (right) collisions. 117

6.10 $\frac{V_{ap}}{V_p}$ distributions after the isolated muon selections for e^-p collisions. The signal distribution is for a LQ with a mass of 350 GeV. 118

6.11 D_{jet} (top) and D_{track} (bottom) distributions after the isolated muon selections for e^-p (left) and e^+p (right) collisions. 119

6.12 θ^μ (top) and θ^X (bottom) distributions after the isolated muon selections for e^-p (left) and e^+p (right) collisions. 120

6.13 θ^μ (left) and θ^X (right) distributions after the isolated muon selections for e^-p collisions. The LQ signals are for mass 350 GeV. 121

6.14 250 GeV V_0^L LQ mass distribution reconstructed using the double angle method after the isolated muon selections. 121

7.1 P_T^{calo} distributions after the final selections for e^-p (left) and e^+p (right) collisions. 125

7.2 P_T^{miss} distributions after the final selections for e^-p (left) and e^+p (right) collisions. 127

7.3 P_T^X distributions after the final selections for e^-p (left) and e^+p (right) collisions. 127

7.4 P_T^μ distributions after the final selections for e^-p (left) and e^+p (right) collisions. 128

7.5 $\Delta\phi_{\mu-X}$ distributions after the final selections for e^-p (left) and e^+p (right) collisions. 128

7.6 $\frac{V_{ap}}{V_p}$ distributions after the final selections for e^-p (left) and e^+p (right) collisions. 129

7.7 D_{jet} (top) and D_{track} (bottom) distributions after the final selections for e^-p (left) and e^+p (right) collisions. 130

7.8 θ^μ (top) and θ^X (bottom) distributions after the final selections for e^-p (left) and e^+p (right) collisions. The signal events are for LQs with 250 GeV. 131

7.9 θ^μ (left) and θ^X (right) distributions after the muon selections for e^-p collisions. The signal events are for LQs with 350 GeV. 132

7.10 Different LQ mass distribution reconstructed using the double angle method after the final selections. 133

7.11 Selection efficiencies for different LQs which may be produced in e^-p collisions after the final selections as a function of mass. 135

7.12 Selection efficiencies for different LQs which may be produced in e^+p collisions after the final selections as a function of mass. 136

8.1 Exclusion limits from H1 (top) on λ_μ in terms of mass for scalar (right) and vector (left) LQs in e^-p interactions compared to ZEUS (bottom) taken from [87] for $\tilde{S}_0^R$ (left) and $V_{1/2}^L$ (right) LQs. The brackets show the quark(s) in the incoming proton contributing to the LQ formation. The ZEUS limits are for LQs between 140 and 300 GeV. H1 and ZEUS limits are very comparable for low mass LQs. 147

8.2 Exclusion limits from H1 (top) on λ_μ in terms of mass for scalar (left) and vector (right) LQs in e^+p interactions compared to ZEUS (bottom) taken from [87] for $\tilde{S}^L_{1/2}$ (left) and V^R_0 (right) LQs for 1994-2000 data with $\mathcal{L} = 113$ pb^{-1}. The brackets show the quark(s) in the incoming proton contributing to the LQ formation. The ZEUS limits are for LQs between 140 and 300 GeV. H1 and ZEUS limits are very comparable for low mass LQs. 148

8.3 Branching ratio limit of all LQs involved in the e^-p (left) and e^+p interactions (right) at 95% CL in terms of mass for LQ $\rightarrow \mu q$ with a fixed coupling to first generation leptons at electromagnetic coupling constant strength, $\lambda_{eq} = 0.3$. 149

List of Tables

3.1 Fundamental fermions in the SM 52

3.2 The fundamental gauge bosons in the SM. Q_{em} is the electromagnetic charge, J in J^P is the spin of the particle and P is the parity. 53

3.3 The 14 LQ types in the BRW model. The second and third column show the Aachen and the original BRW nomenclature for LQ classification, respectively. The other columns show the electrical charge for the LQs, the third component of the weak isospin, the hypercharge (where $Y = 2 \times (Q - T_3)$), the fermion number, the production and decay channels, the relative coupling strengths and the branching ratios into $l^{\pm}q$ respectively. The subscript in the Aachen nomenclature indicates the isospin of the LQ and the superscript refers to the incoming lepton helicity. S is used for scalar (spin 0) LQs and V (spin 1) for vector LQs. The information here are given for e^+p collisions. The production channels are s-channel. 74

6.1 Selections applied in the second level selection to select isolated muon events. First level selections (P_T^{calo}, P_T^{μ}, θ^{μ}) which were dedicated to selecting muon events are included in this set. 111

6.2 Number of events for each SM MC process and data for the e^-p and e^+p interactions after applying the isolated muon cuts. 123

7.1 Cuts applied in the final level selection to select LFV events. Second level selections which were dedicated to selecting isolated muon events are included in this set. Top: Number of events after each cut for data and SM expectation for both e^-p and e^+p collisions. Bottom: Selection efficiencies (Section 7.3) after each cut for vector LQs one with a mass below the kinematic limit and one with a mass above the kinematic limit. 126

7.2 Number of events for each SM MC process and data for the e^-p and e^+p interactions after applying the final selections. 132

7.3 Selection efficiencies of $F = 0$ (top) and $F = 2$ (bottom) LQs coupling to the first, second and third quark generations for e^-p interactions. The dashes represent scenarios involving a top quark. 139

7.4 Selection efficiencies of $F = 0$ (top) and $F = 2$ (bottom) LQs coupling to the first second and third quark generations for e^+p interactions. The dashes indicate scenarios involving a top quark. 140

8.1 Number of events for each MC process and data for the e^-p and e^+p interactions after applying the final selections. The errors include all uncertainties described in the text. 142

8.2 First row: Most stringent limits from low energy experiments; Second row: ZEUS limits for 1994-2000 ($e^\pm$) interactions; Third row: H1 limits for 1998-2000 ($e^\pm$) interactions giving a total integrated luminosity of 80.8 pb^{-1} for $F = 0$ type LQs. The ZEUS limits are more stringent because they include the 94-97 data as well giving a total integrated luminosity of 129.9 pb^{-1}. The cases marked with '$*$' refers to scenarios involving a top quark. 151

8.3 First row: Most stringent limits from low energy experiments; Second row: ZEUS limits for 1994-2000 ($e^{\pm}$) interactions; Third row: H1 limits for 1998-2000 ($e^{\pm}$) interactions with a total integrated luminosity of 80.8 pb^{-1} for $F = 0$ type LQs. The ZEUS limits are more stringent because they include the 94-97 data as well with a total integrated luminosity of 129.9 pb^{-1}. The cases marked with '$*$' refers to scenarios involving a top quark. 152

Abstract

A search for lepton flavor violation (LFV) processes mediated by leptoquarks (LQs) is performed with the H1 experiment at HERA. Final states with a muon and a hadronic jet are searched for in a data sample collected in the period 1998-1999 corresponding to an integrated luminosity of 13.8 pb^{-1} for e^-p collisions and in the period 1999-2000 corresponding to an integrated luminosity of 66.0 pb^{-1} for e^+p collisions both with a centre of mass energy of 319 GeV. No evidence for LFV is found. Limits are derived at 95% confidence level (CL) on the Yukawa coupling of LQs to a muon and a light quark, $\lambda_{\mu q}$, in the Buchmüller-Rückl-Wyler effective model, as well as on the branching ratio, $BR_{\mathrm{LQ}\to\mu q}$, for the LQ decaying to a muon and a light quark. For leptoquarks with masses far beyond the centre of mass energy limits at 95% CL are also set on the four fermion contact interaction term, $\frac{\lambda_{eq_i}\lambda_{\mu q_i}}{M_{LQ}^2}$, and compared to the low energy experiment limits.

No portion of the work referred to in this thesis has been submitted in support of an application for another degree or qualification of this or any other university or other institute of learning.

Chapter 1

Introduction

HERA is the only collider in the world which produces high energy *ep* collisions. These collisions allow one to study the structure of the proton and to test quantum chromodynamics. It also enables the electroweak sector of the Standard Model to be tested. Any *ep* collision is expected to end with an electron or a neutrino in the final state. A deviation from this expectation might be a sign for lepton flavour violation. Lepton number is conserved in the Standard Model for massive leptons. However, there is no clear theoretical reason for this conservation especially since the conservation is not observed in the neutrino sector.

This thesis presents a search for muons resulting from lepton flavour violation in data collected between 1998 and 1999 for electrons colliding with protons and between 1999 and 2000 [1] for positrons colliding with protons. The centre of mass energy for both interaction types is 319 GeV.[2] The corresponding integrated luminosities are $\mathcal{L} =$ 13.8 pb^{-1} and $\mathcal{L} =$ 66.0 pb^{-1} for the e^-p and e^+p samples, respectively. A similar search has been performed and published for the 1994-1997 data with a centre of mass energy of 300 GeV [2]. The results of the new e^+p data have already

---

[1] Data collected up to 2000 are termed HERA I data and data collected after 2000 are termed HERA II data.

[2] Throughout this thesis natural units are used where $\hbar = c = 1$.

been accepted as preliminary by the H1 collaboration and were presented at the ICHEP04 conference [1].

One way to check for lepton flavour violation is to search for leptoquarks (LQs) mediating ep interactions and decaying into a muon or tau in the final state. The LQs considered here are based on the Büchmuller-Rückl-Wyler model. Any LQ in this model can be produced resonantly by one interaction type. For masses below the centre of mass energy any LQ signature has a clear peak at its mass. Half of the fourteen LQ types can be produced resonantly by the e^-p interaction and the other half by the e^+p interaction. For higher mass LQs only the tail of the mass distribution which extends below the kinematic limit is visible. For masses far beyond the kinematic limits ($\sim$ 1 TeV) both e^-p and e^+p collisions can access any LQ type through virtual exchange. No signal in the data has been found which indicates lepton flavour violation. Direct exclusion limits have been set for the low mass region. Limits on the four fermion interaction term have been set on all LQ types for both interactions.

Thesis Content

The thesis is organised as follows:

- Chapter 2 describes the components of the H1 detector relevant to this search.
- Chapter 3 gives an introduction to the Standard Model and describes the motivations for a lepton flavour violation search. An overview of the theory relevant to ep collisions is followed by a description of LQ phenomenology.
- Chapter 4 introduces the basic selection criteria applied to all subsequent selections. This is followed by a description of the particle identification techniques.
- Chapter 5 explains the variables used to describe the LQ kinematics after the first level selection. This selection is dedicated to selecting events with muons.

- Chapter 6 shows the control plots after applying a second level of selection dedicated to selecting *isolated* muons.
- Chapter 7 explains the final selections applied to select events containing muons from LQ decay. Finally, the efficiencies for selecting different LQ types and masses are presented.
- Chapter 8 explains the systematic uncertainties taken into account in the search and then introduces the limit techniques used to calculate the limits on the lepton flavour violation process.
- Chapter 9 concludes this thesis. Possible future searches are also mentioned.

Chapter 2

The H1 Experiment at HERA

In this chapter the electron[1]-proton collider HERA (Hadron Electron Ring Anlage) at DESY (Deutsches Elektron Synchrotron) in Hamburg is introduced. A brief description of the HERA storage ring is followed by an overview of the main H1 detector components. The details of the H1 detector components are described in [3].

2.1 The HERA Storage Ring

The HERA collider consists of two accelerators in an approximately circular tunnel with a circumference of 6.3 km and at a depth of 10-15 m below the ground surface. As can be seen in Figure 2.1, electrons are accelerated in the clockwise direction up to 27.6 GeV and protons are accelerated in the anti-clockwise direction. The HERA collider was in operation from 1992 until 1997 with a proton beam energy of 820 GeV. In 1998 the proton beam energy was increased to 920 GeV resulting in an increase of centre of mass energy ($\sqrt{s}$) from 300 GeV to 319 GeV.

---

[1] The term electron will be used to refer generically to e^- or e^+, unless otherwise stated.

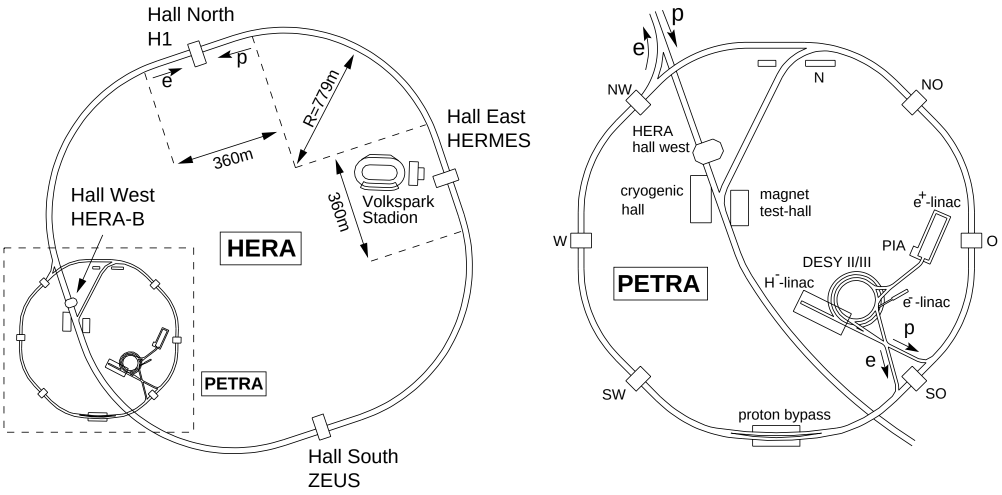

Figure 2.1: The HERA accelerator with all four experiments (left) and an enlarged view of the PETRA pre-accelerator complex (right).

The electron and proton beams collide in two interaction regions located at the North and South Halls. Around these interaction regions the H1 (North) and ZEUS (South) experiments are installed to study *ep* collisions. In addition, two fixed target experiments called HERMES and HERA-B are located in the East and West halls respectively. The HERMES experiment utilises the polarised electron beam and collides it with polarised gas targets (H_2, D_2, He) to investigate the spin structure of nucleons (protons and neutrons). The HERA-B experiment was built to investigate charge-parity (CP) violation in $\bar{B}^\circ B^\circ$ pairs formed from the interaction of the proton beam halo with nucleons of a tungsten wire target.

Figure 2.1 shows the different experiments described above and the PETRA pre-accelerator complex where both beams are initiated, accelerated and accumulated before they are injected into the HERA main accelerator. Each beam is made up of 220 bunches containing 10^{10} to 10^{11} particles each and crossing every 96 ns at the interaction points. Of the total 220 bunches only $\sim$ 175 are used in collisions whereas the remaining bunches, called pilot bunches, are employed to study background rates induced by the interaction of the beam with the beam pipe, the so-called beam-pipe interaction, or with the residual beam gas, called beam-gas interaction.

A positron beam (e^+) was used in the period 1994-97. In 1998 HERA operated with an electron beam (e^-). Between summer 1998 and autumn 2000 positrons were again collided with the protons.

From September 2000 until July 2002, HERA operation was stopped for an extensive upgrade of the accelerator and the experiments. The aim was to upgrade the luminosity and hence the focusing of the beam currents in the interaction region was increased. To achieve this, superconducting quadrupole focusing magnets were installed within the H1 and ZEUS detectors. In addition, spin rotators were installed before and after the interaction region to provide a longitudinally polarised electron beam.

2.2 The H1 Detector

The H1 detector, situated in the North Hall of the HERA ring, is a multi-purpose detector to study many aspects of high energy electron-proton scattering. It weighs $\approx$ 2800 tonnes and measures roughly 12m × 10m × 15m. A 3D cut-away view of the H1 detector is shown in Figure 2.2. Protons enter the detector from the right and electrons from the left and the two beams are focused to meet each other at a point known as the *interaction point* (IP). Since the proton beam enters with an energy much higher than the electron beam, the centre of mass energy of the *ep* collision is boosted along the proton direction. Therefore, the detector design is very asymmetric and more highly instrumented in the proton direction. In addition, the H1 detector provides almost complete coverage in solid angle (4π) around the interaction point to enable the detection of particles produced from the *ep* interaction. The main acceptance loss comes from the beam pipe.

To detect particles produced from the interaction, several instruments surround the

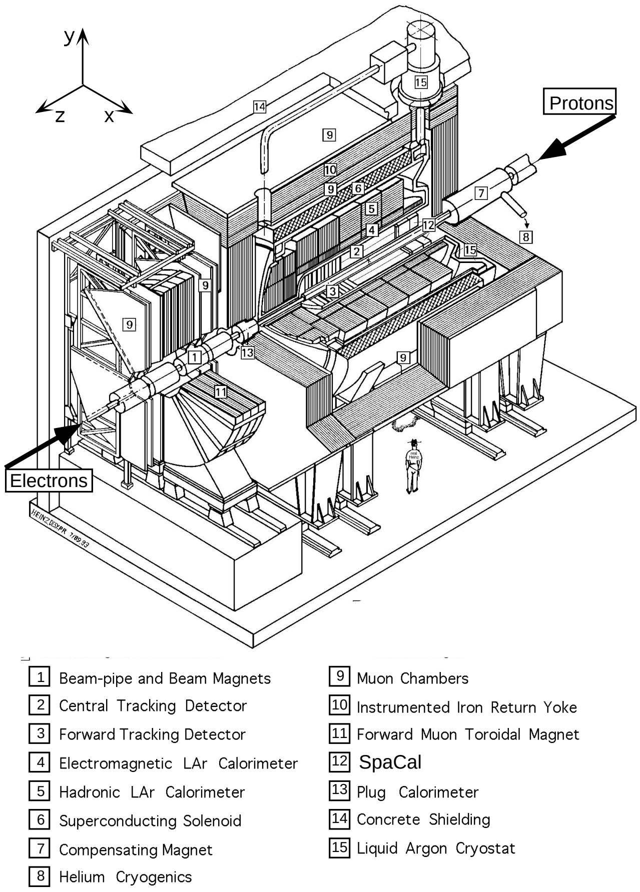

Figure 2.2: A 3D cut-away view of the H1 Detector

beam pipe. Around the interaction point lie the tracking detectors which consist of central and forward tracking systems each with drift chambers and proportional chambers. The tracking detectors are surrounded by the liquid argon calorimeter (LAr) consisting of the electromagnetic and hadronic calorimeters, which are used to identify electrons and hadrons respectively. The calorimeters are also employed to measure the energy and position of neutral and charged particles by absorbing the energy of almost all incident particles. A side view of the H1 detector shows that the LAr has a horse-shoe shape in order to contain particles boosted in the proton beam direction. The LAr is surrounded by a superconducting solenoid with a diameter of 6 m and length of 5.75 m to provide an almost uniform magnetic field of 1.15 T parallel to the beam axis. This allows the measurement of particle momenta from their radius of curvature and charge from the direction of curvature. The whole detector is encased in a layer of instrumented iron to provided the return yoke for the magnetic field. The iron return yoke is laminated and filled with streamer tubes to measure hadronic energy leakage from the LAr. Muon tracks are also identified and their direction measurement is achieved by these streamer tubes. An additional detector outside the iron containing a toroidal magnet sandwiched between drift chambers is used to identify muons boosted in the forward direction with respect to the proton beam.

2.2.1 The H1 Coordinate System

Points within the H1 detector are described using a right handed Cartesian coordinate system with the nominal interaction point defined as the origin, $+x$ pointing towards the centre of the HERA ring, $+y$ pointing vertically upwards and $+z$ pointing in the direction of the incoming proton beam (also know as the "forward" direction). The (x, y)-plane is referred to as the transverse plane. The polar angle θ is defined with respect to the proton beam direction so that $\theta = 0°$ is in the proton direction and $\theta = 180°$ is in the electron direction (also know as the "backward" direction). The azimuthal angle, $\phi = 0°$, points along the x-direction.

2.3 Tracking

The tracking system of H1 was designed to give an accurate measurement of the transverse momentum of charged particles below 25 GeV. It also helps in separating very closely spaced charged particles inside jets of hadrons. Its main task is to provide track triggering, reconstruction and particle identification and it covers the angular range $5^\circ < \theta < 178^\circ$ with full azimuthal angular acceptance.

Measurement of the track of charged particles through the detector is made using three different types of tracking detectors: Drift chambers to provide an accurate reconstruction, multiwire proportional chambers (MWPCs) which are used for triggering because of their fast read out time and silicon strip detectors which aid the identification of primary and secondary vertices and track measurement at high polar angles.

Drift Chambers consist of cells which are filled with gas and contain anode sense wires and cathode field wires. A nearly uniform electric field is created by applying a high voltage to the cathode. When a charged particle passes through the chamber the ionised electrons in the gas *drift* towards the anode wires whereas the positive ions drift toward the cathode wires. The drift occurs at a nearly constant speed known as the drift velocity. Near the anode wires the electric field is greater and hence as the electron approaches the wire secondary collisions with the gas atoms are induced releasing more electrons. This avalanche of electrons induces a current and hence a pulse along the wires. Using the information of the pulse timing and the drift velocity the original position where the initial ionisation took place can be calculated.

MWPCs are similar to drift chambers except that they consist of many closely spaced anode wires lying between cathode wires. When a charged particle passes through the gas the gas atoms are ionised. Because the anode wires are closely spaced the electrons drift towards the closest anode wire and as a consequence secondary ionisations are induced due to the high field strength and the electron collisions. The signal received is proportional to the initial ionisation. The readout pads are located around the outside of the cells and form the cathode. Because the signals received on the anode wires have a fast read out time, $\mathcal{O}(10 \text{ ns})$, they are used for triggering.

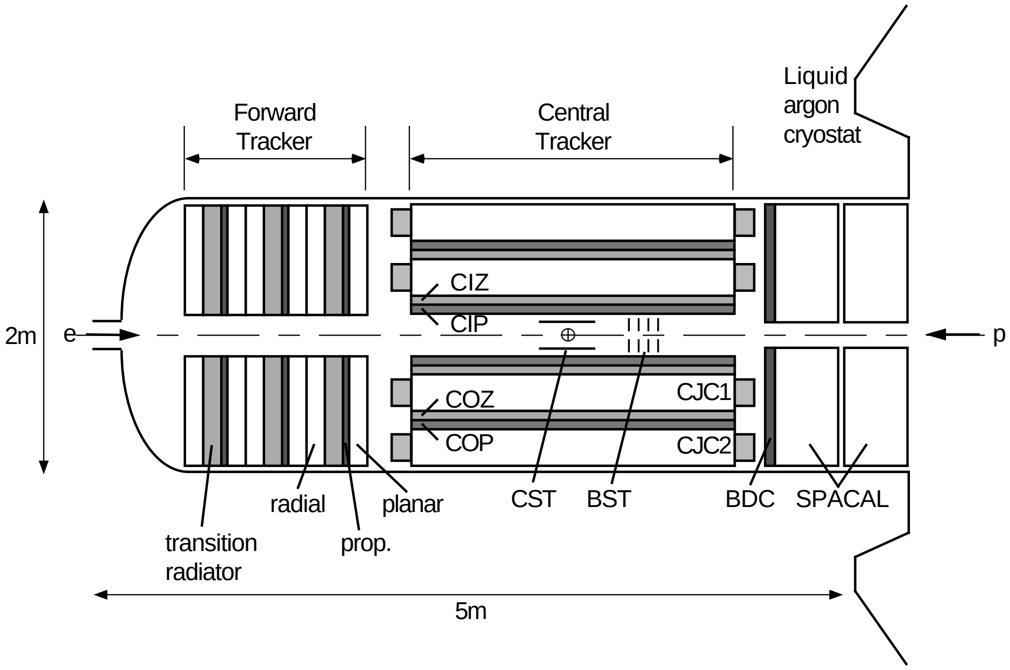

Figure 2.3: A longitudinal view of the H1 tracking system.

The tracking system of H1 is shown in Figure 2.3. As previously mentioned (Section 2.2) the whole system is contained within the magnetic field of the solenoid which enables the momentum measurement of charged particles. The tracking detector is divided into two regions: the central (CTD) and forward (FTD) track detectors to maintain good efficiency for triggering and reconstruction since the particles generated from the ep collisions are not symmetrically distributed in z around the interaction point. Both these detectors contain drift chambers and MWPCs. As shown in Figure 2.4, the central region around the beam pipes contains the following detectors:

- Central Inner Proportional Chambers (CIP).
- Central inner z-Chamber (CIZ).
- Central Jet Chamber 1 (CJC1).

- Central outer z-Chamber (COZ).
- Central Outer Proportional chamber (COP).
- Central Jet Chamber 2 (CJC2).

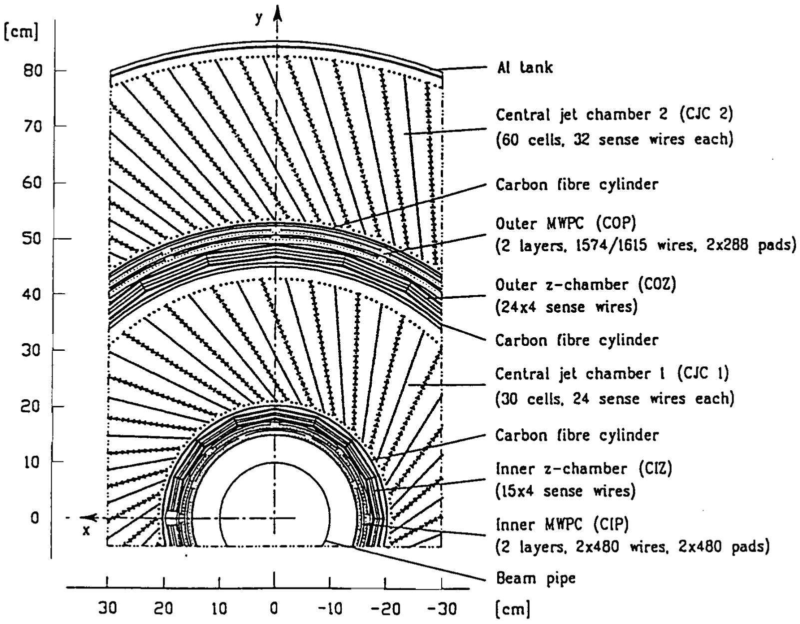

Figure 2.4: A transverse view of the H1 central tracking system.

The Backward Drift Chamber (BDC) provides extra track reconstruction in the backward region.

2.3.1 The Central Track Detector

The CTD cover a polar angular range of $15° \leq \theta \leq 165°$. In this section a detailed description of the CTD is given.

The Central Proportional Chambers

The CIP and COP [4] are multiwire proportional chambers, each consisting of two layers. The sense wires of the CIP and COP run parallel to the beam-pipe. Their main purpose is to deliver fast timing signals which are used for fast trigger information about tracks coming from the nominal interaction vertex. Their time resolution is 21 ns obtained from test beam studies.

The Central Jet Chambers

The main detectors in the CTD are CJC1 and CJC2 [5]. Both chambers have a length of 2.2 m. These are drift chambers with anode sense wires parallel to the beam axis resulting in a best measurement of tracks in the $r - \phi$ plane. The wire signal induced by a charged particle allows a resolution measurement of $\sigma_{r\phi} = 140$ μm whereas the measurement of z by sampling the pulse at both ends of the wire using the charged division technique [6] yields a coarse resolution of $\sigma_z = 2.2$ cm. The CJC1 (CJC2) is divided into 30 (60) cells with 24 (30) sense wires in each cell. Each cell is tilted by 30° with respect to the radial line. This ensures that in the presence of the magnetic field the electrons drift approximately perpendicular to stiff, high momentum tracks which originated from the IP. The electron is subject to two forces due to the electric and magnetic fields and hence it is deflected due to the magnetic field from the path of the electric field lines. This deflection angle is called the Lorentz angle. The drift velocity direction of the electron is never far from perpendicular to the track. Each stiff track will then cross at least one of the cells. By connecting track segments of different cells, spatial drift chamber track reconstruction ambiguities are avoided. Two potential wires are placed between two adjacent sense wires to reduce the possibility of cross-talk between neighbouring sense wires. In addition, tracks coming from different bunch crossings can be distinguished from the time the drifting electrons take to reach the wire plane, which is around 50 ns.

To eliminate left-right ambiguity of track segments the sense wires are staggered off the sense wire plane by 150 μm.

The Central z-Chambers

As is shown in Figure 2.4 the CIZ [7] fits inside CJC1 and the COZ chamber fits between CJC1 and CJC2. CIZ and COZ cover the polar angular range range $16^\circ < \theta < 169^\circ$ and $25^\circ < \theta < 156^\circ$ respectively. The CIZ is a 16 sided polygon with 15 cells and the COZ forms a 24 sided polygon with 23 cells. In contrast to the CJCs, the sense wires in the z-chambers are perpendicular to the beam axis to provide a better resolution of 300 μm in the z-coordinate measurement than that obtained from the charge division method used in the CJC.

2.3.2 The Forward Tracker Detector

The Forward Tracker Detector (FTD) [8] depicted on the left hand side of Figure 2.3 covers the polar angular range $7^\circ < \theta < 25^\circ$. It consists of three identical supermodules. Each supermodule is composed of: Planar Drift Chambers, MWPCs, Transition Radiators and Radial Drift Chambers. Details of the FTD supermodule components are pictured in Figure 2.5.

Each supermodule contains three adjacent planar drift chambers located closest to the central trackers because of their homogeneous spatial precision in x and y which is suitable for linking to tracks in the centre. The wires run parallel to each other and perpendicular to the beam pipe. Each planar chamber contains 32 cells, each containing 4 wires staggered alternately by 300 μm each side of the median plane of the cell. The Planar Drift Chambers are rotated at 60° to each other.

The Forward MWPCs (FMWPCs) are mounted directly after the planar drift chambers and provide fast triggering in the forward region. The Radial Chambers are located after the Transition Radiators and are divided into 48 sectors each having

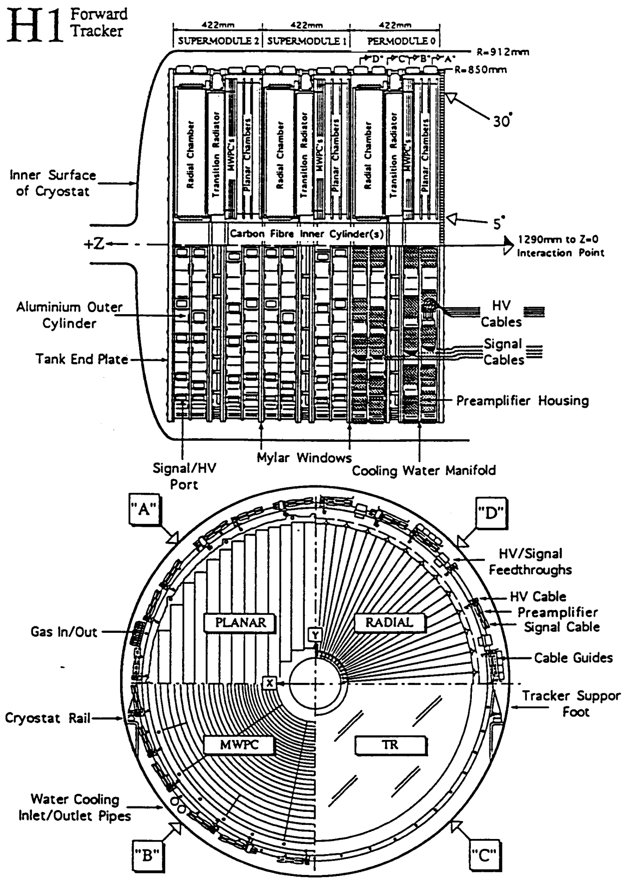

Figure 2.5: A longitudinal view of the FTD (top). A transverse view of the FTD showing all its components (bottom).

12 sense wires staggered alternately by 287 μm each side of a plane bisecting the sector. The wires are strung perpendicular to the beam pipe and radiate outwards from it. Photons produced in the Transition Radiator section are detected in the Radial Chambers. Twelve accurate space points from ionisation drift timing are produced by the Radial Chambers and the charge division method is used since the signals are read out at both ends of the wires. This provides accurate $r - \phi$ information and radial measurements.

2.3.3 The Backward Drift Chamber

The BDC [9] was installed after an upgrade in 1995 and is mounted between the SpaCal and the CTD. Its main purpose is to provide accurate track reconstruction in the backward region especially for electrons with high polar angles. The BDC is composed of 8 layers each divided into octants and each octant contains 32 drift cells. Each of these cells contains 32 wires strung perpendicularly to the beam pipe axis to give an accurate z-coordinate measurement.

2.4 Calorimetry

All calorimeters in H1 have the same detection principle. They are all *sampling calorimeters* and consist of a series of absorbing (passive) layers interleaved with sampling (active) layers. They were designed to provide a clear identification and precise measurement of electrons, muons, neutral particles and jets with high particle density.

When a high energy particle enters an absorbing layer it undergoes multiple interactions with the atoms in the layer. This results in secondary particles which interact, in turn, with the next passive layer. Hence, a shower of charged particles is generated through these processes which continues into the active layers. This process continues as the high energy particle passes through the subsequent passive layers until it dissipates its energy through the shower. Charged particles within the shower ionise the constituent atoms in the active layers. Energy produced from this ionisation can be read out as a signal which is proportional to the energy of the original incident particle.

Electrons and photons lose their energy by electromagnetic interaction with the constituent atomic electrons of the absorbing layer. The development of an electromagnetic shower occurs via two processes: bremsstrahlung and pair production.

The resulting shower contains electrons, positrons and photons. The longitudinal progress or the characteristic amount of matter traversed by the shower is called the *radiation length,* X_0. It is defined as the mean distance over which an electron loses all but $1/e$ of its energy or 7/9 of the mean free path of a photon which pair produces electrons.

Hadrons interact with the nuclei of absorbing layers elastically or inelastically. The shower contains pions produced in the nuclear interaction which decay into photons decaying electromagnetically. This is characterised by a sharp peak near the decay interaction point. The secondary charged hadrons are mainly $\pi^{\pm}$-mesons and they interact inelastically giving rise to a broader shower shape.

The characteristic length for the hadronic shower is the nuclear *interaction length* of the absorbing layer, $\lambda_i \approx 35A^{\frac{1}{3}}$, where A is the atomic weight of the layer. This is much larger than the radiation length for the same material resulting in a slow hadronic cascade development compared to the electromagnetic one.

Within H1 there are 4 different calorimeters which together provide a complete solid angle coverage around the interaction point. These are:

- The Liquid Argon (LAr) Calorimeter which covers the forward and central regions.
- The Spaghetti Calorimeter (SpaCal) covering the backward region not covered by the LAr.
- The Plug Calorimeter covering the forward part between the LAr and the beam pipe.
- The Tail Catcher (TC) situated within the iron return yoke.

Details of each of these calorimeters are given in the following sections.

2.4.1 The Liquid Argon Calorimeter

The LAr [10] Calorimeter is the principal component in the calorimetry system in H1. Its main function is to detect electrons, photons and hadronic final states. It covers an angular range of $4^\circ < \theta < 153^\circ$. It is a sampling calorimeter with liquid argon being the active medium. All the constituents of the LAr are incorporated in a cryostat to keep the argon cooled in a liquid form.

The LAr is composed of two sections, an electromagnetic calorimeter where lead is used as a passive layer formed from 2.4 mm thick plates interleaved with a 2.35 mm gap filled with liquid argon, and a hadronic calorimeter where 19 mm thick plates of stainless steel forming the passive layer are separated by a double gap of 2.4 mm liquid argon. The read out pads are within the liquid. Around 30% of the hadronic energy is lost due to nuclear excitation [11]. This is accounted for by software techniques [12].

The LAr is segmented along the z-axis into eight sections called "wheels" as shown in Figure 2.6 (top). Each of these wheels is divided in $r - \phi$ into eight octants, (Figure 2.6 (bottom)). The small regions between wheels and octants contain dead material and are referred to as "cracks". The wheels are named according to their location along the z-axis; BBE (Backward Barrel Electromagnetic Calorimeter), CB1, CB2, CB3 (Central Barrel Calorimeter), FB1, FB2 (Forward Barrel Calorimeter), OF1, OF2 (Outer Forward Calorimeter), IF1 and IF2 (Inner Forward Calorimeter). All of these wheels contain both electromagnetic and hadronic calorimeters except the BBE which is only an electromagnetic calorimeter. The plates are arranged in a perpendicular orientation to the beam pipe in the backward and forward region and parallel to the beam pipe in the central region. This is to ensure that the incident angle of particles from the ep interaction on the absorber plates is always greater than 45°. The LAr is highly segmented into 45000 cells resulting in a fine granularity, which allows for a precise spatial and energy measurement. The depth of the electromagnetic (hadronic) section is $\approx 30X_0$ $(8\lambda_i)$ in the forward region and $\approx 20X_0$

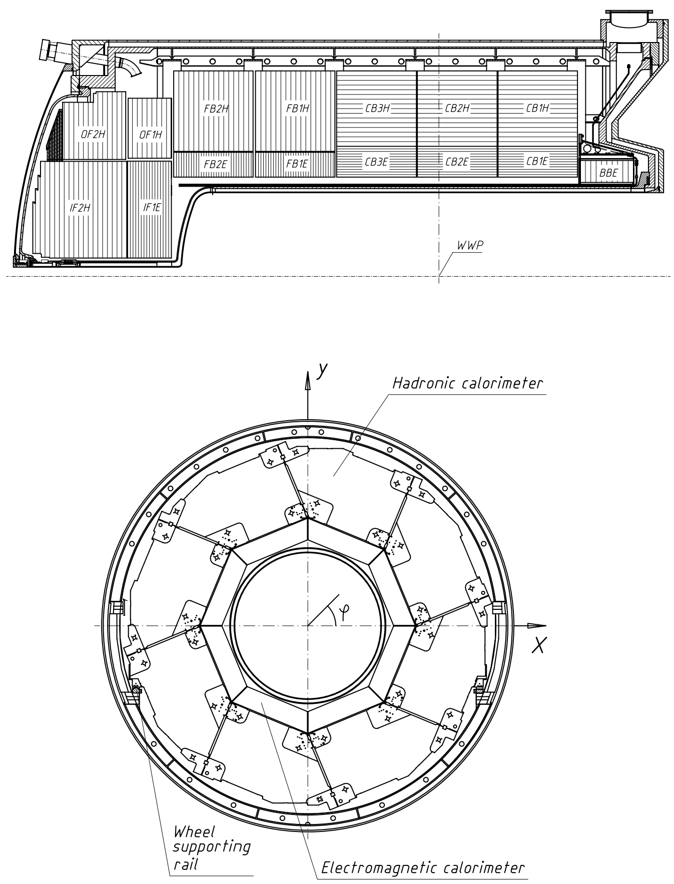

Figure 2.6: A longitudinal view of the LAr (top). A transverse view of the LAr showing all eight sections (bottom).

($5\lambda_i$) in the backward region. Test beam measurements revealed that the energy resolution of electrons in the electromagnetic calorimeter is $\frac{\sigma_E}{E} = \frac{0.12}{\sqrt{E/GeV}} \oplus 0.01$ [13] and of pions in both calorimeters is $\frac{\sigma_E}{E} = \frac{0.50}{\sqrt{E/GeV}} \oplus 0.02$ [14].

2.4.2 The SpaCal

The SpaCal [15], meaning Spaghetti Calorimeter, complements the LAr in the backward region and covers the polar angle range $153° < \theta < 177.8°$. Its main purpose is to measure electron angles and energy efficiently in the backward region. It consists of two sections: electromagnetic and hadronic, each having lead absorbers embedded with scintillating fibers as the sampling material. Light produced in the scintillating fibers due to particle showering in the lead is carried via light guides to photomultipliers where the light signal is read out with a time resolution of 1 ns. This time resolution allows the SpaCal to be used for veto purposes against out of time induced backgrounds (Section 2.6). The depth of the sampling material in both sections is 250 mm corresponding to $28X_0$ or $1\lambda_i$. The signals from the electromagnetic section are read from 1192 individual channels and those from the hadronic section are read from 136 channels. The resolution of the energy measurement of the electrons in the electromagnetic part is $\frac{\sigma_E}{E} = \frac{0.07}{\sqrt{E/GeV}} \oplus 0.01$ [16] and $\frac{\sigma_E}{E} = \frac{0.13}{\sqrt{E/GeV}} \oplus 0.04$ [17] in the hadronic part, obtained from test beam measurements. The hadronic response for the combined sections is established from a charged pion beam and is $\frac{\sigma_E}{E} = 30\%\sqrt{\frac{E}{GeV}}$ [18].

2.4.3 The Plug

The Plug [19] Calorimeter is installed within the instrumented iron in the forward region of the detector. It covers the angular range $0.6^\circ < \theta < 3.5^\circ$ and absorbs the hadrons between the beam pipe and the LAr. The Plug is composed of nine copper absorbing plates interleaved with eight sensitive layers of silicon modules acting as active layers where the signals are read out. The Plug energy resolution is $\frac{\sigma_E}{E} = \frac{1.5}{\sqrt{E/GeV}}$. This resolution is poor due to dead material in front of the calorimeter and shower leakage. The Plug can be used as a veto against beam gas and beam wall background (Section 2.6).

2.4.4 The Tail Catcher

The iron return yoke is instrumented with sixteen limited streamer tubes (LST) [20]. Eleven of these are equipped with read out electrode pads and are used to measure the hadronic energy leakage out of the LAr and the SpaCal. The layout of one of these layers is shown in Figure 2.7. The LSTs are filled with gas and contain a single sense wire. They are fitted with cathode pads perpendicular to the wire running through the centre. The ten iron plates (shown in Figure 2.8) act as the absorbing material. When a charged particle resulting from an interaction in the iron passes through the gas in the tube, due to the high electric field a discharge is caused called a *streamer*. This in turn results in a current in the read out pads. The remaining five of the sixteen layers are used for muon detection (section 2.5). The energy resolution of the tail catcher is found to be $\frac{\sigma_E}{E} = \frac{1.0}{\sqrt{E/GeV}}$ from test beam measurements. The pads provide a coarse spatial resolution of 10 cm.

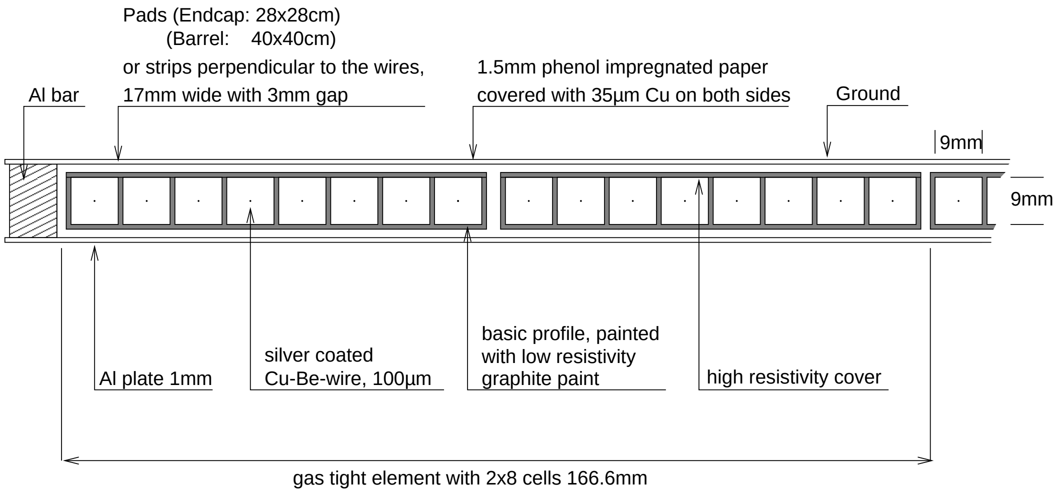

Figure 2.7: One layer of LST in the Tail Catcher. A single wire is pictured in the middle of each tube.

2.5 Muon Detection

Muons barely interact with nuclei and are barely affected by bremsstrahlung and therefore escape the LAr. Muon detection is performed outside the main detector and is divided in two regions: central and forward.

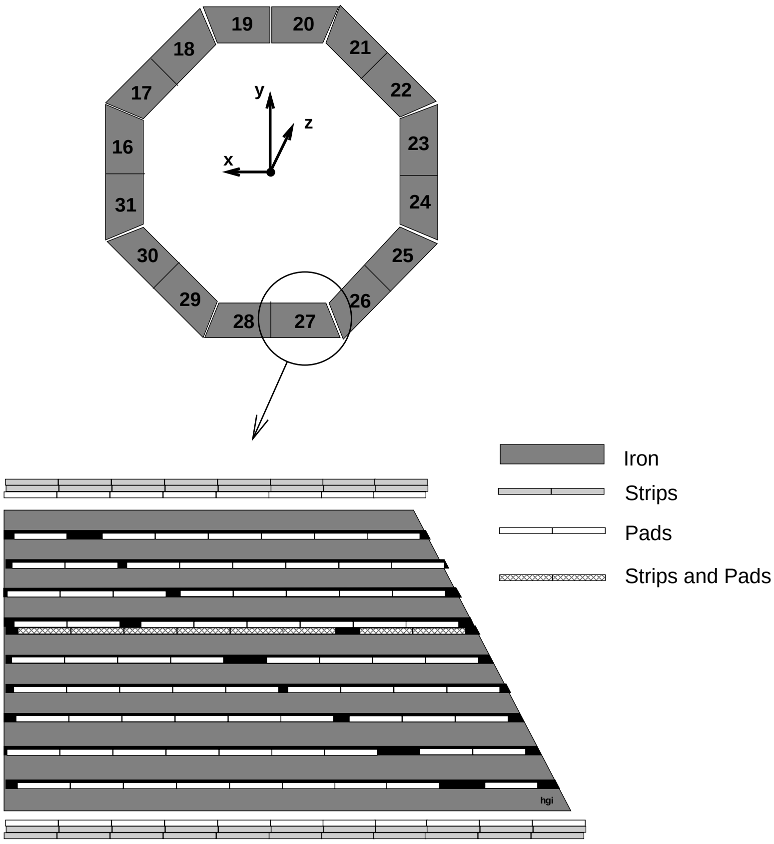

Figure 2.8: A transverse view of the Instrumented Iron (top) and its structure showing the pads and strips used in the hadron and muon detection (bottom).

2.5.1 The Central Muon Detector

Muon detection in the central region benefits from the instrumented iron yoke of the solenoid in the range $5^\circ < \theta < 171^\circ$. Figure 2.8 illustrates the configuration of the muon detection in the instrumented iron. As mentioned in the previous section five LSTs [21] are used for this purpose. These LSTs are fitted with thin metal strips which are perpendicular to the wire running through the centre. These strips are used for the read out signal instead of the cathode calorimeter pads used in the tail catcher as can be seen from Figure 2.8. At both sides of the return yoke three LSTs are located, two of which are strip type and one is a pad LST. The fifth one is in the middle of the iron return yoke. The strips provide a spatial resolution of 10-15 mm.

2.5.2 The Forward Muon Detector

It is difficult to link possible muon tracks between the FTD and the central muon system in the forward region due to high track multiplicities. The Forward Muon Detector (FMD) [22] can discriminate between muons coming from the nominal interaction point, beam halo (see next section) and cosmic muons. It consists of three double-layered drift chambers on each side of a toroidal magnet with a magnetic field of 1.5 T. Figure 2.9 depicts a side view of the FMD. All sense wires are strung perpendicular to the beam pipe. The angular coverage of the FMD is $4^\circ < \theta < 17^\circ$. At this low angle the main H1 solenoid has little effect on the muons. The FMD toroid bends the muons in the forward region and hence their momenta can be measured from the angles before and after interacting with the toroidal magnet. Muon momenta in the range $5 < p_T < 200$ GeV can be measured with the FMD. The lower limit is due to the energy absorption of the muons by the toroid and the detector components traversed between the IP and the FMD. Muons with p_T greater than the upper limit are measured with poor resolution since the muons are barely affected by the magnet, resulting in high errors in the momentum measurements.

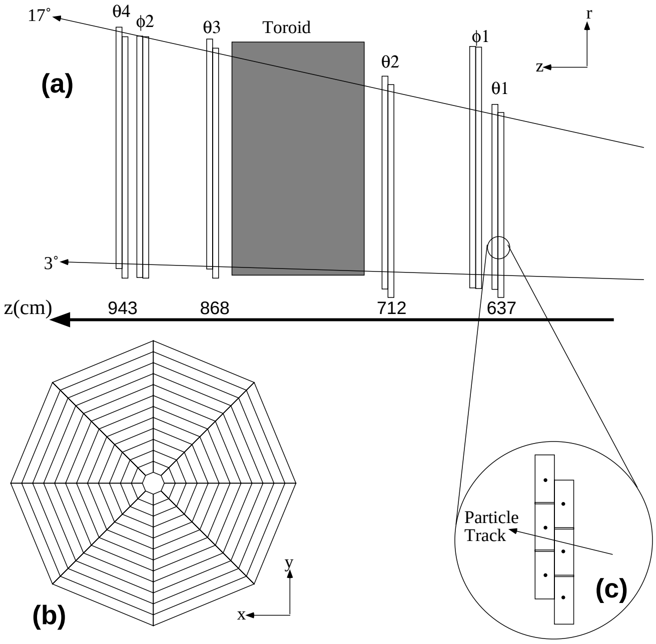

Figure 2.9: (a) A side view of the FMD system with its drift chambers and the toroidal magnet. (b) A theta chamber of the FMD. (c) Particle passage through two different cells.

Momentum measurement in the FMD independent of the FTD reduces the wrong track linking probability in the forward region. The spatial resolution of the FMD is 250 μm.

2.6 The Time of Flight System

The time of flight system [23] is comprised of plastic scintillators placed at various locations around the H1 detector in the backward and forward regions to reject beam induced background events. The rejection of these events is based on their timing information and the fact that the arrival time of particles originating from background interactions is earlier than the arrival time of particles originating from the nominal interaction point to these ToF scintillators. The rate of these background events is studied from the non-colliding pilot bunches.

ToF scintillators are placed as shown in Figure 2.10: within the backward iron endcap (BToF), within the SpaCal (SToF), within the Plug (PTOF) (end of Section 2.4.3) and within the FMD (FToF). Beam induced background includes: beam gas, which is due to the inelastic collision of the proton beam with residual beam gas; beam wall, which is caused by the interaction of the proton with beam pipe wall; and beam halo muons originating from the interaction of the proton beam with the residual gas or hardware outside the H1 detector. The top and bottom of Figure 2.11 show beam gas and beam halo event displays respectively. Beam halo muon events are rejected using two large veto wall scintillators outside the iron. LVeto is located at $z = -6.5$ m and SVeto at $z = -8.1$ m as shown in Figure 2.10.

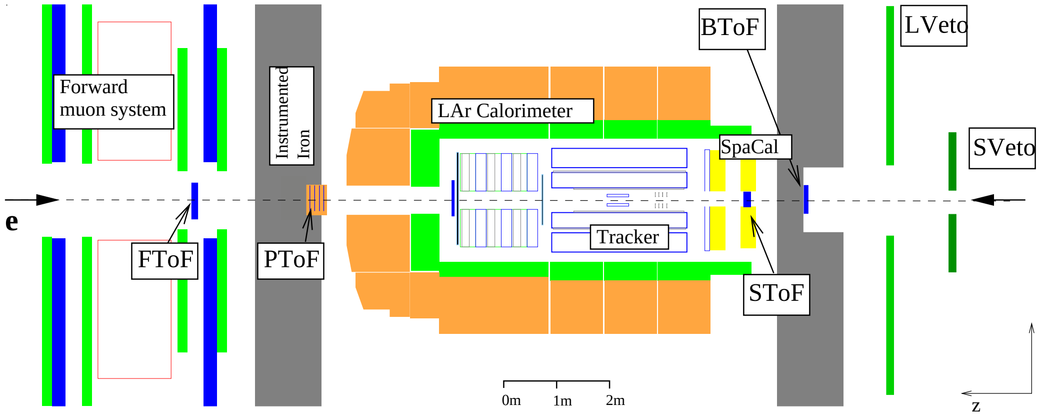

Figure 2.10: The location of the ToF scintillators and Veto Walls.

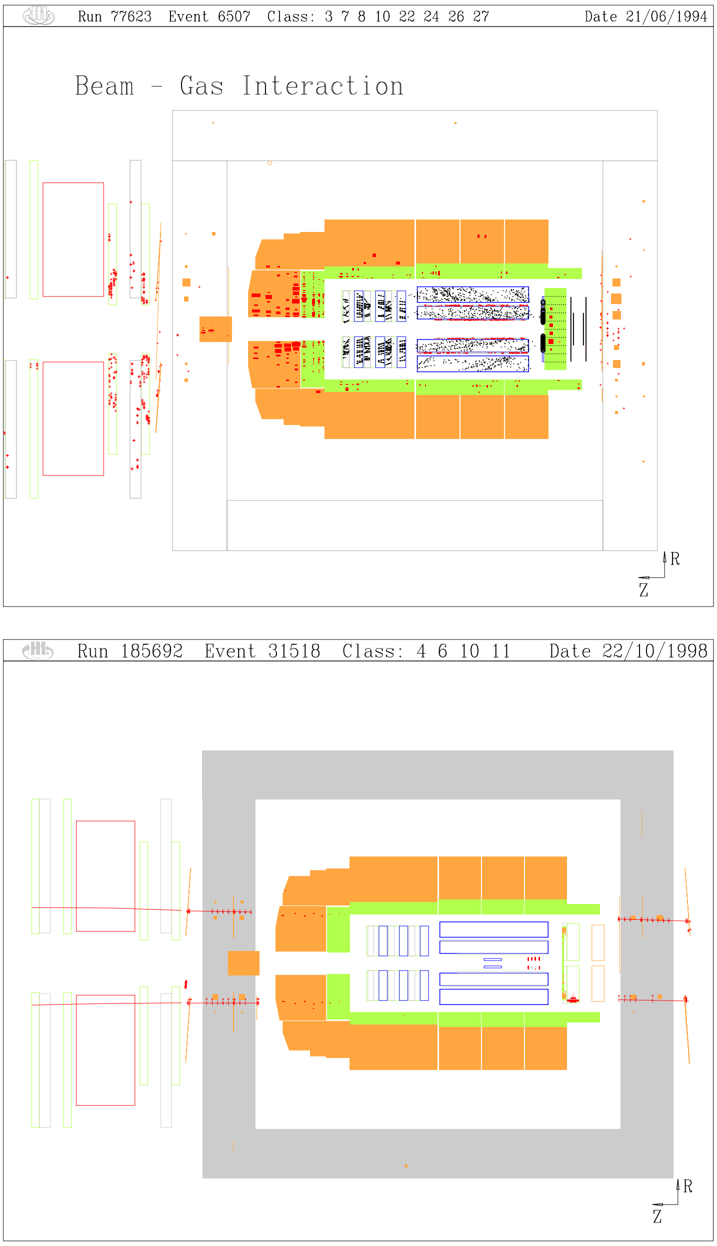

Figure 2.11: Beam gas (top) and beam halo (bottom) event displays.

2.7 The H1 Luminosity System

The luminosity measurement [24] is an essential part of the *ep* collisions in order to calculate cross sections precisely. Two methods are employed in determining the luminosity measurement both of which are based on the precisely known cross section of the Bethe-Heitler process [25]:

$$ep \rightarrow e\gamma p$$

The first method is used online in which both electron and photon must be detected. Since the angular distribution of both these particles is strongly peaked in the electron beam direction, the luminosity system is situated in the backward region. This system is composed of two parts, shown in Figure 2.12 : the electron tagger (ET) located at $z = -33.4$ m and the photon detector (PD) at $z = -102.9$ m. Both detectors are segmented TiCl/TiBr crystal Cerenkov counters with a depth of 22 radiation lengths and a resolution of $\frac{\sigma_E}{E} = \frac{0.10}{\sqrt{E/GeV}} \oplus 0.01$. A set of quadrupoles are used to deflect the scattered electron so that it leaves the system at $z = -27.3$ m through an exit window to be detected by the ET. The main background for the Bethe-Heitler process is the interaction of the incoming electron with the residual beam gas:

$$eA \rightarrow e\gamma A.$$

This can be evaluated from the pilot bunches and is reduced by requiring that the sum of the detected photon and electron energy is not far from the electron beam energy.

The second offline method only demands the number of photons to be detected above a certain threshold energy and is used in physics analysis. In the online method the uncertainty comes from different acceptances of the ET due to different beam conditions. By using the offline method (second method) this problem is not encountered.

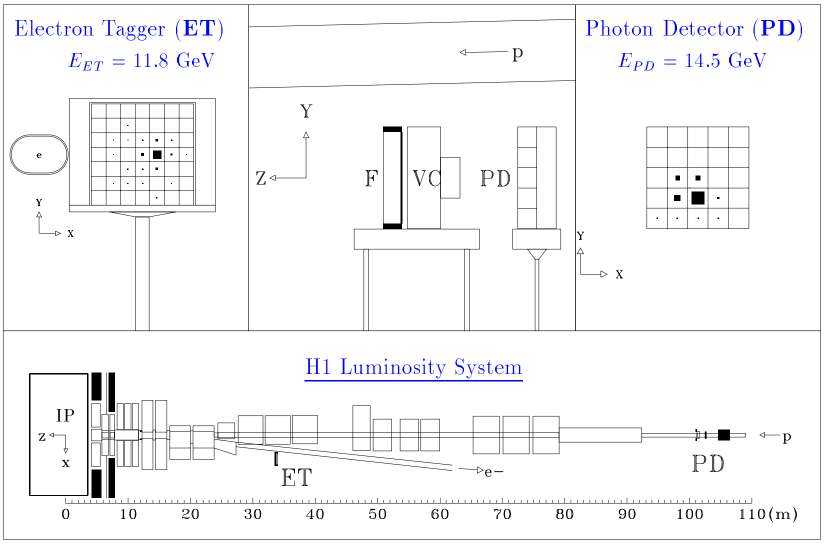

Figure 2.12: The H1 Luminosity system.

2.8 The H1 Trigger System and Data Acquisition

The main purpose of the trigger system is to select *ep* interactions and to reject background, since the background rate is up to a factor of 1000 higher than the *ep* interaction rate.

The rate of *ep* bunch crossings is 10.4 MHz and the maximum rate of event writing to tape is only 10 Hz which makes the reduction of the background events such as beam wall, cosmic or beam halo muons and uninteresting physics events very important. In addition, the rate of detector response to physics events is about 100 Hz which is much lower than the bunch crossing frequency. To combat these difficulties the trigger system was designed as shown in Figure 2.13.
At each bunch crossing all subdetectors send trigger information to the First Level Central Trigger Logic (CTL1) [26] called trigger elements (TEs). The first level consists of 200 TEs which are logically combined into 128 sub-triggers designed to trigger on interesting physics processes and to act as monitor triggers for background

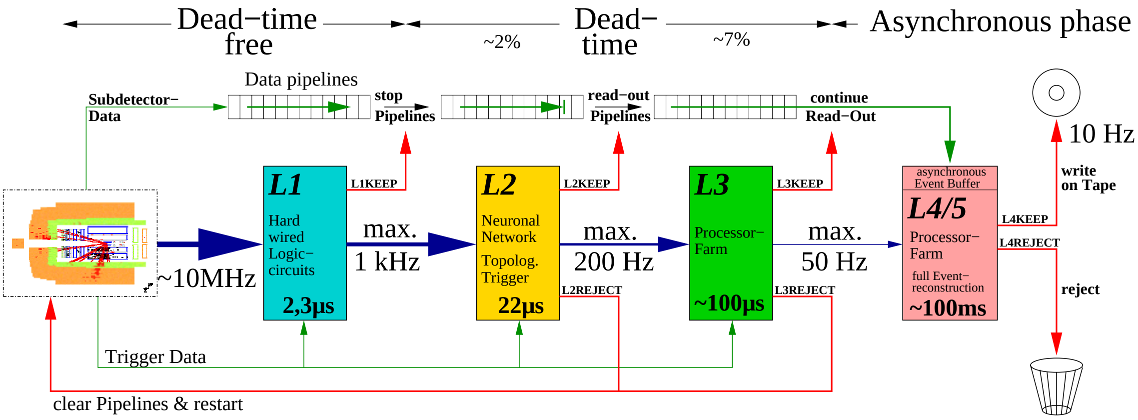

Figure 2.13: A schematic view of the H1 trigger system.

efficency studies. The maximum time allowed for the TE to reach the CTL1 equals 22 bunch crossings (≈ 2.1 μs) and a time of 2 bunch crossings is needed for the CTL1 to take a decision. Because the rate of bunch crossings is higher than that of the trigger decision time, all subtriggers and TEs from subsequent bunch crossing are stored in the so-called *pipeline*. If the decision of a subtrigger is set then a *L1Keep* signal is sent to all subdetectors and, hence, the pipelines of all subdetectors are stopped and *dead time*, during which no more TEs are kept in the pipeline, starts although all information from subsequent bunch crossing is kept in the pipeline otherwise. For common physics processes a technique of *prescaling* is applied in which a fraction of these events are accepted by the CTL1. If the prescale is p then 1 event out of p events is kept. This is to ensure that the trigger system does not only record common processes and ignores the rare events.

The second level (L2) of the trigger system starts once the pipelines are halted. The L2 trigger system consists of two components: the Topological Trigger (L2TT) [27] and the Neural Network trigger (L2NN) [28]. The decision time for this level is 20 μs. This time is used to verify the L1 decision by a combination of signals from different subdetectors. L2TT employs pattern recognition, using a 2D projection of an event in θ and ϕ whilst L2NN uses neural network techniques. Thus, the L1 trigger is revalidated using additional information that was not sent to the CTL1 because of insufficient time. If an event is rejected by L2 the pipelines are cleared and deadtime ends. L2 helps in reducing the prescales of some high rate L1 subtriggers.

Level four (L4)[2] is used to reconstruct events partially . This is achieved by 30 parallel processors providing more detailed reconstruction and selection of tracks and clusters. They require 100 ms to achieve the reconstruction and to store permanently to Production Output Tapes (POTs) containing both the raw and reconstructed event information.

Level five (L5) is employed offline and performs a full event reconstruction and classification into different physics events classes using the H1REC [31] software package. Another storage method is achieved on Data Summary Tapes (DSTs) which is a simplified version of the POT. Typically DSTs are used for physics analysis.

2.9 Detector Monte Carlo Simulation

To understand the detector response to physics events a detailed simulation of the H1 detector is produced using the H1SIM [29] package based on GEANT3 [30]. Details of location, geometrical acceptance and intrinsic resolution of each detector component are implemented.

To compare physics models to the experimental data a Monte Carlo (MC) technique is applied based on random numbers and probability distributions. Physics processes are generated by different software packages. Final states of these processes are produced using all relevant Feynman diagrams and parton distribution functions (next chapter). All particles and final states of jets are described by four-vectors. Up to this level of simulation the information is termed “Generator level”. The measurement of the physics model outcomes predicted from the theory should be

---

[2] Level three (L3) is implemented as part of the HERA II upgrade.

very similar to what we are able to measure using the detector. The H1 detector is simulated using the H1SIM package and then a full reconstruction of the event is implemented using the H1REC software in the same way as the real data. This level is termed the “Reconstructed level”.

Chapter 3

Theoretical Overview

This chapter details the theory behind the work in this thesis. A brief introduction to the Standard Model is followed by an overview of the main physics interactions studied at HERA describing their theoretical basis and the kinematic variables. The motivation of this analysis is introduced and the concept of lepton flavour violation via leptoquark exchange particle is explained. A brief description of the background processes which mimic the lepton violating signal and their Monte Carlo generators concludes this chapter.

3.1 Standard Model

The Standard Model (SM) is a theoretical framework which describes the elementary particles and their strong, weak, and electromagnetic interactions in terms of "gauge theories". A gauge theory is a theory that possesses invariance under a set of transformations whose parameters are space-time dependent (local transformations). The SM only incorporates these three forces leaving the gravitational force because of its weakness compared to the others.

In the SM, the forces between the elementary particles which are called *fermions*,

	1st gen.	2nd gen.	3rd gen.	Q_{em}	colour	weak isospin		spin
						left-hd.	right-hd.	
Quarks	u	c	t	$+\frac{2}{3}$	r,b,g	$\frac{1}{2}$	0	$\frac{1}{2}$
	d	s	b	$-\frac{1}{3}$	r,b,g	$\frac{1}{2}$	0	$\frac{1}{2}$
Leptons	ν_e	ν_μ	ν_τ	0	–	$\frac{1}{2}$	–	$\frac{1}{2}$
	e	μ	τ	-1	–	$\frac{1}{2}$	0	$\frac{1}{2}$

Table 3.1: Fundamental fermions in the SM

are represented by the exchange of gauge vector particles called *bosons*. These gauge bosons are related to the gauge symmetries of the field theories. The SM is invariant under the following group:

$$SU(3)_C \;\times\; SU(2)_L \;\times\; U(1)_Y \tag{3.1}$$

which describes the electromagnetic, weak and strong interactions of the elementary particles. The weak and electromagnetic (*electroweak*) interactions are unified in the gauge group $SU(2)_L \times U(1)_Y$. This symmetry is spontaneously broken: the bosons of the weak interaction are massive with masses 80.43 GeV and 91.19 GeV for the W and Z bosons, respectively. On the other hand, the photon, mediating the electromagnetic interactions, is massless. The strong interaction described in the first term in Eq. 3.1 is a colour gauge symmetry interaction mediated by one of its 8 massless gluons. All these mediating particles are vector gauge bosons possessing spin 1. The fundamental fermions are the quarks and the leptons each possessing spin 1/2 and grouped into *families* or *generations*. Together the groups of fermions and gauge bosons of the SM form the basis for all matter in the universe and are listed in Tables 3.1 and 3.2.

In addition to the gauge symmetry, there exist a number of *internal* symmetries in the SM which hold only approximately. For instance [32],

force	boson	Q_{em}	Mass(GeV)	J^P	related group
strong	8 gluons g	0	0	1^-	$SU(3)_C$
electromag.	γ	0	0	1^-	$SU(2)_L \times U(1)_Y$
weak	$W^\pm$	± 1	80.41	1	$SU(2)_L \times U(1)_Y$
	Z^0	0	91.19	1^-	$SU(2)_L \times U(1)_Y$

Table 3.2: The fundamental gauge bosons in the SM. Q_{em} is the electromagnetic charge, J in J^P is the spin of the particle and P is the parity.

- energy(E), momentum(p), angular momentum(L), charge(Q), colour, baryon number (B) and lepton numbers (L_e, L_μ, L_τ) are conserved physical quantities in all interactions;
- the parity (P) and charge (C) are conserved in the strong and electromagnetic interactions but not in the weak interaction;
- the lepton and quark flavours are conserved in all interactions except the charged current (section 3.2.3) of the weak interaction which transforms one type of quark into another type and one type of lepton into another.

Therefore, conservation laws do not apply to all interactions. So far, within the limits of today's high energy physics experiments, observations are successfully consistent with the SM predictions. The SM has 19 free parameters whose values are to be determined by experiment. Contemporary experiments allows us to probe the SM with an accuracy down to a length scale of 10^{-18} m. However, there are some fundamental questions that the SM does not answer. For example the reason of the existence of three families of lepton and quarks, the matter-antimatter asymmetry and the gravitational force. Hence, there are many suggestions that a theory which describes the matter and interactions in the universe more rigorously is required. Thus, the SM is considered to be an approximation and deviations from the SM may be considered to be a signal for this more general theory.

As mentioned above, the flavour quantum numbers of quarks are not conserved in all interactions. By contrast, lepton flavour was believed to be individually conserved in each generation. This was based on the assumption that the three neutrinos are massless. However, since 1998 [33], there is strong evidence that neutrino flavours oscillate and therefore must have non-vanishing mass. This in turn allows for *lepton flavour violation* (LFV) within neutrinos of different generations. On the other hand, no direct evidence for LFV within the charged massive leptons (e, μ, τ) has so far been observed.

At HERA electrons collide with protons. Since leptons are directly involved at HERA experiments, the deviation from lepton flavour conservation law at high energies can be investigated. Any observation of a LFV process would be a clear indication of physics beyond the SM.

3.2 Deep Inelastic Scattering

At the end of the nineteenth century it was believed that matter consists of atoms which were considered to be the fundamental building blocks of matter, and positive and negative charges were evenly distributed amongst them. In 1911 Rutherford collided α particles with a thin gold foil [34]. He observed a deflection of some positive α particles from their original path and the bounce back of others. From the results of this experiment he concluded that matter consists of atoms whose centres are occupied by a positive constituent. This constituent was called the nucleus and the *scattering* of the α particles off the nuclei was causing their deflection. These nuclei were later found to consist of protons and neutrons. In 1956 Hofstadter studied the scattering of electrons from a hydrogen target and concluded that protons and neutrons have finite size.

The fixed target high energy experiments at SLAC in the late 1960s used an electron beam scattered off nucleons [35]. The observed polar angle distribution of the scattered electrons was dependent only on the square of the four momentum of the mediating boson (which is the photon) and independent of the different values of the *momentum fraction* of the proton which can only be explained by assuming point-like constituents within the proton. These constituents were later called quarks. The early deep inelastic scattering (DIS) experiments helped to establish the quark picture of hadrons.

Today the DIS experiments at HERA allow a deeper insight into the proton and this gives an opportunity to study the dynamical picture of the proton, measure its particle content over a huge kinematical range and to test the predictions of the SM, especially the part which describes the quark and gluon interaction, i.e. Quantum Chromodynamics (QCD). With the available high energies one also can search for potential physics beyond the SM .

3.2.1 Kinematics

In DIS at HERA, an electron e having four momentum k interacts with a proton P with four momentum p via the exchange of a γ or Z in a neutral current (NC) interaction of the form

$$e^{\pm}P \rightarrow e^{\pm'}X,$$

or via the exchange of a $W^{\pm}$ in a charged current (CC) interaction of the form

$$e^{-}P \rightarrow \nu_e X$$
$$e^{+}P \rightarrow \bar{\nu_e} X$$

where X corresponds to the final state system of the hadronic particles. In the case of CC the e^- converts into a neutrino ν_e and the e^+ converts into an antineutrino

$\bar{\nu}_e$. The kinematics of the above processes can be described using combinations of the four vectors.

The set of variables commonly used to describe the kinematics of DIS consists of

$$Q^2 = -q^2 = -(k-k')^2 \tag{3.2}$$

$$x = \frac{Q^2}{2p.q} \tag{3.3}$$

$$y = \frac{p.q}{p.k} \tag{3.4}$$

$$W^2 = (p+q)^2 \tag{3.5}$$

$$s = (k+p)^2 \approx 4E_eE_p \tag{3.6}$$

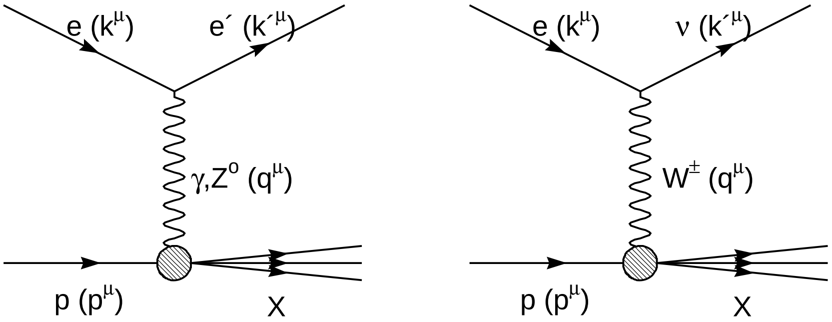

Figure 3.1: Left: NC process. Right: CC process. In the NC process the electron scatters with momentum k' and the exchanged boson is a photon or Z. The exchanged boson in the CC process is W and the scattered particle is a neutrino.

Figure 3.1 shows typical NC and CC processes with the four-momenta of the interacting particles. In the above equations $k = (E_e, \mathbf{k})$ and $p = (E_e, \mathbf{p})$ are the four momenta of the electron and proton respectively. As described in the previous section, the scattering process involves the exchange of a gauge boson which results in a transfer of four-momentum between the incoming and outgoing particles. Q^2 is the negative of the four-momentum transfer squared and $k' = (E'_e, \mathbf{k}')$ is the four-momentum of the scattered lepton. x, called *Bjorken-x*, is the fraction of the proton's four-momentum carried by the struck quark with the assumption that quarks are massless and do not interact with each other [37]. This is the basis of the quark parton model (QPM) where quarks are considered to be point like particles called partons [38]. In this model the nucleon consists of the so-called valence quarks, responsible for the internal quantum numbers of the proton such as charge, as well as of the sea quarks and gluons. The word parton covers both gluon and quark. In this model

$$xq(x) = xq_v(x) + xq_s(x)$$

$$x\bar{q}(x) = x\bar{q}_s(x)$$

$$xq_s(x) = x\bar{q}_s(x)$$

The subscripts v and s denote the valence and sea quarks, q and $\bar{q}$ are the quark and anti-quark densities respectively. In this naive parton model, the quark distributions (or *parton density functions, pdfs*) depend only on x. The partons do not interact with each other and hence the probability functions depend only on the parton momentum.

y is the electron energy fraction transferred to the hadronic system by the exchange boson and it reflects the *inelasticity* of the interaction. The centre of mass energy of the interaction is given in Eq. 3.6 and the centre of mass of the sub-process which considers the whole interaction except the incoming and outgoing leptons (i.e. the boson-proton system) is given in Eq. 3.5.

At fixed s, two Lorentz-invariant variables are sufficient to describe the kinematics. The most common choice is x and Q^2. The relations between the variables is

$$Q^2 = sxy. \tag{3.7}$$

Q^2 gives a measure of the *virtuality* of the exchange gauge vector boson if it is a photon and provides an interaction resolution scale, d, given by the uncertainty principle:

$$Q \times d \approx \hbar. \tag{3.8}$$

Considering the size of the proton which is of the order of 10^{-15} m, $Q^2 \approx 1$ GeV^2. For Q^2 much less than this value, the exchange photon is considered to be almost real and this type of interaction is called *photoproduction* (next section). For high values of Q^2 the exchange photon is not real anymore (and hence virtual) and this allows it to probe the proton and in turn the constituents of the proton can be investigated. This kind of interaction is termed DIS.

3.2.2 Kinematic Reconstruction

In order to determine the cross section, a precise reconstruction of the kinematic variables is needed. As mentioned in the previous section, two kinematic variables are needed to describe the process, e.g. x and Q^2. In the case of a CC process, these kinematic variables can only be reconstructed using the hadronic final state since the neutrino is not detected. The NC events, on the other hand, have more information and therefore various methods can be used to reconstruct the kinematics. The main methods used are introduced in this section.

Electron method

In this method the kinematic variables are determined from the energy E'_e and the polar angle θ_e of the scattered electron:

$$Q_e^2 = 4E_eE'_e\cos^2\frac{\theta_e}{2}, \quad y_e = 1 - \frac{E'_e}{2E_e}(1-\cos\theta_e), \quad x_e = \frac{Q_e^2}{y_e s}, \tag{3.9}$$

where E_e is the energy of the incoming electron and E'_e is the energy of the scattered electron. θ_e is the polar angle of the scattered electron.

Hadron method

In this method the kinematic variables are obtained from:

$$Q_h^2 = \frac{P_{T,h}^2}{1-y_h}, \quad y_h = \frac{\Sigma}{2E_e}, \quad x_h = \frac{Q_h^2}{y_h s}, \tag{3.10}$$

where

$$\Sigma = \sum_i E_i - p_{z,i}, \quad P_{T,h} = \sqrt{(\sum_i p_{x,i})^2 + (\sum_i p_{y,i})^2}, \quad x_h = \frac{Q_h^2}{y_h s}. \tag{3.11}$$

E_i and $p_{z,i}$ are the energy and longitudinal momentum components of particle i, and $p_{x,i}$, $p_{y,i}$ are its momentum components in the transverse plane perpendicular to the z-axis. The summation is over all particles apart from the scattered lepton. This method is only used for the CC measurements. It is not used in the NC measurement due to the degradation of the Q^2-resolution with increasing y. More details can be found in [39].

Double-angle method

This method calculates the kinematic variables using the angle of the scattered lepton, θ_e, and the hadronic final state polar angle, γ_h:

$$y_{DA} = \frac{\sin\theta_e(1-\cos\gamma_h)}{\sin\gamma_h + \sin\theta_e - \sin(\theta_e - \gamma_h)},$$

$$Q^2_{DA} = \frac{4E_e^2 . \sin\gamma_h(1+\cos\theta_e)}{\sin\gamma_h + \sin\theta_e - \sin(\theta_e - \gamma_h)}. \tag{3.12}$$

3.2.3 Cross Section and Structure Functions

The NC double differential cross section as a function of x and y to leading order (LO) in Quantum Electrodynamics (QED) is

$$\frac{d^2\sigma_{NC}^{e^\pm p}}{dxdQ^2} = \frac{e^4}{8\pi x}\left(\frac{1}{Q^2}\right)^2 \left[Y_+\tilde{F}_2^\pm(x,Q^2) - y^2\tilde{F}_L^\pm(x,Q^2) \mp Y_- x\tilde{F}_3^\pm(x,Q^2)\right]. \tag{3.13}$$

The first term includes the electromagnetic coupling constant, where e is the charge of the electron. The bracket contains a linear combination of three different *structure functions*. $\tilde{F}_2$, $\tilde{F}_L$ and $x\tilde{F}_3$. $\tilde{F}_2$ is composed of three further structure functions:

$$\tilde{F}_2^\pm = F_2 - \nu_e \frac{\kappa_w Q^2}{Q^2 + M_Z^2} F_2^{\gamma Z} + (\nu_e^2 + a_e^2)\left(\frac{\kappa_w Q^2}{Q^2 + M_Z^2}\right)^2 F_2^Z \tag{3.14}$$

with

$$\kappa_w^{-1} = 4\frac{M_W^2}{M_Z^2}\left(1 - \frac{M_W^2}{M_Z^2}\right) \tag{3.15}$$

and ν_e and a_e being the vector and axial-vector weak couplings of the electron to the Z boson. F_2, F_2^Z and $F_2^{\gamma Z}$ describe pure γ exchange, pure Z exchange and γZ interference respectively.

The *helicity* dependence term is given by

$$Y_\pm = 1 \pm (1-y)^2 \tag{3.16}$$

$x\tilde{F}_3$ contains pure Z exchange and γZ interference structure functions:

$$x\tilde{F}_3^{\pm} = \pm a_e \frac{\kappa_w Q^2}{Q^2 + M_Z^2} x F_3^{\gamma Z} \mp (2\nu_e a_e) \left(\frac{\kappa_w Q^2}{Q^2 + M_Z^2} \right)^2 x F_3^Z \tag{3.17}$$

$\tilde{F}_L$ is the longitudinal structure function and has zero contribution to the cross section in the QPM which can be considered as the leading order (LO) in cross section.

In the QPM, the structure function F_2 includes sum terms over the quark and anti-quark densities in the proton $q_f(x, Q^2)$ as follows

$$F_2(x, Q^2) = \sum_f e_f^2 x q_f(x) \tag{3.18}$$

where the sum is over all quark and anti-quark flavours, q_f, and e_f is their charge. Whereas F_2 structure functions sum the quark and anti-quark densities, xF_3 structure functions take their differences. As can be seen from equation 3.18 the QPM predicts that these *parton density functions* depend only on x.

The cross section of the CC process is similarly defined as

$$\frac{d^2\sigma_{CC}^{e^\pm p}}{dx dQ^2} = \frac{g^4}{64\pi x} \left(\frac{1}{Q^2 + M_{W^\pm}^2} \right)^2 \left[Y_+ \tilde{W}_2^{\pm}(x, Q^2) - y^2 \tilde{W}_L^{\pm}(x, Q^2) \mp Y_x \tilde{W}_3^{\pm}(x, Q^2) \right] \tag{3.19}$$

where g is the electroweak coupling constant given by

$$g^2 = \frac{e^2}{\sin^2 \theta_W} \approx 4e^2, \tag{3.20}$$

and $\tilde{W}_2$, $\tilde{W}_L$ and $x\tilde{W}_3$ are the equivalent CC structure functions. Because the CC propagator term includes the mass of the W boson, $M_{W^\pm}$, its cross section is suppressed at low Q^2 with respect to the NC process.

At the electroweak unification scale, where $Q^2 \geq M_{W^\pm}^2 \approx M_Z^2 \approx 10^4$ GeV^2, the NC and CC cross sections are of the same order as can be seen from the measured cross section shown in Figure 3.2 [41]. In the high Q^2 domain, Z exchange also contributes significantly to the NC process causing constructive γZ interference in e^-p interactions and destructive interference in e^+p interactions. In CC the e^-p cross section is larger compared to the e^+p process at higher Q^2. This is due to the charged W^- boson coupling to the u valence quark in the proton while the W^+ boson couples to the d valence quark in the proton.

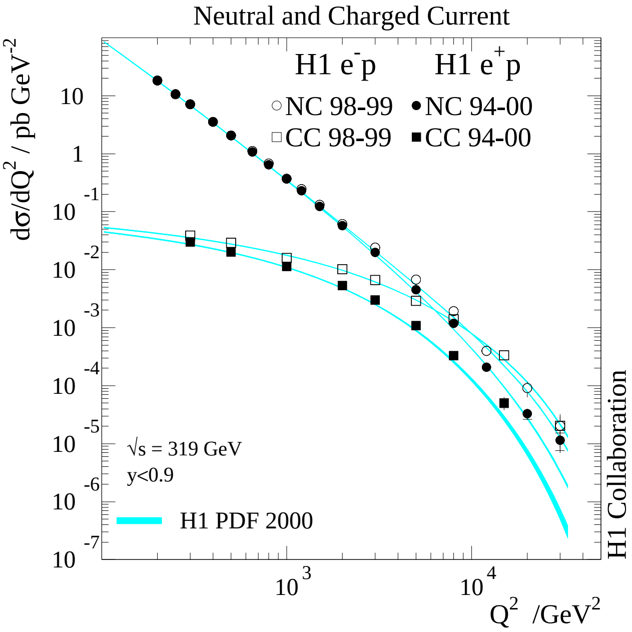

Figure 3.2: The differential cross section of the NC and CC processes for e^-p and e^+p interactions. Both processes have higher cross sections in the e^-p interactions at high Q^2 than the e^+p interactions.

3.2.4 Scaling Violation and Quantum Chromodynamics

Scaling Violation

Early measurements of DIS indicated that the F_2 structure function was only dependent on Bjorken-x and independent of Q^2. Therefore, because the F_2 measurement

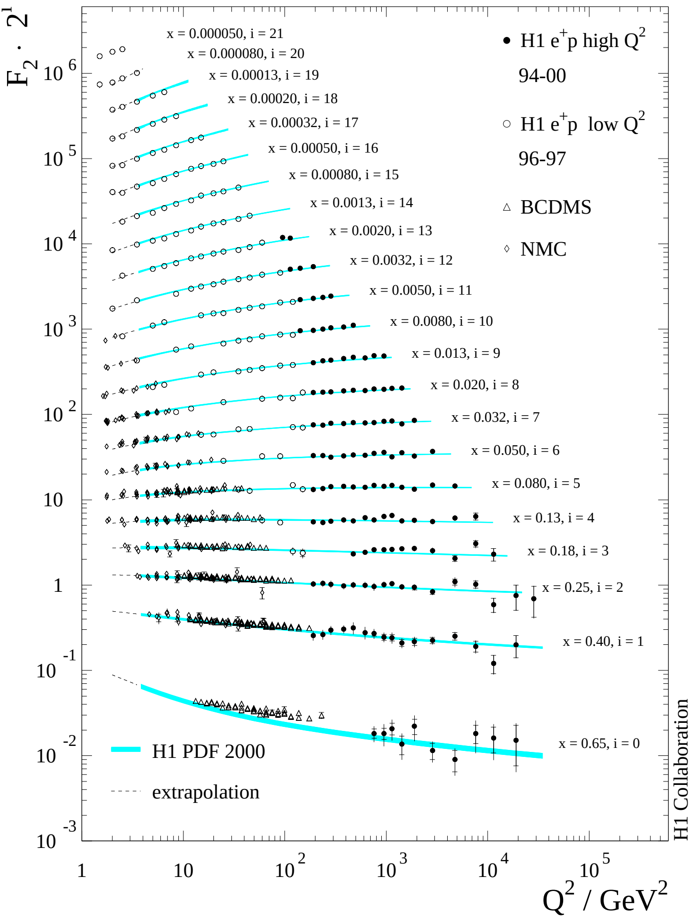

Figure 3.3: The $F_2(x, Q^2)$ structure function distribution as a function of Q^2 with different values of x for different experiments.

was independent of any length scale probing the proton (Eq. 3.8) this phenomenon was called *scaling invariance* [37, 44].

However, when measurements were performed on a larger range of x and Q^2 this behaviour of the structure function no longer held, and *scaling violations* were established [42, 43]. The $F_2(x, Q^2)$ structure function may be extracted from the NC differential cross section measurement. Figure 3.3 [41] shows the $F_2(x, Q^2)$ distribution with respect to Q^2 for different values of x measured at H1 and compared to other experiments. At low x, F_2 is seen to rise with Q^2 and to fall with Q^2 at high x. This rise of F_2 at low x can be explained by considering the effect of the gluons in the proton. The density of the gluons, and hence the sea quarks, in the proton $xg(x)$ is seen to rise with falling x as shown in Figure 3.4 [45]. That is, the number of gluons in the proton carrying a fraction x of the proton's momentum increases as x decreases. The rise of F_2 at low x with increasing Q^2 is then attributed to the increase in the resolving power of the photon probe to detect the partonic content of the proton since more partons are probed and hence added to the structure function. The fall of F_2 with rising x is attributed to the decrease in number of partons with high x. This asserts that the *pdfs* depend on Q^2. Figure 3.5 shows the pdfs for different quarks inside a proton with $Q^2 = 10^4$ GeV^2.

Based on the assumptions of the QPM, the sum of all parton momenta must be equal to the sum of the momentum of the proton, i.e.

$$\sum_f \int_0^1 dx\ x\ q_f(x) = 1. \tag{3.21}$$

Therefore, from the momentum sum rule and considering all quarks it was found that only approximately 50% of the proton's momentum is carried by quarks. This deficit is attributed to the gluons.

Quantum Chromodynamics

Scaling violations are described by introducing corrections to the QPM using Quantum Chromodynamics (QCD), the theory which describes the interactions between quarks and gluons. QCD is, unlike QED, a non-Abelian theory. This fact is reflected by gluons being able to couple to each other, whereas photons cannot couple to each other. The QPM is equivalent to the zeroth order of QCD; higher order corrections are introduced as a perturbative expansion in orders of the strong coupling constant, α_s, which, by the introduction of gluons, depends on Q^2 and at leading order equals:

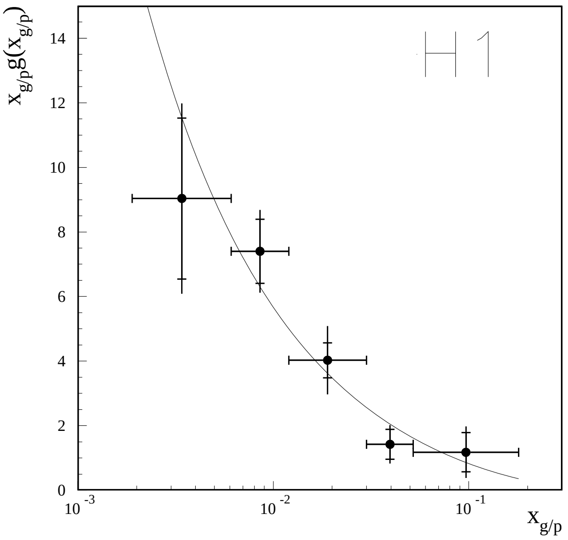

Figure 3.4: The gluon density distribution with respect to x.

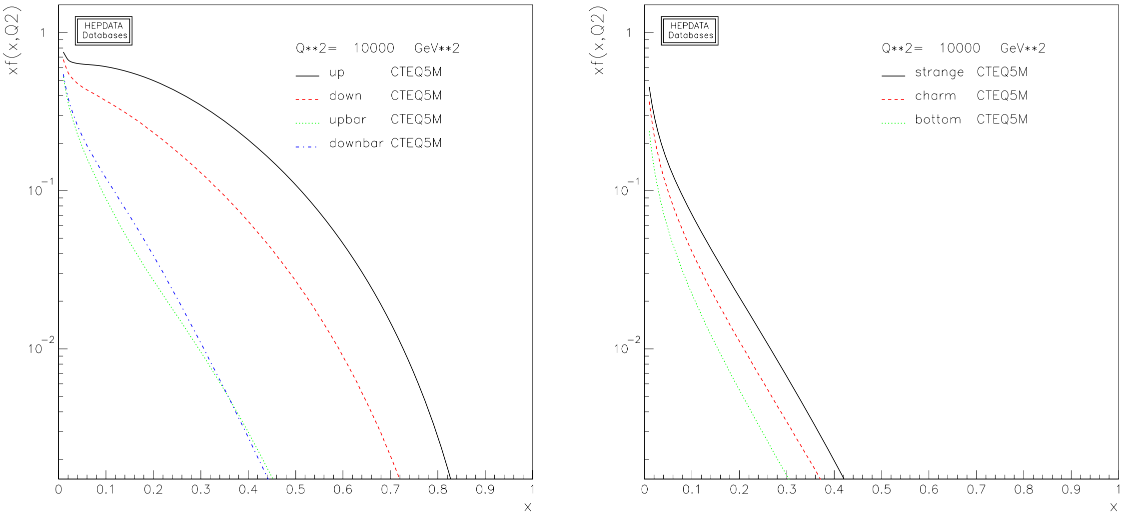

Figure 3.5: Plots of the pdfs of the proton using CTEQ5 for different quark contributions. As x increases the pdfs decrease steeply.

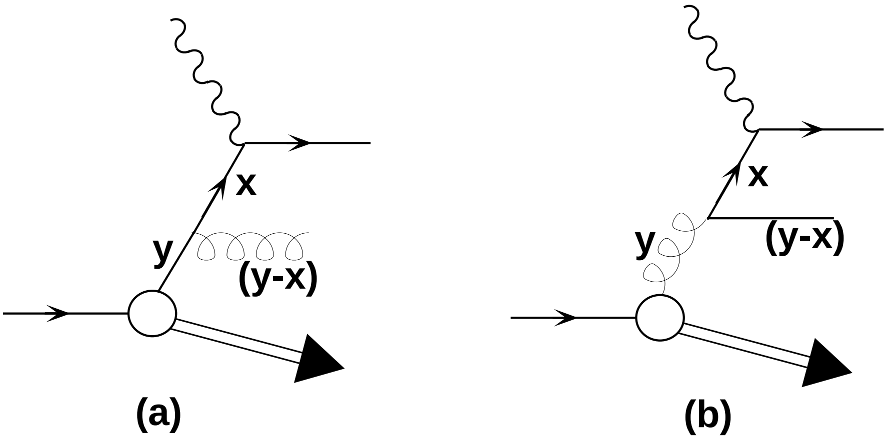

Figure 3.6: (a) Quark splitting into gluon and quark. (b) Gluon splitting into two quarks.

$$\alpha_s = \frac{12\pi}{(33-2N_f).(\ln Q^2/\Lambda^2_{QCD})} \tag{3.22}$$

where N_f is the number of quark flavours and Λ_{QCD} is a scale parameter which has to be determined by experiment. From this equation for high values of Q^2, α_s is much smaller than unity. In this case quarks are considered to be free and non-interacting – a property known as *asymptotic freedom*. When Q^2 decreases α_s becomes large and the strong coupling constant gets larger – a situation known as *quark confinement*. In this case the perturbative expansion converges and perturbative expansion can be used.

LO corrections are formulated using the Dokshitzer-Gribov-Alterelli-Parisi (DGLAP) splitting functions [46]:

$$\frac{dq(x,Q^2)}{d\ln Q^2} = \frac{\alpha_s(Q^2)}{2\pi}\int_x^1 \frac{dy}{y}\left[q(y,Q^2)P_{qq}\left(\frac{x}{y}\right) + g(y,Q^2)P_{qg}\left(\frac{x}{y}\right)\right] \tag{3.23}$$

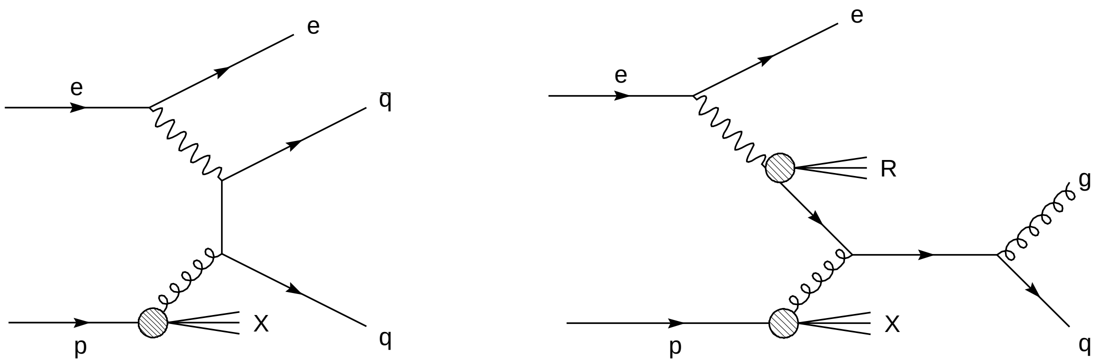

Figure 3.7: Left: Direct photoproduction process. Right: Resolved photoproduction process.

$$\frac{dg(x,Q^2)}{d\ln Q^2} = \frac{\alpha_s(Q^2)}{2\pi}\int_x^1 \frac{dy}{y}\left[q(y,Q^2)P_{gq}\left(\frac{x}{y}\right) + g(y,Q^2)P_{gg}\left(\frac{x}{y}\right)\right] \tag{3.24}$$

resulting in logarithmic terms in $\ln Q^2$ and $\alpha_s \ln \frac{1}{x}$. These functions express the probability that a parton will “split”, either into a quark radiating a gluon or a gluon converting to a $\bar{q}q$ as illustrated in Figure 3.6, i.e. the splitting functions P_{ij} indicates the probabilities for the splitting process, in Figure 3.6, of finding a parton i from a parton j with the momentum fraction $z = \frac{x}{y}$ of the parent quark momentum in the range $\ln Q^2, \ln Q^2 + d\ln Q^2$. Feynman diagrams such as those in Figure 3.6 are included in the splitting functions. This approach is valid for large values of x. For the use of DGLAP at low x more details are given in [47].

3.3 Photoproduction

In this region the exchanged photon is said to be *quasi-real* since $Q^2 \approx 0$. A process is termed photoproduction if the electron is detected in either in the 33m or 44m electron taggers (ET).

The cross section is mainly dependent on the *propagator term*, $\frac{1}{Q^4}$, and since $Q^2 \approx 0$ it can be inferred that the total ep cross section is dominated by photoproduction. Photoproduction processes are divided into three types.

1. Low transverse momentum processes which involve vector meson production such as ρ, ω or ϕ where the contribution for this meson production is obtained from the photon and partially from the proton.

2. *Direct* high transverse momentum with the photon directly coupling point-like to the hard subprocess via partons from the proton as shown in Figure 3.7 and contributing totally to the hard sub-process.

3. *Resolved* high transverse momentum in which the photon fluctuates into a $q\bar{q}$ pair, one of which couples to the hard sub-process. Unlike the *Direct* case, some of the photon momentum contributes to the hard sub-process and the rest can be detected as the photon remnant, R [50].

3.4 Lepton Flavour Violation in the SM

The experimental observation that all known interactions involving charged leptons conserve the lepton flavour individually was one of the bases for the classification of the known leptons into three families. However, since this fact has not yet been related to an underlying gauge symmetry, it is not clear whether lepton flavour is one of the fundamental quantum numbers.

Many searches for specific LFV processes in low energy experiments have been performed. Some of these searches are for the transition $e \leftrightarrow \mu$, which includes the searches for $\mu + N \rightarrow e + N$, $\mu \rightarrow e\gamma$ and forbidden leptonic kaon decays, e.g. $K \rightarrow e\mu$. LFV searches involving τ leptons have also been performed such as searches for forbidden decays of B-mesons:, e.g. $B \rightarrow \bar{e}\tau X$. Limits for these processes have been set by the low energy experiments.

The mass of the neutrino plays an important role in LFV. The neutrino mixing matrix U_{MNS} [52] is a unity matrix (when neutrinos are considered massless) resulting in a negative sign for LFV, i.e. forbidden, in the neutrino sector of the SM. However, if neutrino masses are taken into account, the mixing matrix element will take a value different from unity which allows for neutrino mixing and hence LFV in this sector.

The Super-Kamiokande (SK) [33] Collaboration has reported experimental evidence for the oscillation of atmospheric neutrinos and the SNO experiment studies the solar neutrino cross section. These neutrinos are mainly muon and electron neutrinos resulting from cosmic protons which interact with atmospheric atoms. This mainly produces pions which decay in the following way:

$$\pi^+ \rightarrow \mu^+\nu_\mu \rightarrow e^+\nu_\mu\bar{\nu_\mu}\nu_e$$

$$\pi^- \rightarrow \mu^-\bar{\nu_\mu} \rightarrow e^-\bar{\nu_\mu}\nu_\mu\bar{\nu_e}.$$

As we can see from these decays, the ratio of ν_μ to ν_e is 2. However, the measured value is much less than expected. This can be explained by the disappearance of the ν_μ due to oscillations into other neutrino types. The SK detector detects these neutrinos and distinguishes between them. The mechanism relies on the fact that each of these neutrinos hits a target. The scattering of a neutrino with the target produces a massive lepton of the same neutrino family, i.e muon or electron, which can then be further detected.

If neutrinos are massive, processes of the type $\mu \rightarrow e\gamma$ (Figure 3.8) and $\mu \rightarrow 3e$ may occur [53]. The branching ratio for the process $\mu \rightarrow e\gamma$ (a neutrino mass of $m_i = 10$ eV) is very small: $BR(\mu \rightarrow e\gamma) \sim 10^{-50}$ [53] obtained from

$$BR(\mu \rightarrow e\gamma) = \frac{3\alpha}{32\pi}\left(\sum_i V_{ei}^* V_{\mu i}\frac{m_i^2}{m_W^2}\right)^2 \tag{3.25}$$

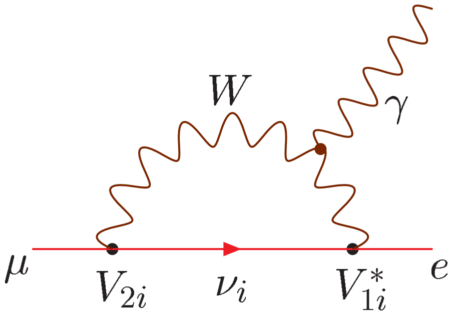

Figure 3.8: Feynman diagram for $\mu \to e\gamma$.

The experimental limits on such LFV reactions are $BR(\mu \to e\gamma) < 1.2 \times 10^{-11}$ and $BR(\mu \to e^- e^+ e^-) < 1.0 \times 10^{-12}$ at 90% confidence level (CL) [54]. Hence, because of the very small neutrino mass the effect of LFV in the SM is too small to be detected by present experiments. Upper bounds on neutrino mass obtained from cosmological measurements for ν_e are $\mathcal{O}(1 \text{ eV})$. The results of the SK and SNO experiments are compatible with the assumption of $m_i \leq 10$ eV. From these neutrino measurement observations and from Eq. 3.25 we deduce that LFV does not exist in the current SM. Therefore any evidence for LFV from experiments would indicate physics BSM.

3.5 Lepton Flavour Violation in BSM Theories

In this section an overview of some models containing LFV is discussed. The potential scenario relevant to HERA physics is discussed in more detail.

3.5.1 LFV in Gauge and Extra Dimension Theories

Many grand unified theories (GUTs) are based on the $SU(5)$ group. In such theories, quarks and leptons can transform into each other by means of very heavy gauge bosons (X, Y). In this model only the combination of quantum numbers $(B - L)$ is conserved [34, 54]. LFV can occur due to the irrelevant lepton type in this transformation.

Lepton flavour is considered to be one of the global symmetries which are, in general, believed to be violated by quantum gravity. When extra spatial dimensions are compactified at larger scales than the electroweak one, the quantum gravity scale may be low and $\mathcal{O}$ (1 TeV) [55,56]. These extra-dimensions may modify the gravitational force law at distances small compared to the size of the extra dimensions. LFV can occur at an observable level if the underlying 4-fermion operators are generated via low scale quantum gravity effects, with large extra dimensions [57]. Therefore, LFV with extra dimensions is commonly discussed. LFV is also discussed in some extra dimension theories concerning neutrino oscillation and fermion mass hierarchy.

3.5.2 Leptoquarks

A possible signature for LFV at HERA would be reactions of the type:

$$e + p \to l + X \tag{3.26}$$

where l stands for a higher generation charged lepton (μ or τ) and X is the hadronic final state.

LFV could be mediated by the exchange of hypothetical particles as shown in Figure 3.9 with Yukawa couplings to both leptons and quarks. These particles are called leptoquarks (LQs) and they do not exist in the SM. They have the following properties:

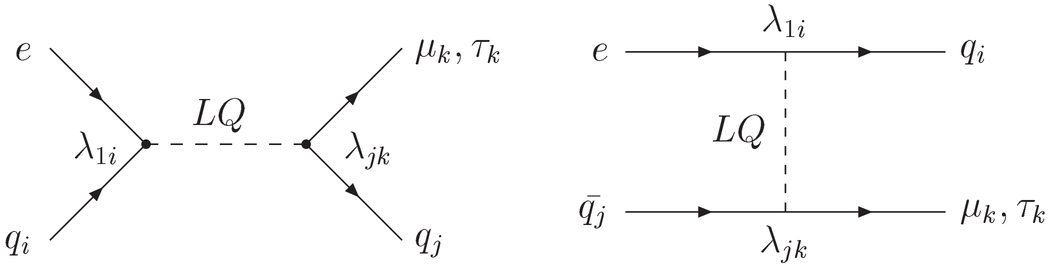

Figure 3.9: Left: s-channel LFV process. Right: u-channel LFV process. Positron (electron) interacts with a valence quark in the s-channel and with a sea antiquark in the u-channel. The LQ in both channels is of $F = 0$ ($F = 2$) type. A sea quark can be involved in the s-channel and a valence quark in the u-channel.

1. LQs are either spin 0 (scalar) or spin 1 (vector) bosons.
2. They carry colour charge.
3. They have fractional electrical charges.
4. They carry non-zero lepton and baryon numbers.

LQs are part of many models beyond the SM, such as GUTs, compositeness models or technicolour theories. Their existence would give an explanation for the clear symmetry between the lepton and quark families. These particles can provide a good mechanism for LFV because they can couple to different lepton and quark flavours.

It is convenient to use the effective phenomenological Lagrangian of Buchmüller, Rückl and Wyler (BRW) [58] which describes LQ production under the $SU(3)_C \times SU(2)_L \times U(1)_Y$ symmetry. In this model there are fourteen LQs (see Table 3.3), seven scalar and seven vector. The fermion number for LQs is defined as:

$$F = L + 3B \tag{3.27}$$

where L and B are the lepton and baryon numbers of the involved lepton and quark respectively. LQs with $F = 2$ are resonantly produced in e^-p scattering, whereas $F = 0$ LQs are resonantly produced in e^+p scattering. With these fermion numbers and the corresponding scattering lepton the LQs are formed from valence quarks which have high Bjorken-x and can be produced resonantly as shown in Figure 3.9 (s-channel).

The following assumptions are adopted in the analysis [59]:

1. The LQ couplings are invariant under $SU(3)_C \times SU(2)_L \times U(1)_Y$ (BRW model).
2. The LQ has either left- or right-handed couplings, but not both.
3. The members of each weak-isospin doublet are degenerate in mass.
4. The production process is dominated by one LQ species.

In the BWR model LQs can be resonantly produced in the s-channel with the following double differential cross section at Born level:

$$\frac{d\sigma^2}{dxdy} = \frac{1}{32\pi xs} q_i(x,\hat{s}) \frac{\lambda^2_{eq_i}\ \lambda^2_{lq_j}\ s^2\ x^2}{(sx - M^2_{LQ})^2 + M^2_{LQ}\Gamma^2_{LQ}} \times f_s(y) \tag{3.28}$$

where $f_s(y) = \frac{1}{2}$ and $f_s(y) = 2(1-y)^2$ are valid for scalar and vector LQs, respectively, $q_i(x,\hat{s})$ is the parton density of the incoming quark, and $\lambda^2_{eq_i}$ and $\lambda^2_{lq_j}$ are the coupling at the electron-quark and lepton-quark vertices, respectively. The variable M_{LQ} is the mass of the LQ, s is the centre of mass energy and x is Bjorken-x. Γ_{LQ} is the partial width and is given by:

$$\Gamma_{LQ} = M_{LQ}\lambda^2_{lq_i} \times g \tag{3.29}$$

LQ type	Aachen	BRW	Q	T_3	Y	F	Prod.	Decay	Coupl.	BR
1	S_0^L	S_{1L}	+1/3	0	+2/3	2	$e_L\bar{u}$	$l\bar{u}$	λ_L	1/2
								$\nu\bar{d}$	-λ_L	1/2
2	S_0^R	S_{1R}	+1/3	0	+2/3	2	$e_R\bar{u}$	$l\bar{u}$	-λ_R	1
3	$\tilde{S}_0^R$	$\tilde{S}_{1R}$	+4/3	0	+8/3	2	$e_R\bar{d}$	$l\bar{d}$	λ_R	1
4	S_1^L	S_{3L}	+1/3	0	+2/3	2	$e_L\bar{u}$	$l\bar{u}$	-λ_L	1/2
				0				$\nu\bar{d}$	-λ_L	1/2
			-2/3	-1			–	$\nu\bar{u}$	$\sqrt{2}\lambda_L$	0
			+4/3	+1			$e_L\bar{d}$	$l\bar{d}$	-$\sqrt{2}\lambda_L$	1
5	$V_{1/2}^L$	V_{2L}	+4/3	+1/2	+5/3	2	$e_L\bar{d}$	$l\bar{d}$	λ_L	1
			+1/3				–	$l\bar{u}$	λ_L	0
				-1/2			–	$\nu\bar{d}$	λ_L	0
6	$V_{1/2}^R$	V_{2R}	+4/3	+1/2	+5/3	2	$e_R\bar{d}$	$l\bar{d}$	λ_R	1
			+1/3	-1/2			$e_R\bar{u}$	$l\bar{u}$	λ_R	1
7	$\tilde{V}_{1/2}^L$	$\tilde{V}_{2L}$	+1/3	+1/2	-1/3	2	$e_L\bar{u}$	$l\bar{u}$	λ_L	1
			-2/3	-1/2			–	$\nu\bar{u}$	λ_L	0
8	V_0^L	U_{1L}	+2/3	0	+4/3	0	e_Ld	ld	λ_L	1/2
								νu	λ_L	1/2
9	V_0^R	U_{1R}	+2/3	0	+4/3	0	e_Rd	ld	λ_R	1
10	$\tilde{V}_0^R$	$\tilde{U}_{1R}$	+5/3	0	+10/3	0	e_Ru	lu	λ_R	1
11	V_1^L	U_{3L}	+5/3	+1	+4/3	0	e_Lu	lu	$\sqrt{2}\lambda_L$	1
			+2/3	0			e_Ld	ld	-λ_L	1/2
				0				νu	λ_L	1/2
			-1/3	-1			–	νd	$\sqrt{2}\lambda_L$	0
12	$S_{1/2}^L$	R_{2L}	+5/3	+1/2	+7/3	0	e_Lu	lu	λ_L	1
			+2/3	-1/2				νu	λ_L	0
13	$S_{1/2}^R$	R_{2R}	+5/3	+1/2	+7/3	0	e_Ru	lu	λ_R	1
			+2/3	-1/2			e_Rd	ld	-λ_L	1
14	$\tilde{S}_{1/2}^L$	$\tilde{R}_{2L}$	+2/3	+1/2	+1/3	0	e_Ld	ld	λ_L	1
			-1/3	-1/2			–	νu	λ_L	0

Table 3.3: The 14 LQ types in the BRW model. The second and third column show the Aachen and the original BRW nomenclature for LQ classification, respectively. The other columns show the electrical charge for the LQs, the third component of the weak isospin, the hypercharge (where $Y = 2\times(Q-T_3)$), the fermion number, the production and decay channels, the relative coupling strengths and the branching ratios into $l^{\pm}q$ respectively. The subscript in the Aachen nomenclature indicates the isospin of the LQ and the superscript refers to the incoming lepton helicity. S is used for scalar (spin 0) LQs and V (spin 1) for vector LQs. The information here are given for e^+p collisions. The production channels are s-channel.

where $g = \frac{1}{16\pi}$ and $g = \frac{1}{24\pi}$ for scalar and vector LQs respectively. LQs can be produced as an exchanged particle in the u-channel with the following double differential cross section:

$$\frac{d\sigma^2}{dxdy} = \frac{1}{32\pi xs} q_i(x, -u) \frac{\lambda^2_{eq_i}\ \lambda^2_{lq_j}\ s^2\ x^2}{\left[sx(1-y) + M^2_{LQ}\right]^2} \times f_u(y) \tag{3.30}$$

with $f_u(y) = \frac{1}{2}(1-y)^2$ and $f_u(y) = 2$ for scalar and vector LQs.

LQ cross sections at masses less than the kinematic limit can be obtained from the Narrow Width Approximation (NWA) [58]. At these masses, and depending on the coupling constant, the s-channel is more dominant than the u-channel. Hence the cross section can be obtained for the s-channel from:

$$\sigma \ = \ \frac{\pi}{4s}\lambda^2_{eq_1} BR(LQ \to lq_j) q_1(x_0, M^2_{LQ}) \int_0^1 f_{NWA}(y) dy$$

$$= (J+1)\frac{\pi}{4s}\lambda^2_{eq_1} BR(LQ \to lq_j) q_1(x_0, M^2_{LQ}) \tag{3.31}$$

with $f_{NWA} = 1$ for scalar LQs and $f_{NWA} = 6(1-y)^2$ for vector LQs; J is the spin of the LQ and $BR(LQ \to lq_i)$ denotes the branching ratio of the LQ into lq_j.

In $M_{LQ} \gg \sqrt{s}$, both u- and s-channel diagrams contribute considerably to the cross section (Figure 3.9) and the LQ propagator contracts to a four-fermion interaction. The *High Mass Approximation* (HMA) can simplify the cross section calculation in this region [91]:

$$\sigma^{HMA} = \frac{s}{32\pi}\left[\frac{\lambda_{eq_i}\lambda_{lq_i}}{M^2_{LQ}}\right]^2 \times$$

$$\left(\int dx\ dy\ xq_i(x, \hat{s}) f(y) + \int dx\ dy\ x\bar{q}_j(x, -u)\ g(y)\right) \tag{3.32}$$

where

$$f(y) = \begin{cases} 1/2 & \text{scalar LQ} \\ 2(1-y)^2 & \text{vector LQ} \end{cases}$$

$$g(y) = \begin{cases} 1/2(1-y)^2 & \text{scalar LQ} \\ 2 & \text{vector LQ} \end{cases}$$

q_i and q_j label the densities of the quarks that couple to the electron and the higher generation leptons, respectively. The first term in the equation is for the s-channel contribution and the second term is for the u-channel. This approximation of the cross section is accurate to better than 10% for $M_{LQ} > 500$ GeV [59]. In this region both $F = 0$ and $F = 2$ high mass LQs are considered in both e^-p and e^+p interactions.

3.6 LFV Signal Processes

For the simulation of the LFV signal the `LEGO` [60] event generator is used. `LEGO` takes into account initial QED radiation in the collinear approximation. The initial and final state parton showers are simulated according to DGLAP evolution equations and the kinematics at the decay vertex are properly corrected for the effect of the parton shower masses. `LEGO` incorporates s- and u-channel LQ exchange processes. The LQ signal cross sections are calculated using the full matrix elements from the theory. For the parton densities, the CTEQ5 [61] parametrisations of parton densities are used to evaluate the cross sections. The Feynman diagram for the LQ decaying to a muon and a quark is shown in Figure 3.9. Figure 3.10 shows a hypothetical event display for this process. The back-to-back feature of the signal is shown clearly in the radial view.

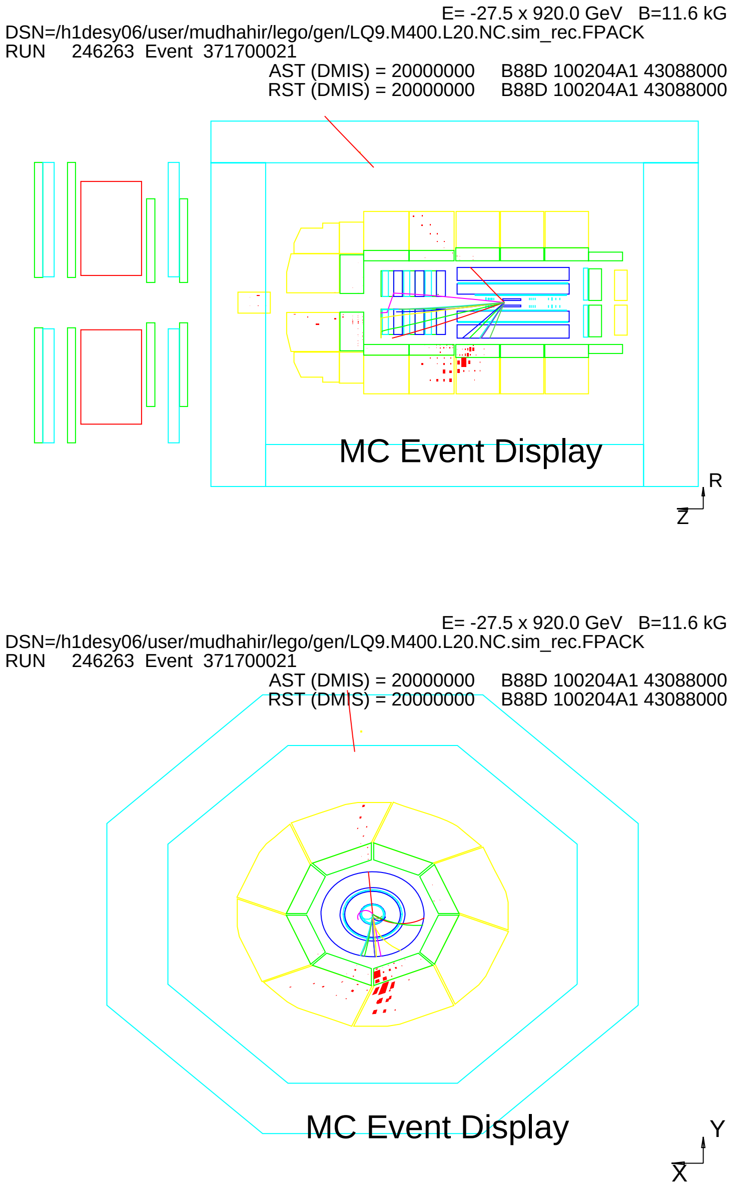

Figure 3.10: $LQ \rightarrow \mu + q$ MC event display in transverse (top) and radial (bottom) views.

3.7 Background Processes

Many background processes may mimic the topology of the signal. These processes include events from lepton pair production, photoproduction, NC and CC processes and W production. Reduction of this background is vital in order to obtain a clean sample of the process we seek to find, or to reduce the limits on this process in case a significant number of signal events is not found. The Monte Carlos used for the simulation of each background process are also introduced here.

3.7.1 Lepton Pair Production

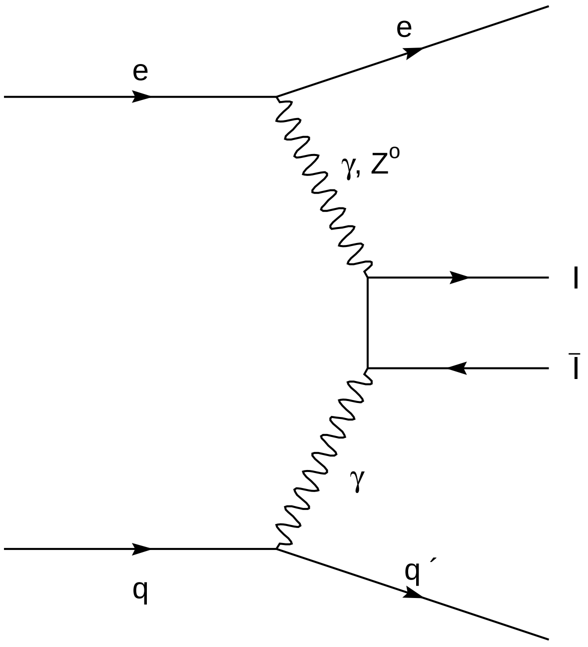

Figure 3.11: Lepton pair process.

Lepton pair production via photon-photon interaction is illustrated in Figure 3.11.

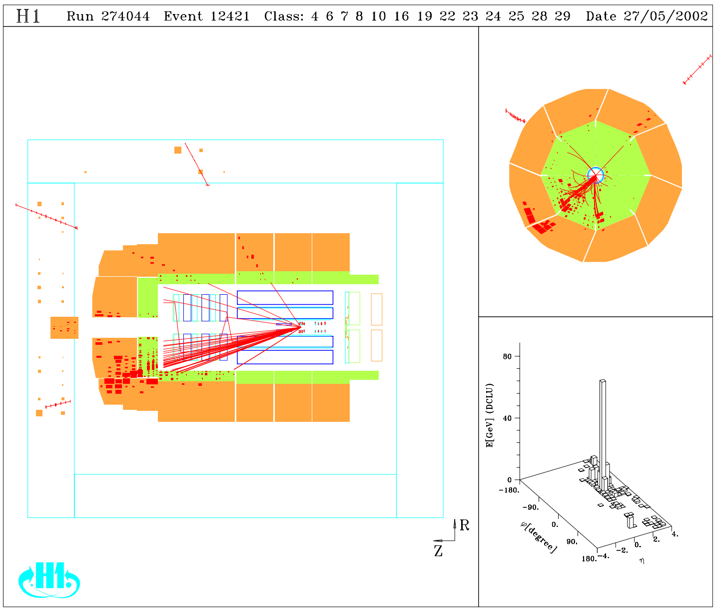

Figure 3.12: Lepton pair event display. The two muons in this event have escaped the LAr through the central and forward muon systems. A muon is also visible in the hadronic final state.

A typical event display is shown in Figure 3.12, where a $\mu^+\mu^-$ pair is produced and is detected with the hadronic jet from the interacting quark. This process can contribute to the background if one lepton escapes detection. If one muon is undetected and is back-to-back with the jet then the event topology is similar to the signal process. More details on lepton pair production at HERA may be found in [62].

The event generator `GRAPE` [64] includes all Feynman diagrams, NLO corrections and initial and final state radiation. It is used to calculate the predicted rate from the lepton pair process. The dominant contribution, lepton pair production via photon-photon processes, is found to be compatible with the prediction given by a second generator, `LPAIR` [65]. Di-lepton J/ψ events are also included in this contribution, calculated using the event generator `EPJPSI` [66].

3.7.2 Photoproduction

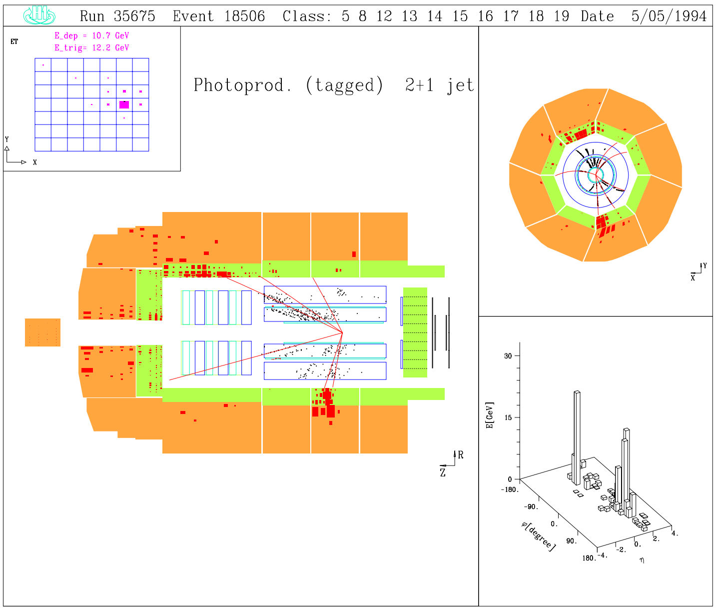

Figure 3.13: Photoproduction event display. The scattered electron is tagged in the ET and particles from the two jets are absorbed in the hadronic and electromagnetic LAr.

Feynman diagrams of photoproduction are shown in Figure 3.7 and a typical event display is shown in Figure 3.13 with two hadronic jets and a tagged electron. These events can mimic the signal if one of the two hadronic jets consists of a single isolated hadron which may decay to a muon or pass through the detector without significant hadronic interaction and subsequently be misidentified as a lepton. The event generator `PYTHIA` [67] is used to calculate the SM predicted photoproduction rate. Since leptonic decays of heavy quark pairs, e.g beauty ($b\bar{b}$) and charm ($c\bar{c}$), are possible a further event generator, `AROMA` [68], is also included. This MC generator simulates the production of heavy quarks in boson gluon fusion.

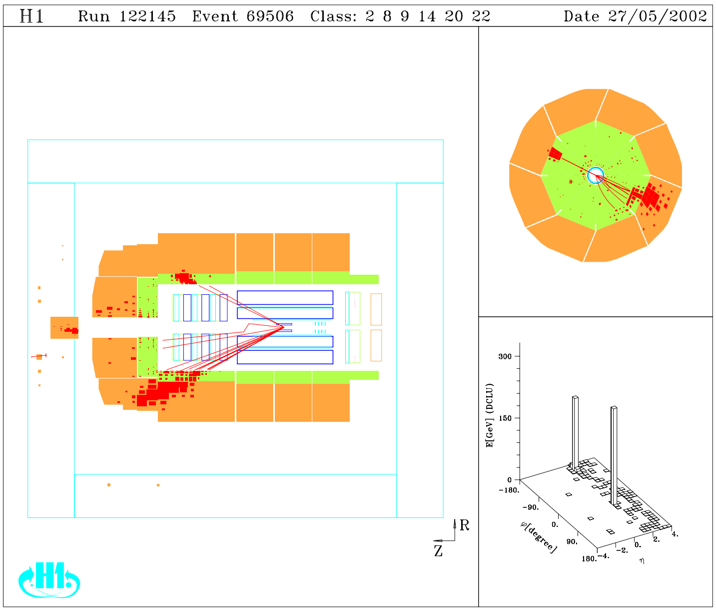

Figure 3.14: Neutral Current event display. The electron is absorbed in the electromagnetic part of the LAr whereas the jet is absorbed in the hadronic and electromagnetic parts of the LAr.

3.7.3 Neutral Current

The NC process (Figure 3.1 (left)) is not expected to contribute very much to the signal sample. A typical event is displayed in Figure 3.14. From the $x-y$ (upper right) view of the figure it can be seen that the event is intrinsically balanced in P_T which is one of the features of the signal if the electron is replaced by muon. The NC contribution from the background may only be significant if the scattered electron is not detected and a muon is produced well separated from the main jet in the hadronisation process. The `RAPGAP` [69] event generator is used to calculate the NC contribution to the background rate.

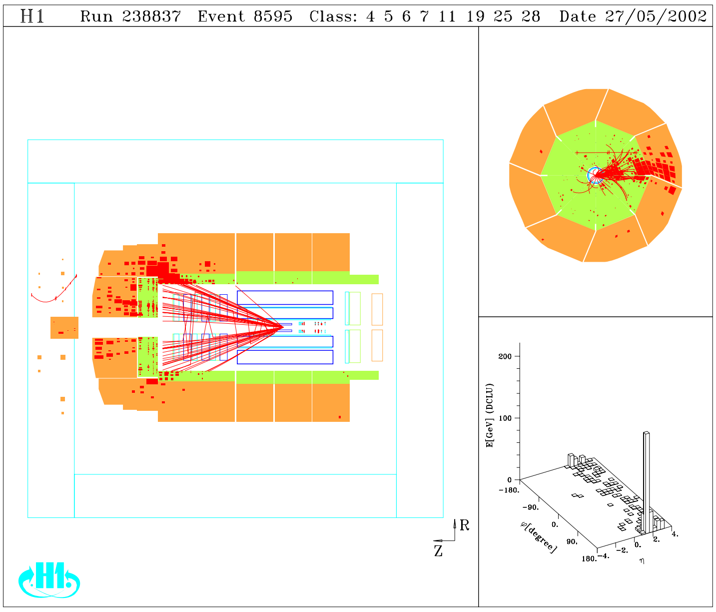

Figure 3.15: Charge Current event display. Particles produced in the hadronic shower are deposited in the LAr.

3.7.4 Charged Current

Figure 3.15 shows a typical event display for a CC event. The CC event enters the signal sample in a similar manner to the NC process – if a particle produced in the hadronisation process is separated from the main body of the jet it may be misidentified as an isolated lepton. The event generator `DJANGO` [70] is used to calculate the background contribution rate of this process.

3.7.5 W Boson Production

A Feynman diagram for W vector boson production decaying to a muon and a neutrino is shown in Figure 3.16. Figure 3.17 shows a typical event display for this process. The `EPVEC` [71] event generator is used to calculate the rate of events expected from the SM. This event generator is used to calculate the heavy vector boson decay. The NLO correction is considered by applying a weight [72].

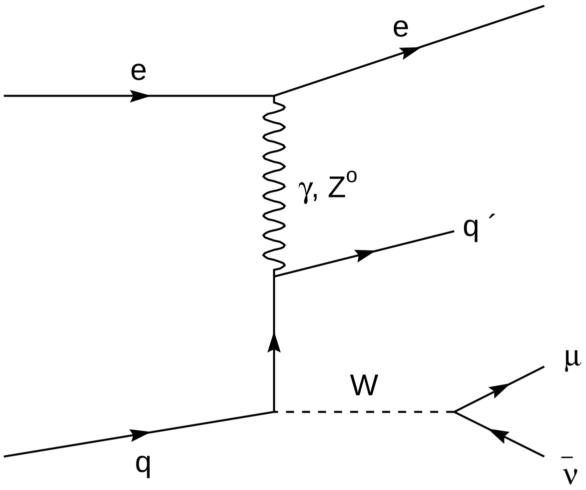

Figure 3.16: *W* production Feynman diagram.

Out of the above background processes, the most dominant one in the *ep* collision is the photoproduction due to the dominance of the propagator term in the cross section. However, this does not contribute a lot to the background since it seldom mimcs the signal process. The NC is the second common proces in the *ep* interaction. This can lead to some significant contribution to the background. The lepton pair process is expected to have a considerable opportunity to be the dominant background since it has at least one muon and one jet in the final state. The *W* production process is one of the rare processes in the *ep* interaction. However, because it ends up with a muon and a jet in the final state it is expected to have some contribution to the background unlike the CC process which is not expected to contribute due to the suppression of its cross section because of the heavy mediating boson and its final state which contains a quark and does not contain a muon except if it is well isolated from the main jet.

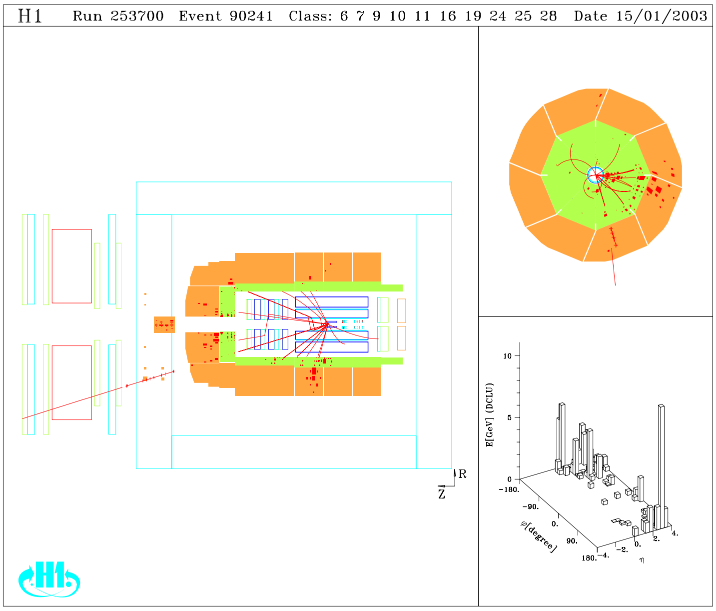

Figure 3.17: *W* production event display. The muon escapes the LAr and traverses through the FMD system.

Chapter 4

General Data Analysis

In this chapter, the initial selections applied in the analysis are outlined. These selections reduce the non-*ep* background events such as beam halo, beam wall and cosmic muon events very significantly. The identification and triggering of muons and the hadronic system are detailed, including their calibration.

4.1 Run Selection and Detector Status

A period of *ep* collisions resulting from one electron and proton injection is called a *luminosity fill.* Luminosity fills are divided and recorded in a series of data taking blocks called *luminosity runs* each lasting up to two hours. Depending on various circumstances, detector conditions may vary resulting in unreliable data measurements from some luminosity runs. For a reliable measurement of data events interesting for this analysis, the following detector components must be fully operational based on their high voltage (HV) conditions:

- the central jet chambers CJC1/2;
- the central proportional chambers (CIP/COP);

- the liquid argon calorimeter (LAr);
- the time of flight (ToF) system;
- the luminosity system.

4.2 Vertex Position

Most events which originate from non-*ep* interactions cannot be related to a primary vertex constructed in the central trackers. A vast amount of such events are ruled out by requiring a primary z-vertex (z_{vtx}) cut for all events to be around the nominal interaction point. This is taken to be $-40 < z_{vtx} < 100$ cm. The extension to the forward region is because a poor reconstruction of the data sample may result in a shifted primary vertex assigned to the events. The above extended z_{vtx} cut assists in including these events in the analysis and this results in an increase of about 5% in the luminosity [73].

4.3 Rejection of Non-*ep* Background

Most of the non-*ep* background events are suppressed using the timing information from the ToF (section 2.6) system in addition to the vertex requirements discussed in the previous section. Additional timing information from the CJCs can help in rejecting such events. This is called T0 and is defined as the drift time of the charged particles to the CJC wires (section 2.3.1). It provides a measurement of when an event occurred. Events which have a time difference greater than 5 ns of the T0 of the bunch crossing are unlikely to come from the *ep* collisions and hence are ruled out.

A set of topological background finders is implemented to reject events originating from cosmic or beam halo muons. By combining the information from different subdetectors these finders search for tagged muons traversing the H1 detector. Cosmic muons are tagged using reconstructed track information from the iron, LAr and CTD, where cosmic muons are more likely to traverse the detector. Beam halo muons are tagged using reconstructed track information parallel to the beam axis [74]. Background finders are also applied to the MC events, although those rejecting more than 1% of the signal MC events are switched off to retain a high selection efficiency of the LFV process.

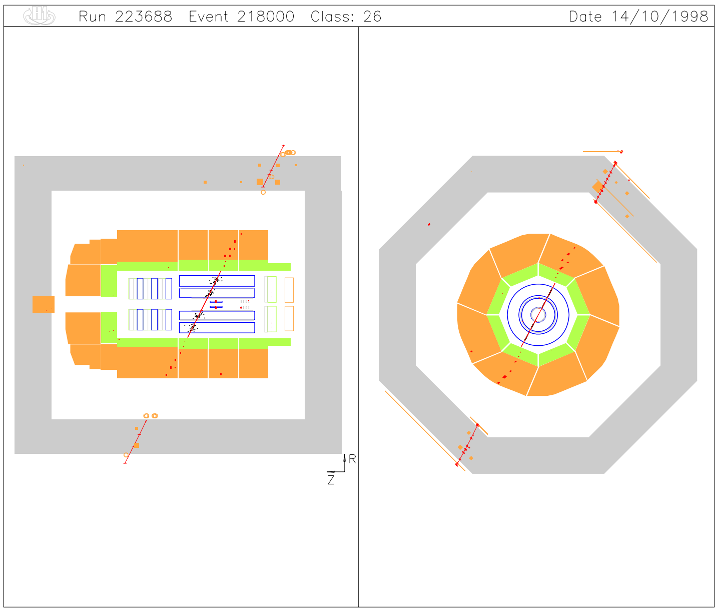

Figure 4.1: Cosmic muon traversing the detector.

4.4 Trigger Selection

As described in section 2.8 the trigger system is employed at H1 to select only interesting *ep* physics events. This section outlines the triggers used in this analysis and describes the calculation of the trigger efficiency.

4.4.1 LAr Trigger

The trigger selection used in this analysis is based on those used for the CC analysis [39]. The timing information from the proportional chambers or the LAr is combined with the trigger elements[1] from the LAr to form L1 subtriggers.

Because of the rare nature of the CC events, the trigger efficiency of the LAr is measured using a *pseudo-CC* data sample – a method based on the removal of the scattered electron in a data sample of NC events from all subdetectors giving events similar to those of the CC process. Since the kinematics of a CC process are different from the NC process (section 3.2.3), events have to be reweighted to those of the CC from its known cross section.

Figure 4.2 shows the trigger efficiency for a MC simulation of the CC process and for the pseudo-CC data as a function of transverse momentum (P_T) and polar angle of the hadronic system. As can be seen from the figure the data are not well described by MC. Hence, the trigger efficiency is determined from the pseudo-CC data events and MC events are reweighted to allow a good comparison to the data. More details of this reweight are given in [39]. This reweight is applied to all background and signal MCs because these processes deposit energy in the LAr except the photoproductio since it contains two jets (section 3.7.2) and this reweight is dedicated to processes with a single jet. The trigger efficiency for the pseudo-CC data is found to be 60% for an imbalance of LAr deposits greater than 12 GeV and 90% for those greater than 25 GeV. Hence, the reweight applied is more significant to events with $P_T^{calo} < 25$ GeV. In the final selection (chapter 7) all events selected are required to have $P_T^{calo} > 25$ GeV.

---

[1] The LAr subtriggers are the following: st66, st67, st71, st75 and st77.

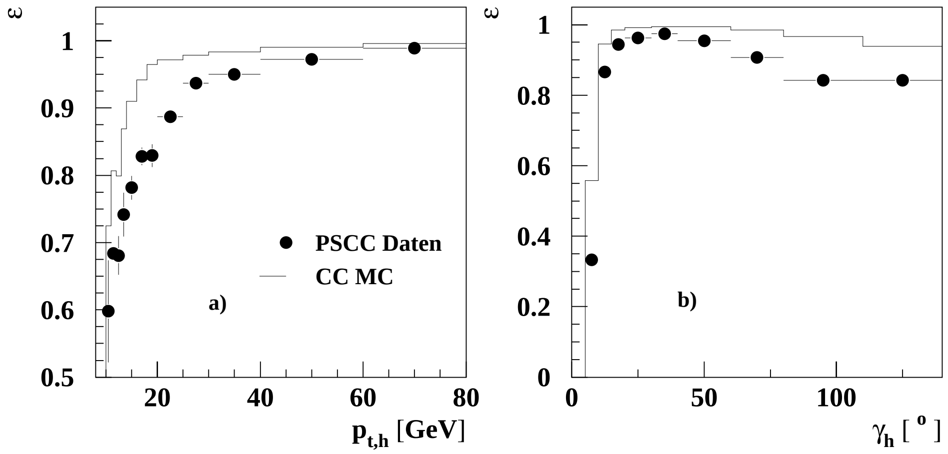

Figure 4.2: LAr trigger efficiency for Pseudo CC data and MC simulation in P_T and polar angle of the hadronic system.

4.4.2 Muon Trigger

The muon triggers[2], described in [62], are also used. L1 muon subtriggers are formed from a coincidence of a muon signal in the muon system with z_{vtx} and central track information. Because of the high background rate a prescale is applied to the muon triggers and this is accounted for in the simulated events by applying a reweight. This reweight is applied to the muon triggers to all background and signal MCs since they contain muons in the final state. The efficiency of some trigger elements as a function of muon polar angle and P_T are shown in Figure 4.3 [62] from which a clear agreement between data and MC can be seen.

---

[2] The muon subtriggers are the following: st15, st19, st22, st34 and st56. st19, st22, st34 and st56 are used in this analysis.

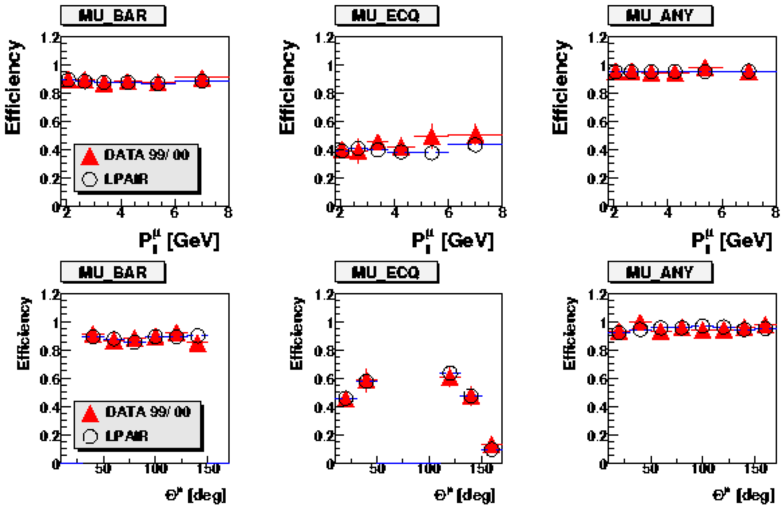

Figure 4.3: Efficiency of trigger elements used for muon triggering as a function of P_T^μ (top) muon polar angle (bottom): muon barrel trigger (left), endcaps muon trigger (middle) and muon trigger signals from endcaps or barrel (right).

4.5 Particle Identification

4.5.1 Muon Identification

Muons penetrate a wide range of detector components, such as the central and forward trackers, LAr, instrumented iron and FMD, because of their low bremsstrahlung radiation and nuclear interaction probability as minimal ionising particles. All muons are required to have greater than 1 GeV in transverse momentum (P_T) since muons with very low P_T are stopped in the LAr due to absorption. All isolated muons must have an energy less than 5 GeV in the electromagnetic part of the LAr in a cylinder of radius 35 cm around the track and 75 cm in the hadronic part. In addition isolated muon tracks must be free from other tracks within a distance of 0.5 in $\eta - \phi$[3] space in the central and forward trackers.

---

[3] $\eta = -\ln(\tan(\frac{\theta}{2}))$ and is called pseudorapidity.

To identify muon candidates a series of grades based on the detector information are used as follows [63]:

- Grade 1 muons have an iron track linked to the central trackers based on a minimum χ^2 probability fit requirement. Muons in this category must have a minimum distance of closest approach (DCA), defined as the perpendicular distance between the centre of gravity of a calorimeter cluster and the tangent to the extrapolated track at its impact point on the front surface of calorimeter, of 100 cm and at least two hits in the central muon system.
- Grade 2 muons also have an iron track linked to the central trackers but are required to be within a distance of 0.5 in $\eta - \phi$ space. In addition, their energy must not exceed 10 GeV in a cone of radius 1 in $\eta - \phi$ space around the track.
- Grade 3 muons require the tail catcher (TC) clusters to match an inner track within a distance of 0.5 in $\eta - \phi$ and the maximum energy of the LAr clusters to be 8 GeV to ensure an isolated muon in the LAr.
- Grade 4 muons have no iron track information and are based on inner track and calorimetry information. In order to avoid the misidentification of hadrons as muons in the calorimeter their minimum separation angle has to be 12° in theta.
- Grade 5 muons are based on clusters in the forward muon system only and require no track information. In this analysis muons with this grade are required to have a good quality track fit in the forward region ($\theta_\mu < 17^\circ$).

4.5.2 Electron identification

Electrons deposit their energy in the electromagnetic part of the LAr as compact isolated clusters. The required maximum DCA is 12 cm. The algorithm used to identify electrons is `QESCAT` [75] which is almost 99% efficient for high transverse momentum electrons. This is, however, restricted to regions where electrons can deposit their energy in the LAr. Regions between LAr modules (cracks) can allow electrons to escape and consequently deposit their energy in the hadronic LAr. Therefore, regions between CB2 and CB3 are ruled out as well as particles penetrating $\pm 2^\circ$ of the ϕ-cracks (transverse view of Figure 2.6).

The electron energy measurement is calibrated using the balance of energy deposits in NC DIS events. The double angle method is used to calculate the energy of the electron. For more details see [39]. The ratio $\frac{E'_e}{E_{DA}}$ is constrained to unity where E'_e is the scattered electron energy and E_{DA} is the energy calculated from the double angle method. Using this constraint, z and the azimuthal ϕ are chosen as calibration parameters. The role of electrons shows up in this analysis in the NC events. The rejection of these events in the final selection (chpater 7) requires the number of isolated electrons to be zero.

4.5.3 The Hadronic System

As is described in the previous chapter individual quarks cannot exist individually – a property known as confinement. The fragmentation of quarks and gluons produces showers of particles. Each particle in the hadronic system has a small P_T with respect to the shower axis. In order to identify jets the k_T algorithm [77] is used where the minimal jet transverse energy is 5 GeV and its minimal cone radius is 1.

The four-vector of the hadronic system X is reconstructed from the information from the trackers, LAr, SpaCal and TC. The `FSCOMB` algorithm [76] is used to measure the P_T of each particle by combining information from the trackers and calorimeters. Particles with low P_T are better measured in the tracking system. `FSCOMB` assigns a cylinder of radius 25 cm around the impact point of the track in the electromagnetic part of the LAr calorimeter and 50 cm in the hadronic part. If the P_T of the track is less than 2 GeV then the energy of the cylinder surrounding the track is excluded and the track energy is added to overall energy.

The calibration of the hadronic final state uses the balance between the hadronic final state transverse momentum and that of the scattered electron in NC DIS events [78], i.e $p_{T,bal} = p_{T,HFS}/p_{T,e}$. This ratio should equal 1 and is used iteratively to correct the MC simulation so that it agrees with the data. The hadronic calibration is significant since the signal and background processes contain hadronic final states.

Chapter 5

Kinematic Variables and Background Processes

The characteristics of the kinematic variables used in the analysis are described in this chapter. These variables are used to understand the behaviour of the LQ and its decay products in the detector. This allows the reduction of the contributing background processes, keeping the selection efficiency of the signal process as high as possible, if appropriate selections are applied. In this chapter the selections are dedicated to identifying events containing muons. The distribution of each variable is displayed for a basic muon selection which requires a high transverse momentum muon (P_T^{μ}) since the LQ decays into a muon with high P_T values. After applying the initial selections outlined in the previous chapter, which select *ep* physics events and identify electrons, muons and the hadronic system, the following selections are performed as a first level selection set:

- The calorimetric transverse momentum (P_T^{calo}) is required to be greater than 12 GeV for the trigger reasons mentioned in the previous chapter.
- The muon transverse momentum (P_T^{μ}) is required to be greater than 10 GeV.

As mentioned above muons with high P_T^{μ} are expected from the LQ decay.

- The muon polar angle is restricted to $10° < \theta_\mu < 140°$. The upper cut is to avoid the backward region where muons are poorly reconstructed [1]. The lower cut is applied to avoid the high track mutiplicity and the background in the forward region.

In this chapter different kinematic variable distributions are shown for the background and the LQ signal MC processes. The LQs shown are generated for e^-p and e^+p collisions. The $\tilde{S}_0{}^R$ LQ type with $F = 2$ is generated at 250 GeV for e^-p collisions and the V_0^L with $F = 0$ is generated for e^+p collisions at the same mass. The event selections applied yield 81 muon data events compared to 66.7 ± 6.4 events expected from the MCs for the e^+p interactions. The same selection applied for the e^-p collisions yields 21 data and 15.9 ± 1.7 MC events. In the next chapter selections for isolated muon events are applied. The background process kinematics are explained in this chapter while the signal process is explained in more detail in the next chapter.

5.1 P_T^{calo}

P_T^{calo} is the transverse momentum measured and reconstructed in the LAr, SpaCal and TC. Isolated muons do not contribute very much to P_T^{calo} since they do not deposit enough energy in the calorimeters and their P_T measured by the trackers is not included in this quantity. The P_T^{calo} of the LQ events is expected to correspond to approximately half of the LQ mass since it represents the P_T measured by the calorimeters and this mostly measures the hadronic energy deposits coming from the decay quark. P_T^{calo} distributions for different background processes after the first

---

[1] This can be attributed to the BBE which does not have a hadronic section (section 2.4.1) and therefore muons can be misidentified as pions.

level selection (muon selection) are shown in Figure 5.1. The sum of all background processes (SM contribution) is shown as a solid black line. The P_T^{calo} distribution for e^-p data is shown on the left and that for the e^+p data is shown on the right. The signal LQ is displayed as a dashed line and is shown for $\tilde{S}_0{}^R$ (e^-p collisions) and V_0^L (e^+p collisions) LQs with 250 GeV mass. The signal MC is not symmetric around the peak. The distribution falls considerably above approximately half of the LQ mass. This shape is a feature of P_T distributions corresponding to half of the LQ mass and is called a *Jacobian peak*[2]. The SM falls steeply with P_T^{calo} which allows the rejection of most background events as will be discussed in chapter 7.

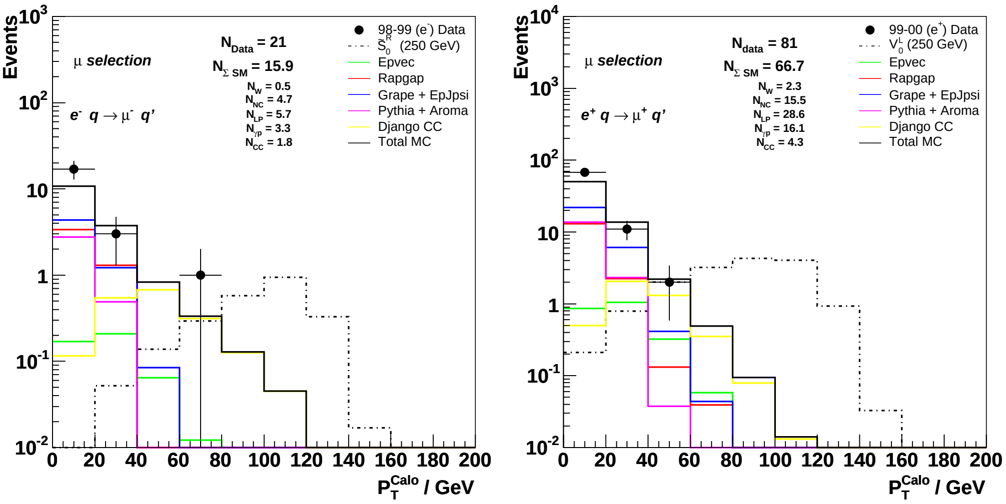

Figure 5.1: Distributions of P_T^{calo} after the muon selections for e^-p (left) and e^+p (right) collisions. Since the muons barely deposit their energy into the calorimeters they do not contribute very much to this quantity. The SM expectation falls steeply with P_T^{calo}. Most background processes have low P_T^{calo}.

---

[2] This can be understood from the cross section falling off rapidly with P_T from

$$\frac{d\sigma}{dP_T} = \frac{d\sigma}{d\cos\theta} \cdot \frac{2P_T}{M_{LQ}} \cdot \frac{1}{\sqrt{(M_{LQ}/2)^2 - P_T^2}}$$

which shows that the cross section falls off rapidly above $P_T \approx \frac{M_{LQ}}{2}$. More details are given in [32].

5.2 P_T^X

P_T^X is the transverse momentum of the hadronic final state. Since the LQ decays into a muon and a quark each with equal transverse momentum, P_T^X is expected to correspond to approximately half of the LQ mass and to have a similar distribution to the transverse momentum of the muon. `FSCOMB` is used to calculate P_T^X of the hadronic system (section 4.5.3). This algorithm takes the track information into account and since the muons barely contributes to P_T^{calo}, $P_T^{calo} \approx P_T^X$. The distributions for P_T^X in the muon selection are displayed in Figure 5.2. As can be seen in the figure the SM expectation falls steeply with P_T^X. As mentioned in chapter 2 the P_T is measured from the trackers and it is inversely proportional to the curvature[3]. The accuracy of track measurement becomes weaker as the tracks become more stiff due to their high momentum.

5.3 P_T^μ

P_T^μ is the transverse momentum of the muon. Since the LQ decays into a muon and a quark each with equal transverse momentum, P_T^μ is expected to correspond to approximately half of the LQ mass. The momentum of the muon is calculated from the curvature of the muon track in the trackers. P_T^μ is obtained from the total momentum and the polar angle measured. Distributions for P_T^μ after the muon selection are displayed in Figure 5.3. As can be seen in the figure the SM expectation falls steeply with P_T^μ.

---

[3] The curvature is inversely proportional to the momentum of the particle, i.e.

$$C \propto \frac{1}{p}$$

where C is the curvature. From this equation it can be seen that the more stiff the track is the higher the momentum of the particle. For straight tracks the track momenta is measured with a high error.

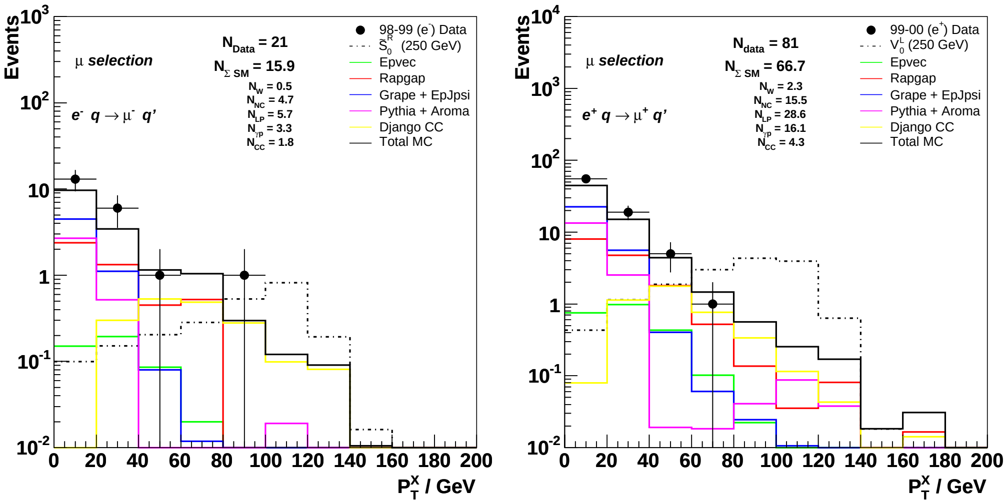

Figure 5.2: P_T^X distributions after the muon selections for e^-p (left) and e^+p (right) collisions. This looks similar to the P_T^{calo} (Figure 5.1) especially for the signal MC. In P_T^X the track information is included in contrast to P_T^{calo} which makes them similar in the case of the LQ signal which contains an isolated muon.

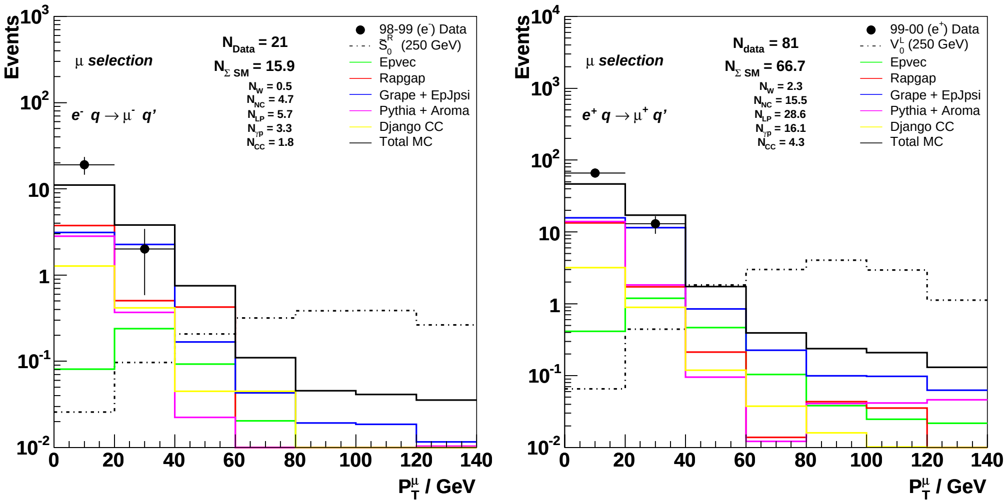

Figure 5.3: P_T^μ distributions after the muon selections for e^-p (left) and e^+p (right) collisions. The P_T^μ is calculated from the curvature of the muon track. The SM expectation falls steeply with P_T^μ.

5.4 P_T^{miss}

All particles have to be balanced in the transverse vector sum as in the initial state interaction the incoming electron and proton are balanced in the transverse component. The missing transverse momentum, P_T^{miss}, is calculated using the vector sum of all identified particles in the detector and hence the transverse component of this quantity is calculated. This is a useful quantity to calculate when events contain neutrinos which are undetectable since their P_T should balance the calculated P_T of the detected particles. The distributions of P_T^{miss} after the muon selections are displayed in Figure 5.4 for both e^-p and e^+p interactions. Note that most of the LQ events have low P_T^{miss} values since LQs do not decay into neutrinos. Photoproduction (PYTHIA+AROMA) and NC background (RAPGAP) processes exhibit a similar distribution unlike the CC (DJANGO) which contains a neutrino. The P_T^{miss} of the CC (DJANGO) events should be equal to the P_T^X since neutrinos and jets are balanced. This figure can be compared with Figure 5.2. The W-decay (EPVEC) shows a peak at around 40 GeV. The W-decays to μ and $\bar{\nu}$ (section 3.7.5) and the P_T^{miss} is calculated from the imbalance in the 4-vector of all particles. Figure 5.3 shows a peak at the same value for the P_T^{μ} which is half of the W mass (Table 3.2).

5.5 Acoplanarity

Acoplanarity, $\Delta\phi_{\mu-X}$, is a measure of the azimuthal balance of an event. Figure 5.5 illustrates how the acoplanarity is defined. The azimuthal angle, ϕ, of the hadronic system used to calculate $\Delta\phi_{\mu-X}$ is taken from the full hadronic system. The distributions of $\Delta\phi_{\mu-X}$ after the muon selection are depicted in Figure 5.6. The lepton pair (GRAPE+EPJPSI) events peak at approximately 180° since these events contain one muon which is back-to-back with the hadronic system. This can be seen from the $r-\phi$ view of the event display in Figure 3.12. In NC (RAPGAP), photopro-

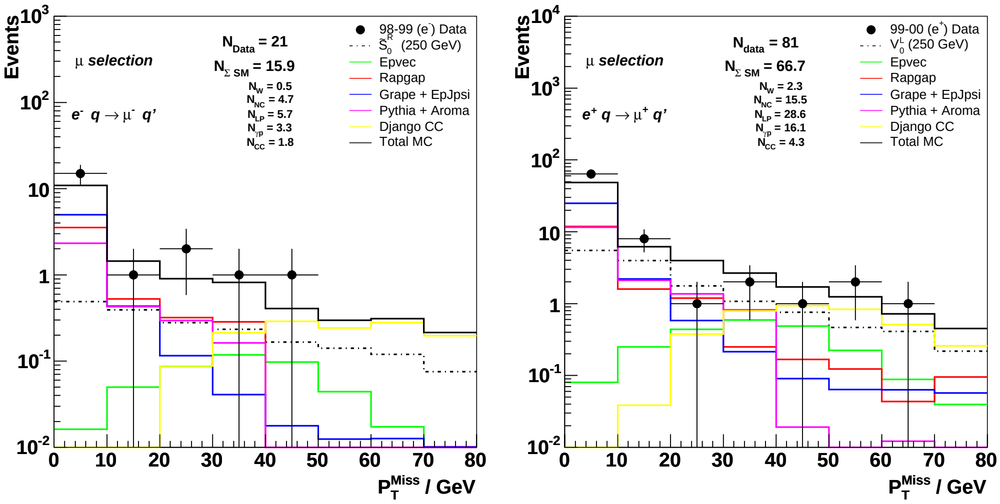

Figure 5.4: P_T^{miss} distributions after the muon selections for e^-p (left) and e^+p (right) collisions. Most W-decay (EPVEC) and CC (DJANGO) events have high P_T^{miss} values since they contain neutrinos in the final state.

duction (PYTHIA+AROMA), W-decay (EPVEC) and CC (DJANGO) events this variable is almost evenly distributed. The LQ signal peaks at around 180° showing its back-to-back nature. The smaller peak of background processes at lower angles is due to events with no jets.

5.6 $\frac{V_{ap}}{V_p}$

$\frac{V_{ap}}{V_p}$ is a ratio which gives a measure of the azimuthal balance of the event like acoplanarity. Its components are defined as follows:

$$V_p = \sum_i \frac{P_T^X \cdot P_T^i}{P_T^X} \quad \text{for} \quad P_T^X \cdot P_T^i > 0 \quad , \tag{5.1}$$

$$V_{ap} = -\sum_i \frac{P_T^X \cdot P_T^i}{P_T^X} \quad \text{for} \quad P_T^X \cdot P_T^i < 0. \tag{5.2}$$

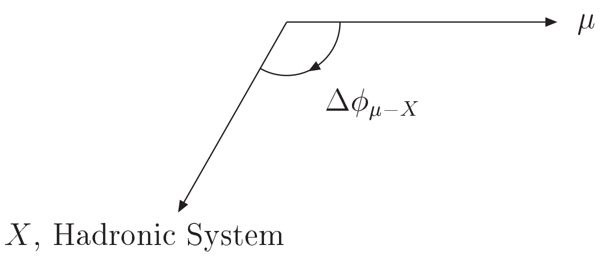

Figure 5.5: Acoplanarity, $\Delta\phi_{\mu-X}$, is defined as the angle between the muon and the hadronic system in $r - \phi$.

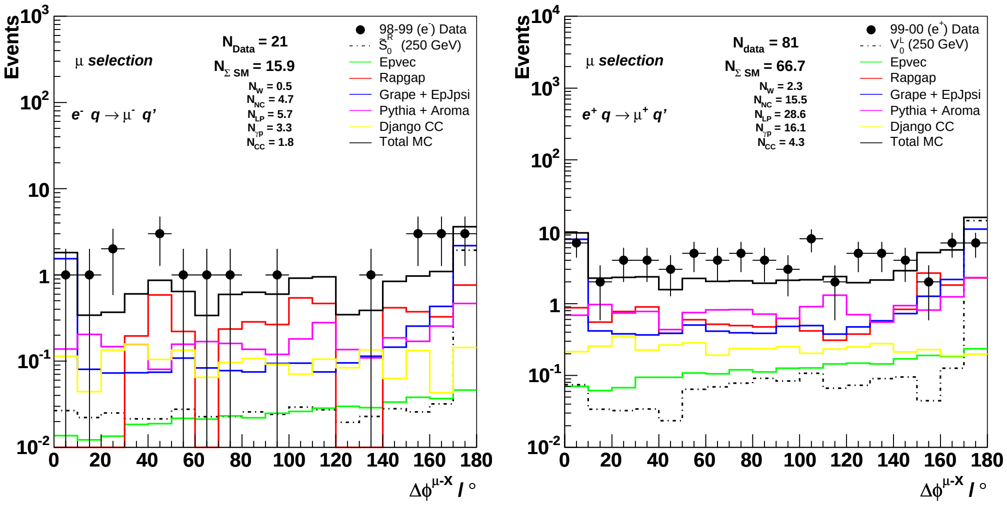

Figure 5.6: $\Delta\phi_{\mu-X}$ distribution after the muon selections for e^-p (left) and e^+p (right) collisions. The lepton pair (GRAPE+EPJPSI) events show a peak at about 180° indicating that the highest P_T^μ muon balances the hadronic final state in the final state. The smaller peak at very low angles are for events with no jets.

V_p is the sum of the measured transverse momentum parallel to the hadronic system vector P_T^X, while V_{ap} is the sum of the measured transverse momentum anti-parallel to the hadronic system vector. The sums are performed over each particle i of the final state [78]. The distributions of $\frac{V_{ap}}{V_p}$ in the muon selections are displayed in Figure 5.7. This variable shows the isotropy of events in the LAr. The lack of isotropy is shown for the LQ signal, W-decay (EPVEC), lepton pair (GRAPE+EPJPSI) and the CC (DJANGO) events unlike the photoproduction (PYTHIA+AROMA) and NC (RAPGAP) events, where the events are distributed isotropically in the LAr.

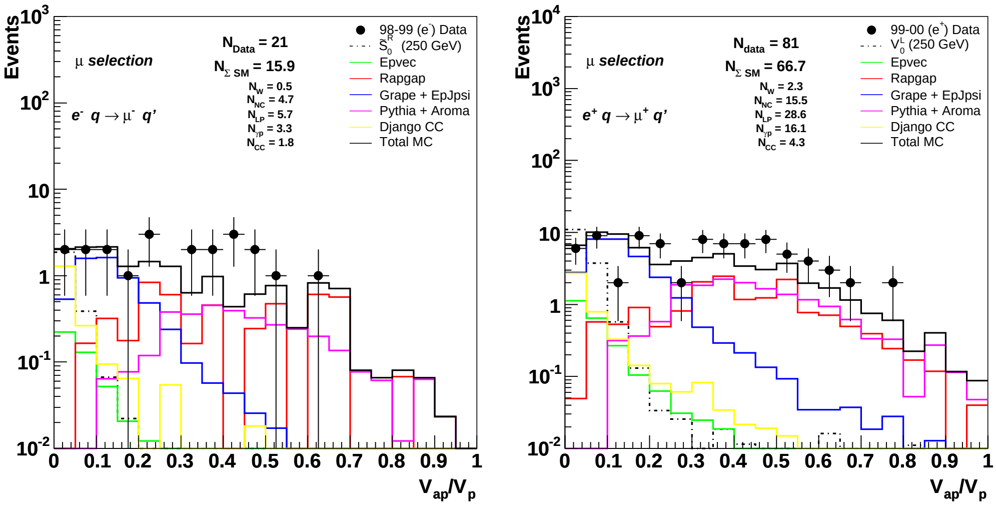

Figure 5.7: $\frac{V_{ap}}{V_p}$ distribution after the muon selections for e^-p (left) and e^+p (right) collisions. The lack of isotropy in the LAr can be seen in the lepton pair (GRAPE+EPJPSI), CC (DJANGO) and W-decay (EPVEC) events which contain particles which escape the LAr in their final state such as neutrions and muons. Selecting events with $\frac{V_{ap}}{V_p} < 0.3$ removes the majority of background events coming from photoproduction (PYTHIA+AROMA) and NC (RAPGAP) processes as will be described in the next chapter.

5.7 D_{jet} and D_{track}

The isolation of the identified muon with respect to the hadronic system is an important criterion of the required LFV signal. This is determined using D_{jet} and D_{track} variables. D_{jet}, which is the distance between the muon track and the axis of the closest hadronic jet in the $\eta - \phi$ plane, is defined as

$$D_{jet} = \sqrt{(\Delta\eta_{track-jet})^2 + (\Delta\phi_{track-jet})^2}. \tag{5.3}$$

D_{track} is the distance from the muon track to the closest track in $\eta - \phi$ space and is defined analogously to D_{jet}. This quantity ensures the isolation of the muon from separated parts of the hadronic system and also any other leptons in the event.
The distributions of D_{jet} and D_{track} in the muon selection sample are displayed in Figure 5.8. Note that for the signal events the peak is at around π (≈ 3.1) which shows clearly the LQ decaying back-to-back into a muon and a quark. The D_{track} distribution also shows a concentration of events at π although it is less peaked compared to D_{jet} due to the spread of the jet. The lepton pair (GRAPE+EPJPSI) distribution shows a similar behaviour to the signal. An identified lepton is termed "isolated" if it is well separated from other tracks and jets in the event. The selections $D_{jet} > 1.0$ and $D_{track} > 0.5$ are used as developed for the isolated lepton searches [73].

5.8 θ^{μ} and θ^{X}

Since the proton beam has higher energy than the electron beam the LQ produced in the interaction is boosted in the forward direction and hence also its decay products, i.e. the muon and the hadronic final state, X. Figure 5.9 shows the distributions of polar angle of the muon and the hadronic system. These variables are measured from the trackers (section 2.3.1). For most of the background events the polar angle

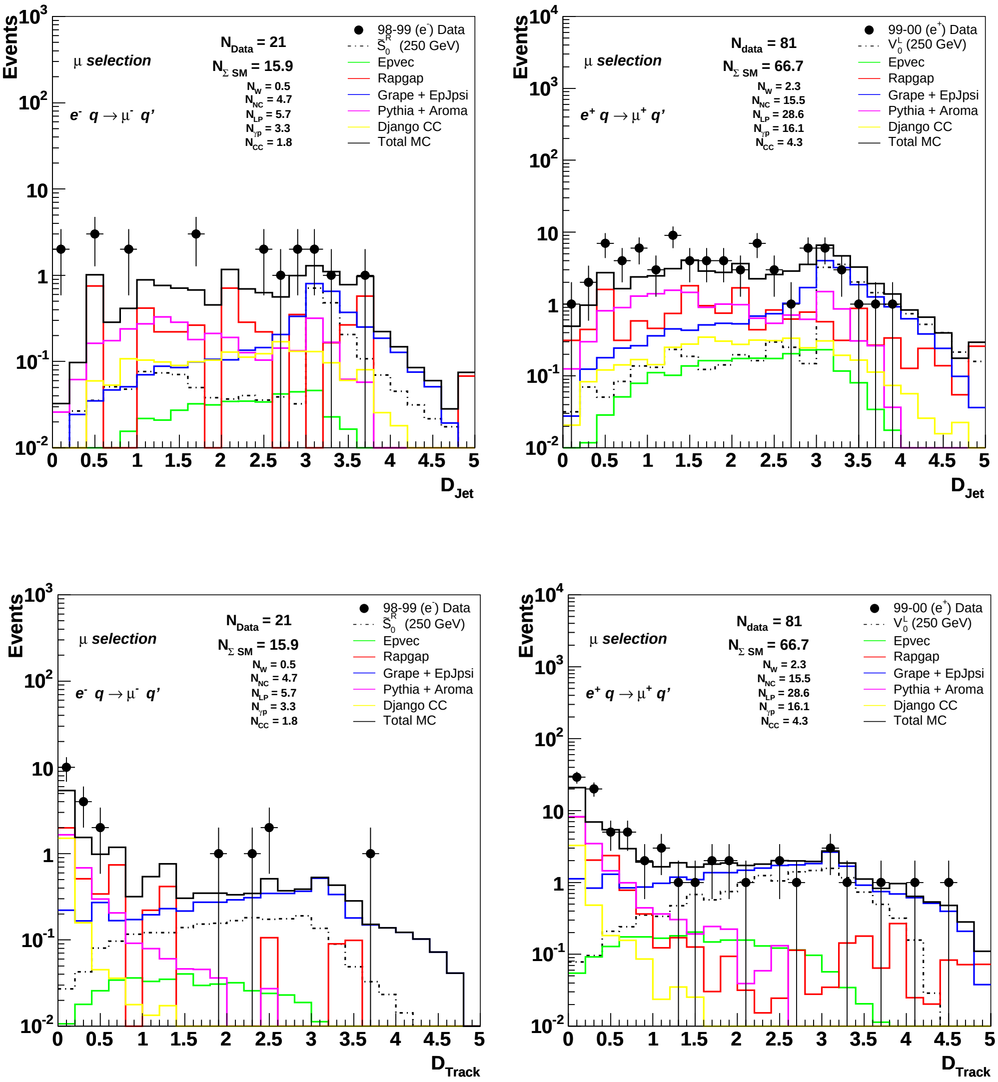

Figure 5.8: D_{jet} (top) and D_{track} (bottom) distributions after the muon selections for $e^{-}p$ (left) and $e^{+}p$ (right) collisions. The lepton pair (GRAPE+EPJPSI) events show a peak at around π in the D_{jet} and D_{track} since the highest P_T^{μ} and the hadronic system are back-to-back.

has low values, this is due to the asymmetric nature of the *ep* collision.

In this selection set some discrepancy between data and SM MCs is shown at high $\frac{V_{ap}}{V_p}$ (Figure 5.7) values and at events with $\Delta\phi_{\mu-X} < 140°$ (Figure 5.6). This discrepancy seems to mainly come from the first bin in the P_T^{calo} distribution (Figure 5.1). However, this region of phase space is not required in the final selection (chapter 7).

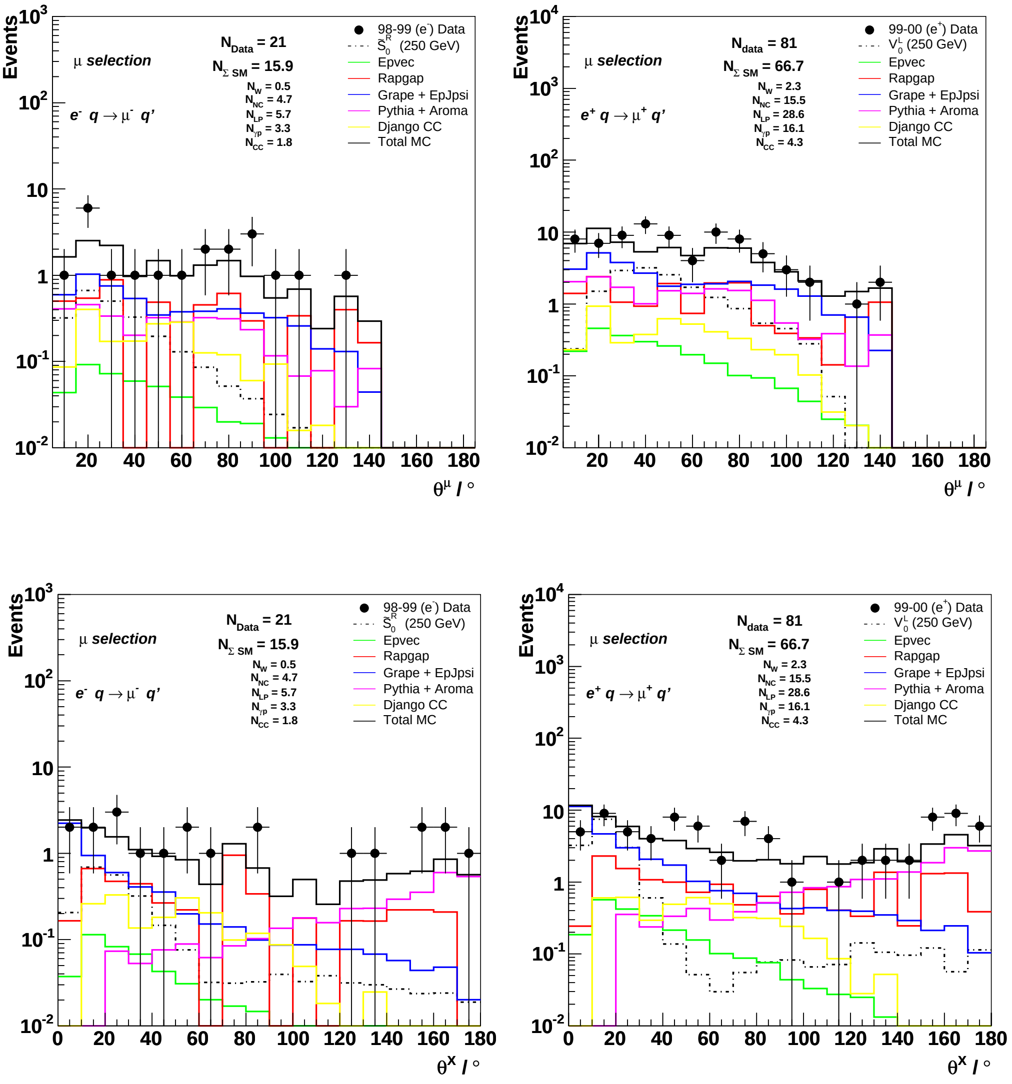

Figure 5.9: θ^{μ} (top) and θ^{X} (bottom) distributions after the muon selections for $e^{-}p$ (left) and $e^{+}p$ (right) collisions.

5.9 Reconstructed Mass

The DIS Lorentz invariants Q^2, y and x are used to determine the leptoquark mass, M^{LQ}, with

$$M^{LQ} = \sqrt{xs} = \sqrt{\frac{Q^2}{y}}\ . \tag{5.4}$$

As was mentioned in chapter 2, the muon barely interacts with matter. Hence, the energy of the muon is not measured as well as the electron energy. Therefore, the dependence on the electron method, taking the angle and energy of the outgoing muon, to reconstruct the mass and the other Lorentz invariants variables does not give accurate results. The reconstruction of Q^2, y, and x is based on the double angle method, to minimise the dependency on the hadronic and muonic energy measurement. For a LQ decaying into a muon and a quark, the angle of the outgoing muon and the angle of the highest transverse momentum (P_T) jet are taken to reconstruct the mass of the LQ.

10,000 $eq \to LQ \to \mu + q'$ events were generated in steps of 25 GeV of LQ mass between 75 GeV and 400 GeV with different coupling constants. For LQs with masses far beyond the kinematic limits 1000 events were generated with $\lambda_{L,R} = 1.0$ and mass of 1 TeV. Figure 5.10 shows the mass distrbution of a 250 GeV vector LQ generated for e^+p collisions and Figure 5.11 shows the reconstructed scalar LQ masses of 150, 250 and 350 GeV for e^-p collisions. The 350 GeV LQ does not show a peak at its generated value whereas the other plots show peaks at their generated values. This is because LQs with masses greater than the centre of mass energy are produced resonantly from the sea quarks with their low x values (section 3.2.4 and Eq. 5.4) and also the u-channel contribution (Figure 3.9) to the signal becomes more significant. The mass distribution can be understood as a convolution of the Breit-Wigner distribution of the resonantly produced LQ at large masses with the parton distribution function (pdf) of the proton[4]. As the mass increases and gets close to the kinematic limit the pdf falls steeply (Figure 3.5) and hence the tail of the reconstructed LQ grows and the peak starts diminishing. The tail is more pronounced in Figure 5.10 than the other cases because the LQ was produced with a higher coupling constant, $\lambda_L = 0.6$, whereas the LQ in top right plot of Figure 5.11 was produced with $\lambda_L = 0.1$. This shows the sensitivity of the distribution to the coupling constant especially as the mass gets closer to the kinematic limit (Eq 3.28, 3.29, 3.30). This is attributed to the fall in the pdf as the mass gets closer to the kinematic limit.

---

[4] The Breit-Wigner equation describes the distribution of events around a resonant peak. It is used to describe the mass of particles or cross section of decay processes. Its details can be found in [32]. It mainly depends on the width of the mass distribution and is given by

$$N = \frac{\Gamma}{(M - M_r)^2 + (\frac{\Gamma}{2})^2} \tag{5.5}$$

where M_r is the mean mass value, M is the mass distribution and Γ is the width of the distribution.

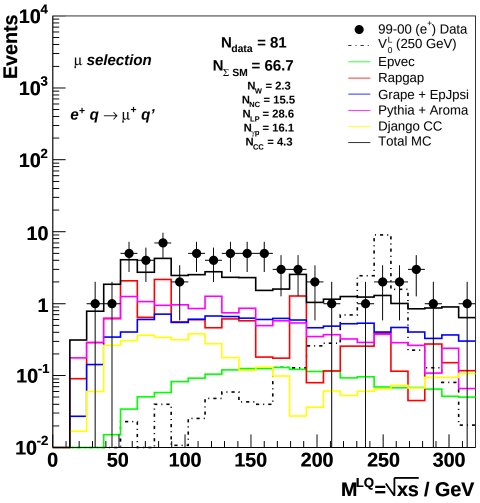

Figure 5.10: LQ mass distribution for e^+p at mass = 250 GeV reconstructed using the double angle method after the muon selections. The broad peak can be understood from a convolution of the Breit-Wigner distribution of the LQ mass with the pdf of the proton. It is caused by the resonantly produced LQ events from the incoming leptons and the sea quarks which have low Bjorken-x values. A high coupling constant was used to generate the LQ. Compare this with plots on the next page. This shows the effect of the coupling constant on LQ masses near the kinematic limits.

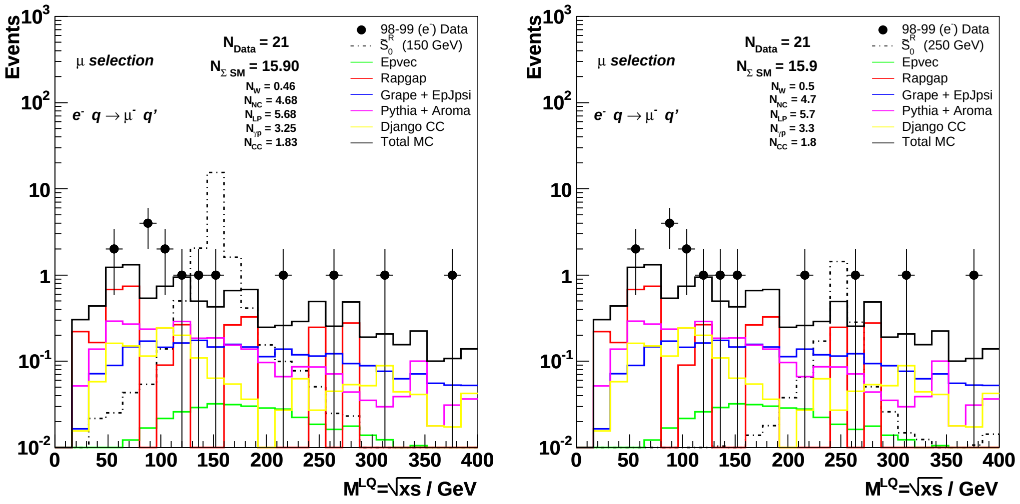

(a) $M^{LQ} = 150$ GeV **(b)** $M^{LQ} = 250$ GeV

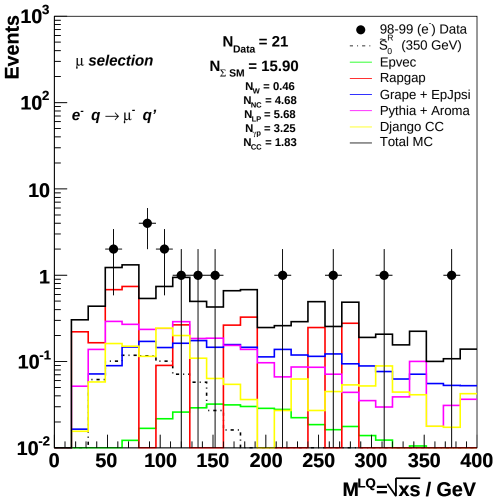

(c) $M^{LQ} = 350$ GeV

Figure 5.11: Different LQ mass distributions for e^-p at masses = 150, 250 and 350 GeV reconstructed using the double angle method after the muon selections. The broad peak for the LQ of mass 350 GeV shows that the LQ is produced from the tail of the Breit-Wigner distribution accessible into the kinematic region. The 350 GeV mass corresponds to $x > 1$ (Eq. 5.4) and hence cannot peak at the generated value.

Chapter 6

Isolated Muon Selection

In this chapter a set of selections is applied to select only events with isolated muons. The distributions of the kinematic variables defined in the previous chapter are displayed for the isolated muon selection. More emphasis is given to understand the LQ LFV signal. The event selections applied yield 5 data events compared to 6.5 ± 0.7 expected MC events in the e^-p sector. The same selections applied in the e^+p sector yield 21 data events compared to 28.3 ± 2.5 MC events.

6.1 Selection Criteria

The main cut employed after selecting muon events selects events at low values of $\frac{V_{ap}}{V_p}$. A cut of $\frac{V_{ap}}{V_p} < 0.3$ is applied to remove most of the photoproduction and NC background events. Also, the isolation criteria mentioned in the previous chapter are applied to ensure the isolation of the muons. These are namely $D_{jet} > 1.0$ and $D_{track} > 0.5$. Events in this selection must contain at least one isolated muon. Table 6.1 summarises the selections applied in this level. After applying these criteria, this selection mainly contains events with lepton pair muons from the background processes. The distributions of the kinematic variables of the muon events are presented in figures later in this chapter. The combined SM prediction is given by the open histogram and the brown band containing the SM prediction line represents the summed SM error without including the experimental systematic errors. The signal component is given by the hatched histogram. Descriptions of the kinematic variables are given showing the differences between LQs below and above the centre of mass energy.

Variables	cuts applied
P_T^{calo}	> 12 GeV
P_T^{μ}	> 10 GeV
θ^{μ}	$> 10°$, $< 140°$
number of isolated muons	≥ 1
$\frac{V_{ap}}{V_p}$	< 0.3
D_{track}	> 0.5
D_{jet}	> 1

Table 6.1: Selections applied in the second level selection to select isolated muon events. First level selections (P_T^{calo}, P_T^{μ}, θ^{μ}) which were dedicated to selecting muon events are included in this set.

6.2 Discussion

Figure 6.1 shows P_T^{calo} distributions after the isolated muon selections for e^-p and e^+p collisions. Since the e^-p interaction has less luminosity ($\mathcal{L} = 13.8\ pb^{-1}$) than the e^+p interaction ($\mathcal{L} = 66.0\ pb^{-1}$) the e^-p plot shows fewer events in the data and background processes. The majority of these events are lepton pair events since the cuts applied in this selection are dedicated to identifying isolated muon events. Selecting events with $P_T^{calo} > 25$ GeV rejects a lot of background events (next chapter). The distribution of the signal events are not symmetric around the peak. This peak is called a *Jacobian peak*. A similar feature will be shown throughout this

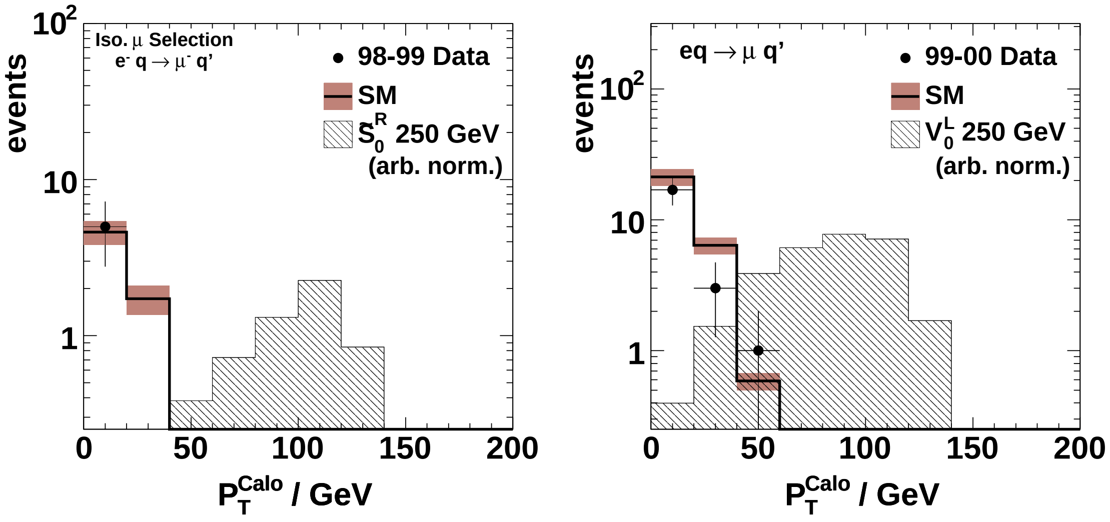

Figure 6.1: P_T^{calo} distributions after the isolated muon selections for e^-p (left) and e^+p (right) collisions with scalar and vector LQs respectively.

chapter for the P_T^X and P_T^μ distributions.

Figure 6.2 shows P_T^X distributions for e^-p and e^+p collisions. The data and the SM expectation falls steeply with P_T^X. The signal events are distributed around half of the generated LQ mass ($P_T^X \approx \frac{M_{LQ}}{2}$) for a LQ generated with masses below the kinematic limit. Figure 6.3 shows the P_T^X for a LQ with a mass of 350 GeV. This figure shows that LQs of masses greater than the kinematic limit have P_T^X less than half of the generated LQ mass. Recall from the previous chapter that the incoming electron interacts resonantly with sea quarks which have low Bjorken-x values and off-resonantly (u-channel) resulting in low mass LQs.

Figure 6.4 shows the P_T^μ distributions for e^-p and e^+p collisions. The plot is for the highest P_T isolated muon (if more than one exist). The signal is distributed at around half of the LQ mass ($P_T^\mu \approx \frac{M_{LQ}}{2}$). Figure 6.5 shows the P_T^μ distributions for e^-p collisions where the signal is for a LQ with a mass of 350 GeV. This can be

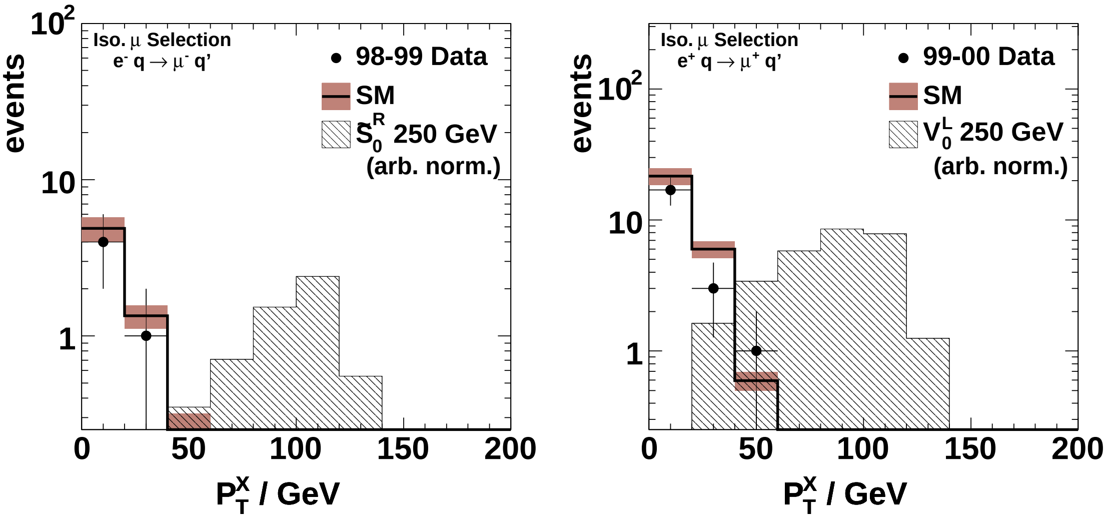

Figure 6.2: P_T^X distributions after the isolated muon selections for e^-p (left) and e^+p (right) collisions. The LQ mass is 250 GeV.

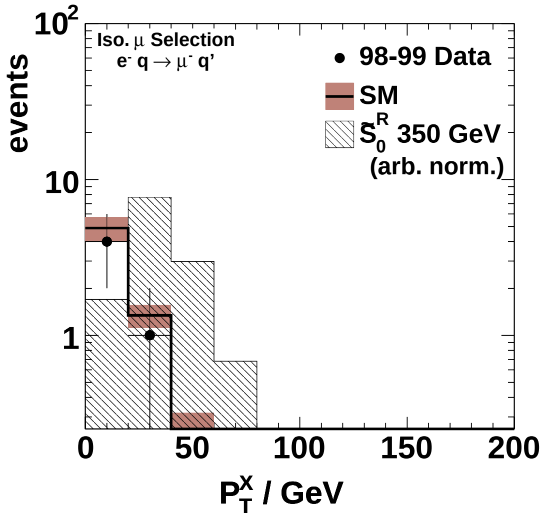

Figure 6.3: P_T^X distributions after the isolated muon selections for e^-p collisions. The LQ generated mass is 350 GeV.

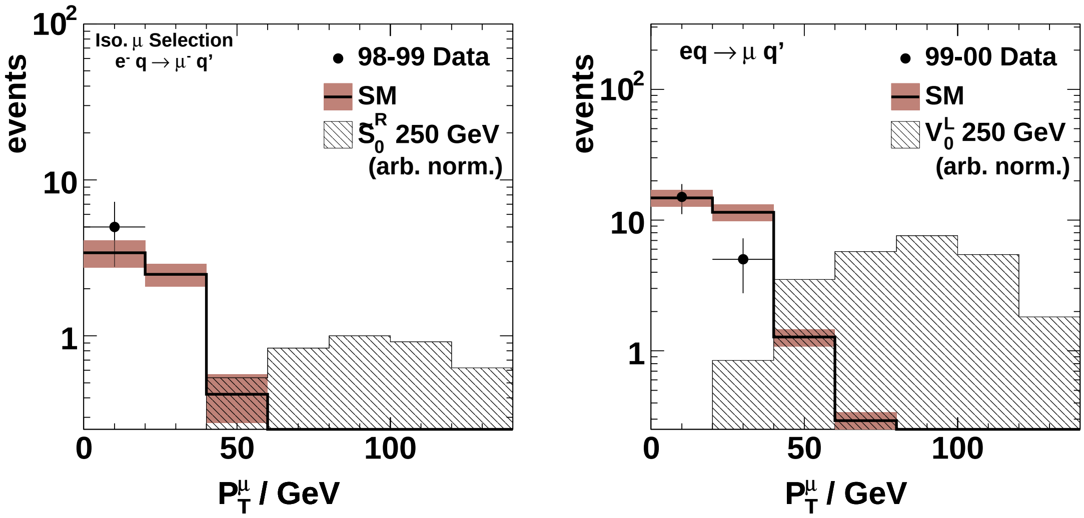

Figure 6.4: P_T^μ distributions after the isolated muon selections for e^-p (left) and e^+p (right) collisions.

compared with the P_T^X distribution of the same events (Figure 6.3) to show that LQs of masses greater than the kinematic limit have a P_T^μ less than half of the generated LQ mass.

Figure 6.6 shows the P_T^{miss} distributions for e^-p and e^+p collisions. Most of the signal process events have low P_T^{miss} values. As mentioned in the previous chapter this is calculated from the imbalance of the P_T of all particles in the events. High values of P_T^{miss} for the signal LQ are due to high P_T^μ measurements. The tracks of these particles are stiff (almost straight). Hence they are measured with larger uncertainties leading to uncertainties in the P_T^{miss} values. Compare this figure with the next figure (Figure 6.7) which shows the P_T^{miss} for a LQ with masses beyond the kinematic limit. The P_T^{miss} distribution is less broadened than those for LQs with masses lower than kinematic limits since in that case (Figure 6.7) most muons events have lower P_T^μ. Therefore, the uncertainties on P_T^μ (and hence P_T^{miss}) are less.

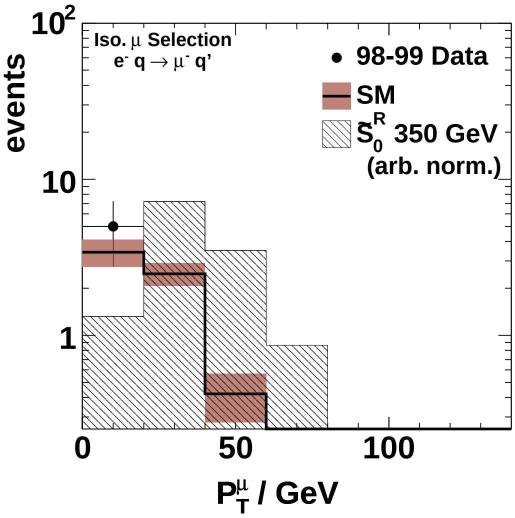

Figure 6.5: P_T^μ distributions after the isolated muon selections for e^-p collisions.

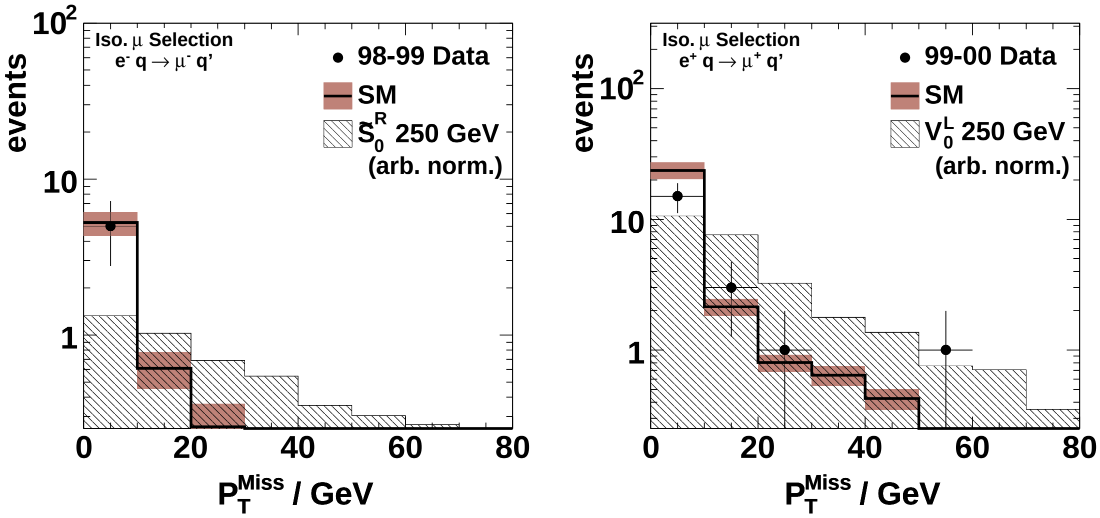

Figure 6.6: P_T^{miss} distributions after the isolated muon selections for e^-p (left) and e^+p (right) collisions.

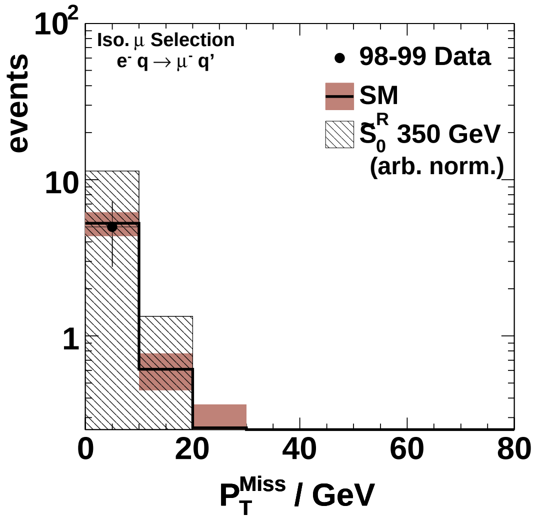

Figure 6.7: P_T^{miss} distributions after the isolated muon selections for e^-p collisions.

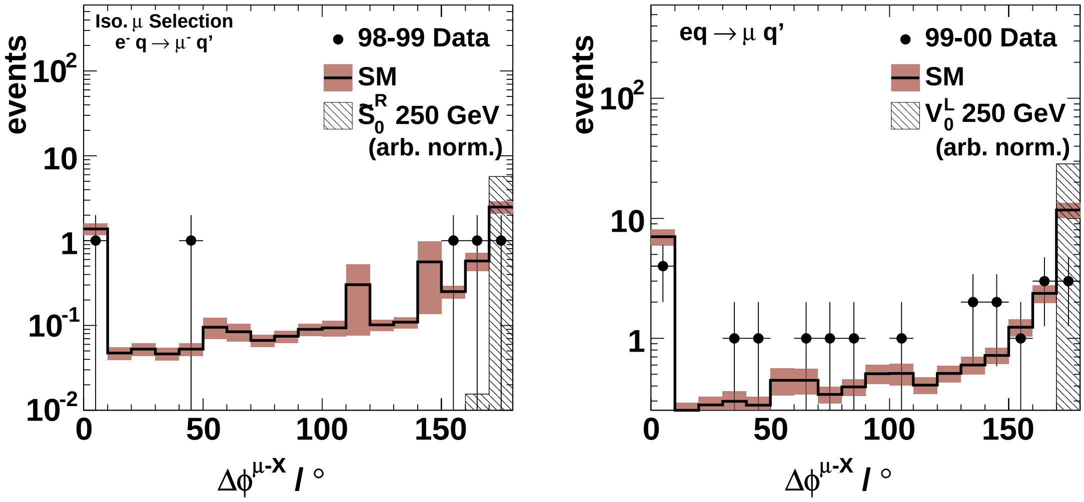

Figure 6.8: $\Delta\phi_{\mu-X}$ distributions after the isolated muon selections for e^-p (left) and e^+p (right) collisions. The smaller peak at very low angles are for events with no jets.

Figure 6.8 shows the $\Delta\phi_{\mu-X}$ distributions for e^-p and e^+p collisions. The clear back-to-back nature of the signal process can be seen. Selecting events with $\Delta\phi_{\mu-X} > 170°$ rejects a lot of background events (next chapter).

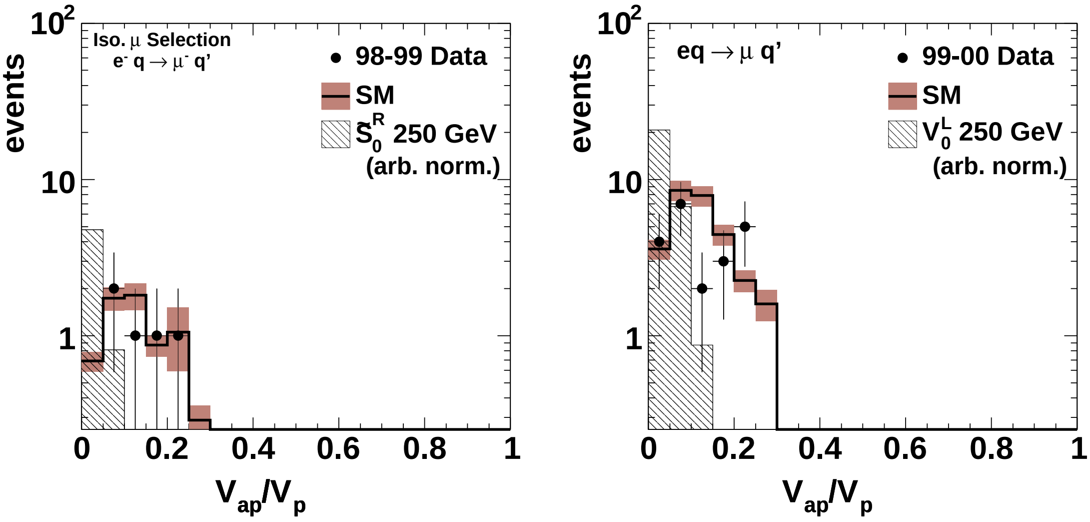

Figure 6.9: $\frac{V_{ap}}{V_p}$ distributions after the isolated muon selections for e^-p (left) and e^+p (right) collisions.

Figure 6.9 shows the $\frac{V_{ap}}{V_p}$ distributions for e^-p and e^+p collisions. The signal distribution is for LQs with a mass of 250 GeV. Figure 6.10 shows the $\frac{V_{ap}}{V_p}$ distributions for e^-p collisions where the signal distribution is for a LQ with a mass of 350 GeV. These two figures show that LQs with masses beyond the kinematic limit have broader $\frac{V_{ap}}{V_p}$ distributions than the 250 GeV LQ distribution. This is because the jets in the hadronic system are more collimated in the 250 GeV LQ case than in the 350 GeV case.

Figure 6.11 shows the D_{jet} and D_{track} distributions for e^-p and e^+p collisions. Since the signal LQ decays into a muon and a quark which are back-to-back the distance in $\eta - \phi$ between the two components is π (≈ 3.1) – a feature shown in the D_{jet}

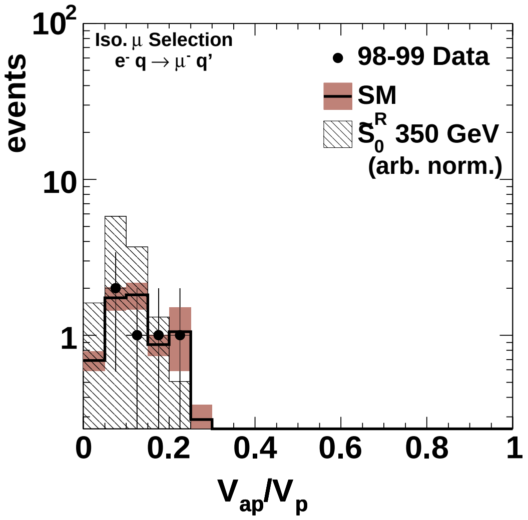

Figure 6.10: $\frac{V_{ap}}{V_p}$ distributions after the isolated muon selections for e^-p collisions. The signal distribution is for a LQ with a mass of 350 GeV.

plots. The D_{track} plots also show a peak at around π ($\approx$ 3.1) although events are more spread than the D_{jet} case.

Figure 6.12 shows the θ^{μ} and θ^{X} distributions for e^-p and e^+p collisions. The LQ signals are for a LQ with mass 250 GeV. The polar angle distributions show that signal decay products are in the forward direction unlike the case for masses beyond the kinematic limits (Figure 6.13). Their boost in the forward direction is due to the high Bjorken x values used to form the LQ from the proton (see Eq. 5.4). For LQs with masses $> \sqrt{s}$ the incoming electron interacts with the low x quarks and hence the decay products are not boosted in the forward direction and the polar angle is distributed with all angles. In addition the contribution from the u-channel (Figure 3.9) increases at these masses, which broadens the polar angle distribution.

Figure 6.14 shows the 250 GeV V_0^L LQ mass distribution reconstructed using the double angle method. The broad peak in the lower LQ mass region does not show in this figure compared to Figure 5.10 since the selections required in this chapter

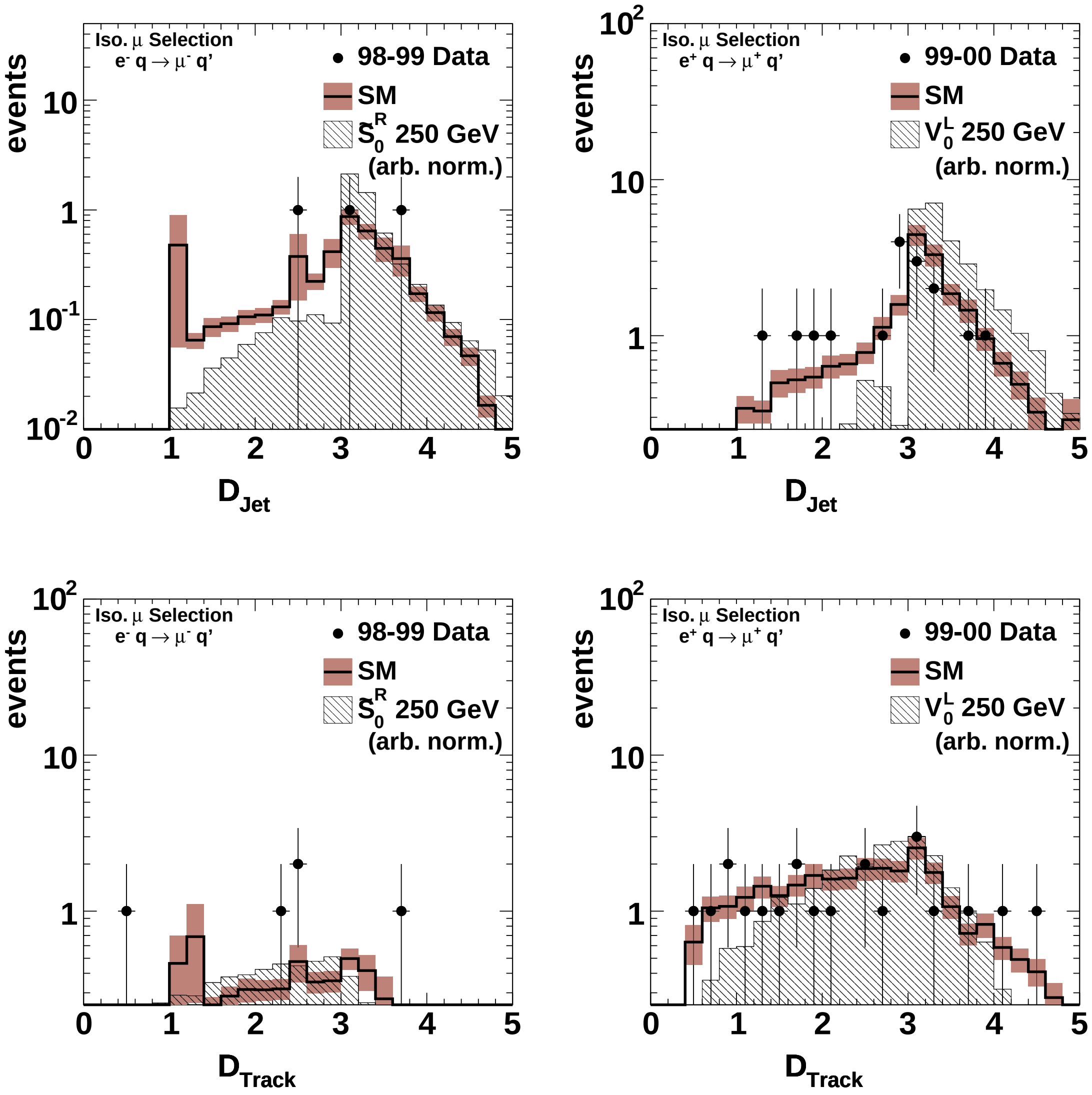

Figure 6.11: D_{jet} (top) and D_{track} (bottom) distributions after the isolated muon selections for $e^{-}p$ (left) and $e^{+}p$ (right) collisions.

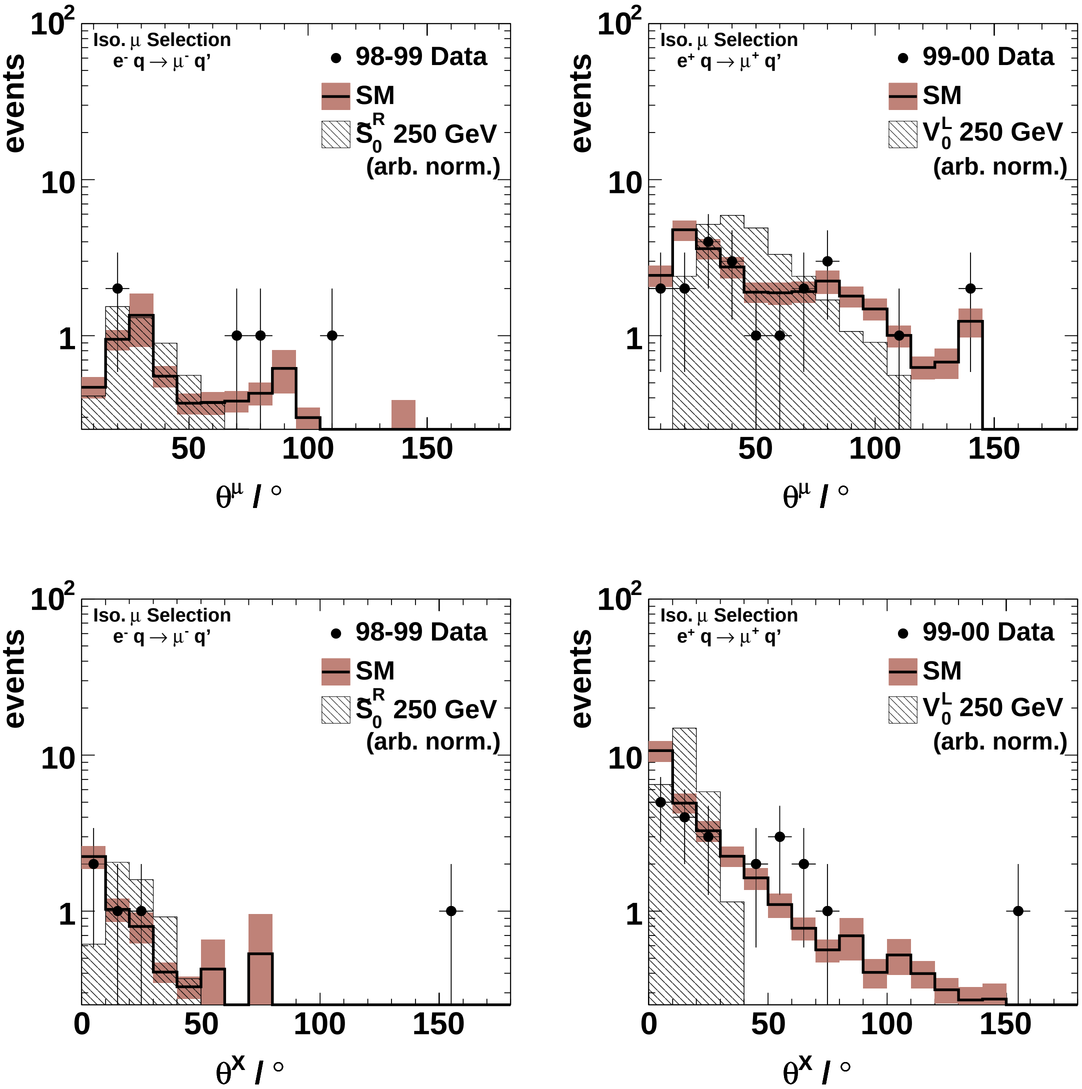

Figure 6.12: θ^μ (top) and θ^X (bottom) distributions after the isolated muon selections for e^-p (left) and e^+p (right) collisions.

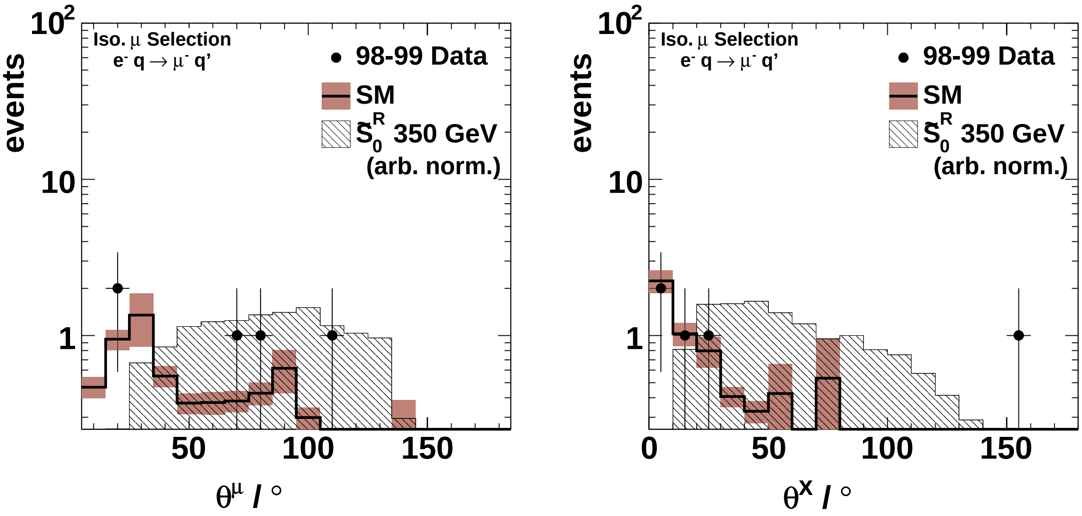

Figure 6.13: θ^{μ} (left) and θ^{X} (right) distributions after the isolated muon selections for $e^{-}p$ collisions. The LQ signals are for mass 350 GeV.

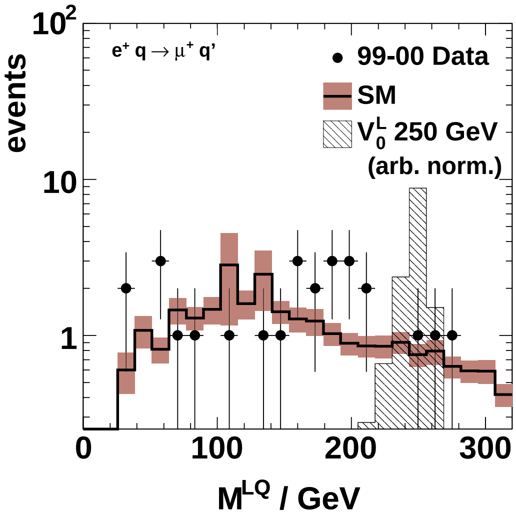

Figure 6.14: 250 GeV V_0^L LQ mass distribution reconstructed using the double angle method after the isolated muon selections.

reject these events. The mass distribution of a LQ with a mass of 350 GeV is already shown in the previous chapter (Figure 5.11) for the muon selection.

6.3 Results

The results of the isolated muon selections are summarised in Table 6.2 for both e^-p and e^+p collisions. The total number of data events contained in each selection is in agreement with the total prediction from all SM processes. The errors in the table consider the statistical and systematic uncertainties attributed to the background MCs without considering the experimental systematic uncertainties which will be described in chapter 8. The systematic uncertainties are estimated from the agreement seen in the background studies between data and MC [73] and are as follows:

- RAPGAP (NC) and GRAPE (lepton pair): 10%;
- DJANGO (CC), PYTHIA and AROMA (Photoproduction): 30%;
- EPVEC (W-decay): 15 %.

The e^-p interaction has a luminosity of $\mathcal{L} = 13.8\ pb^{-1}$ while the e^+p interaction has a luminosity of $\mathcal{L} = 66.0\ pb^{-1}$. This is why the e^-p column in the table presents fewer events. The majority of data and SM MC events are lepton pair events since the cuts applied in this selection are dedicated to identifying isolated lepton events. The contribution of the NC process in the e^-p sector is more than the e^+p sector because its cross section is incoming lepton charge dependent at high Q^2 as is seen from Figure 3.2.

SM process	events in e^-p inter.	events in e^+p inter.
NC	1.10 ± 0.54	1.48 ± 0.27
Lepton pair	4.79 ± 0.48	24.06 ± 2.42
W	0.36 ± 0.05	1.81 ± 0.27
Photoprod.	0.22 ± 0.09	0.98 ± 0.40
CC	< 0.005	< 0.005
Sum MC	6.46 ± 0.73	28.34 ± 2.49
Data	5	21

Table 6.2: Number of events for each SM MC process and data for the e^-p and e^+p interactions after applying the isolated muon cuts.

Chapter 7

$LQ \rightarrow \mu + X$ Selection

In this chapter a final set of selections which are applied to search for the required LFV process $e + q \rightarrow LQ \rightarrow \mu + X$ is introduced. After applying these cuts no data events are left in either $e^{-}p$ and $e^{+}p$ interactions with 0.23 ± 0.10 expected SM events from the $e^{-}p$ interactions and 0.74 ± 0.09 events from the $e^{+}p$ interactions. Finally, the selection efficiencies for the different LQs types including low mass LQs as well as masses far beyond the kinematic limits are outlined. The discussion of experimental systematic errors and the limits on the signal process is given in the next chapter.

7.1 Selection Criteria

Since the decay particles of LQs are back-to-back in the transverse plane, the acoplanarity of the events are required to be $> 170°$. By applying this cut a lot of background events are rejected. All other cuts applied in the previous set of selections are also applied in the final selection. The polar angle of the hadronic system is selected to be $> 7°$ to avoid poor hadronic measurements in the forward direction. The selection $P_T^{calo} > 25$ GeV removes more background events. In addition, the trigger efficiency for the hadronic system for events with these values of P_T^{calo} is high (Figure 4.2). To reduce some background events, the number of jets is required to be greater than zero. To reject NC background processes events with an isolated electrons are rejected. To reject lepton pair events, which ideally contain more than one isolated muon, the number of isolated muons is required to be exactly one. Table 7.1 summarises the cuts applied in the final level to select LFV events and their effect on the background MCs as well as the efficiency of a LQ with a mass below the kinematic limits (250 GeV) and a LQ with a mass above the kinematic limits (350 GeV). The figures in this chapter show the distributions of the kinematic variables described in the previous chapters after applying the final selection cuts. The combined SM prediction is given by the open histogram and the brown band containing the SM prediction line represents the total SM error without including the experimental systematic errors. The signal component is given by the hatched histogram.

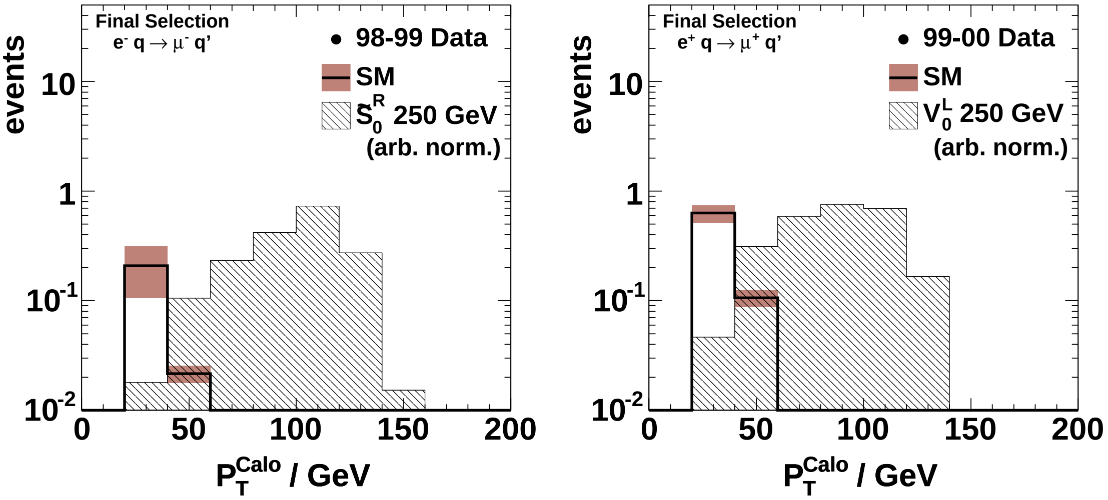

Figure 7.1: P_T^{calo} distributions after the final selections for e^-p (left) and e^+p (right) collisions.

Variables	cuts applied	Data (e^-p)	SM MC (98-99)	Data (e^+p)	SM MC (99-00)
before selection	–	1.181×10^6	1.11×10^6	1.525×10^6	5.83×10^6
non *ep* events	*see chapter 4*	2.187×10^4	7.50×10^5	9.513×10^4	3.96×10^6
P_T^μ	> 10 GeV	768	2300	3022	9540
θ^μ	$> 10°, < 140°$	663	1700	2762	7320
θ^X	$> 7°$	459	829	1460	2660
Muon Grade	*see chapter 4*	25	45.0	108	207
P_T^{calo}	> 25 GeV	0	0.78	2	3.01
D_{track}	> 0.5	0	0.73	2	2.84
D_{jet}	> 1	0	0.71	2	2.70
number of isolated electrons	$= 0$	0	0.72	0	1.65
number of isolated muons	$= 1$	0	0.43	0	1.28
number of jets	≥ 1	0	0.43	0	1.26
$\Delta\phi_{\mu-X}$	$> 170°$	0	0.23	0	0.74
$\frac{V_{ap}}{V_p}$	< 0.3	0	0.23 ± 0.10	0	0.74 ± 0.09

Variables	cuts applied	ϵ_{LQ} (Mass=250 GeV)	ϵ_{LQ} (Mass=350 GeV)
before selection	–	1.000	1.000
non *ep* events	*see chapter 4*	0.978	0.954
P_T^μ	> 10 GeV	0.964	0.897
θ^μ	$> 10°, < 140°$	0.962	0.838
θ^X	$> 7°$	0.877	0.729
Muon Grade	*see chapter 4*	0.755	0.699
P_T^{calo}	> 25 GeV	0.741	0.416
D_{track}	> 0.5	0.741	0.414
D_{jet}	> 1	0.740	0.413
number of isolated electrons	$= 0$	0.724	0.403
number of isolated muons	$= 1$	0.721	0.398
number of jets	≥ 1	0.721	0.398
$\Delta\phi_{\mu-X}$	$> 170°$	0.720	0.396
$\frac{V_{ap}}{V_p}$	< 0.3	0.720 ± 0.05	0.395 ± 0.03

Table 7.1: Cuts applied in the final level selection to select LFV events. Second level selections which were dedicated to selecting isolated muon events are included in this set. Top: Number of events after each cut for data and SM expectation for both e^-p and e^+p collisions. Bottom: Selection efficiencies (Section 7.3) after each cut for vector LQs one with a mass below the kinematic limit and one with a mass above the kinematic limit.

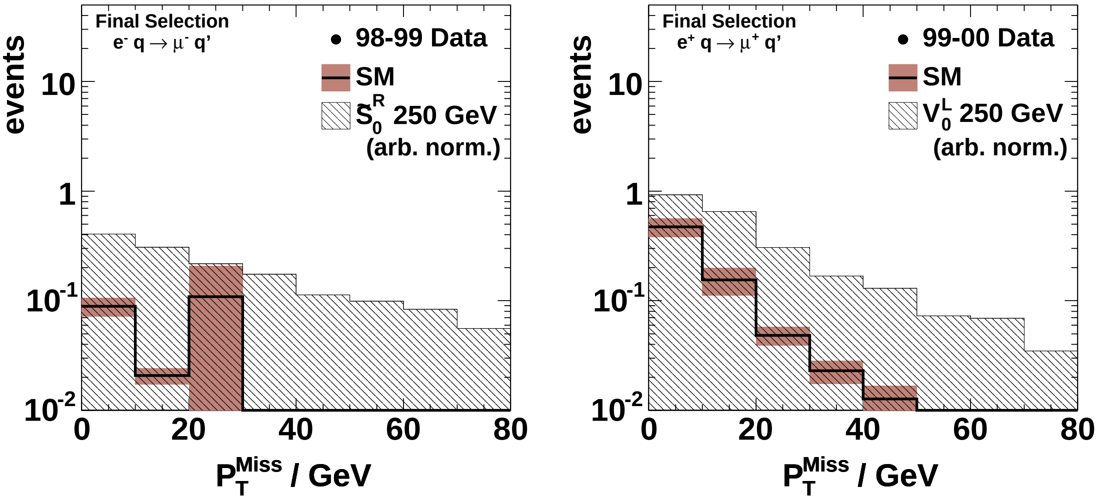

Figure 7.2: P_T^{miss} distributions after the final selections for e^-p (left) and e^+p (right) collisions.

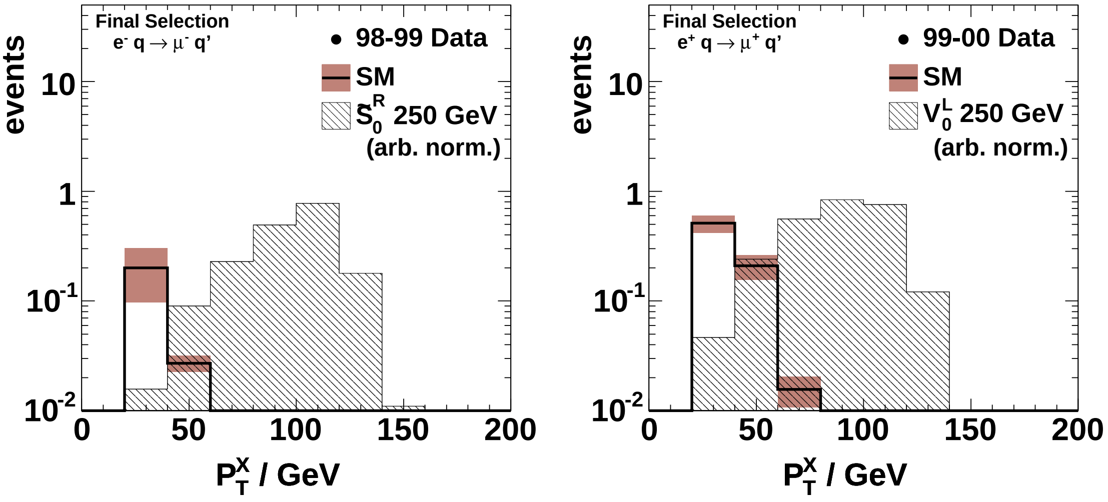

Figure 7.3: P_T^X distributions after the final selections for e^-p (left) and e^+p (right) collisions.

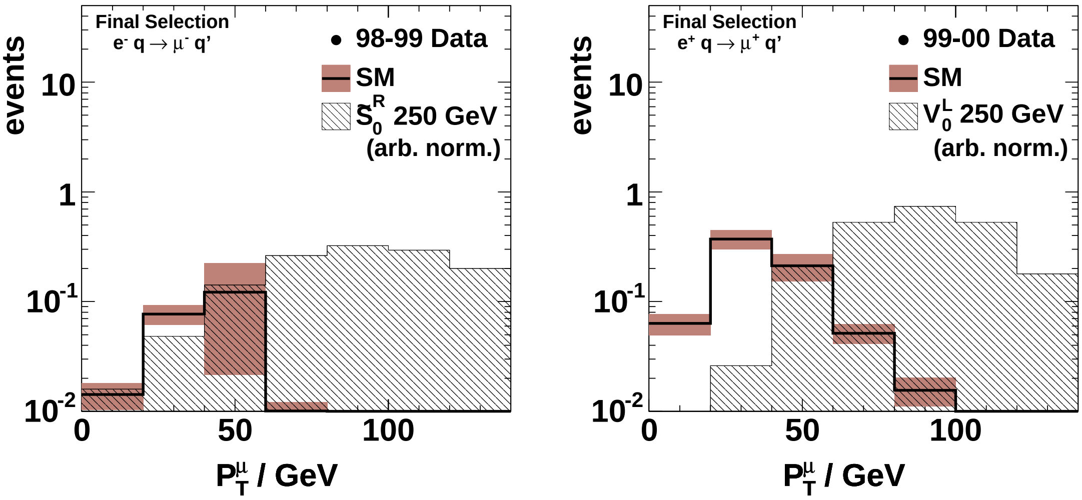

Figure 7.4: P_T^μ distributions after the final selections for e^-p (left) and e^+p (right) collisions.

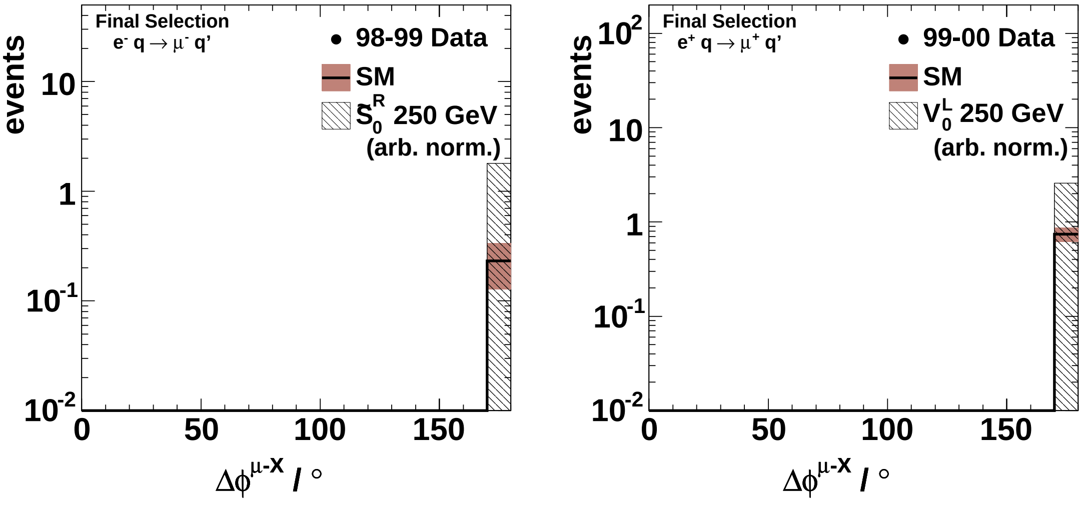

Figure 7.5: $\Delta\phi_{\mu-X}$ distributions after the final selections for e^-p (left) and e^+p (right) collisions.

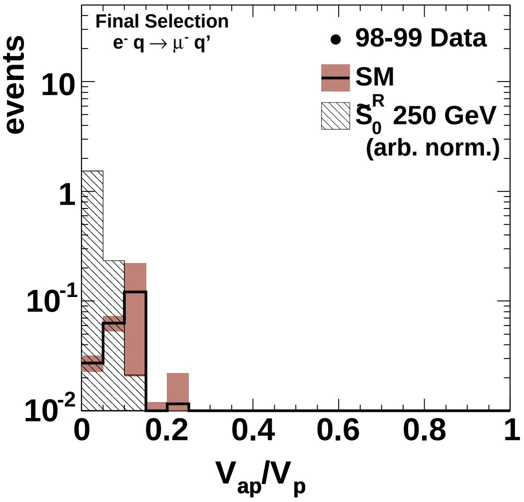

Figure 7.6: $\frac{V_{ap}}{V_p}$ distributions after the final selections for e^-p (left) and e^+p (right) collisions.

7.2 Discussion

The results of the final selections are summarised in Table 7.2 for both e^-p and e^+p collisions. The errors in the table consider the statistical and systematic uncertainties attributed to the background MCs. These errors are given in section 6.3. Due to the luminosity difference mentioned in section 6.3 between the e^-p and e^+p interactions the background processes show fewer events in the e^-p sector. The majority of SM MC events are lepton pair events which shows that the lepton pair events are more likely to mimic the signal events than other background processes when one of the two muons is lost down beam-pipe. Figure 3.12 shows an event display for lepton pair event. This will look very similar to the LFV event display in Figure 3.10 if the lowest P_T^μ is not present. Because the NC cross section depends on the charge of the incoming lepton as can be seen from Figure 3.2 it contributes more to the background in the in the e^-p sector than the e^+p sector.

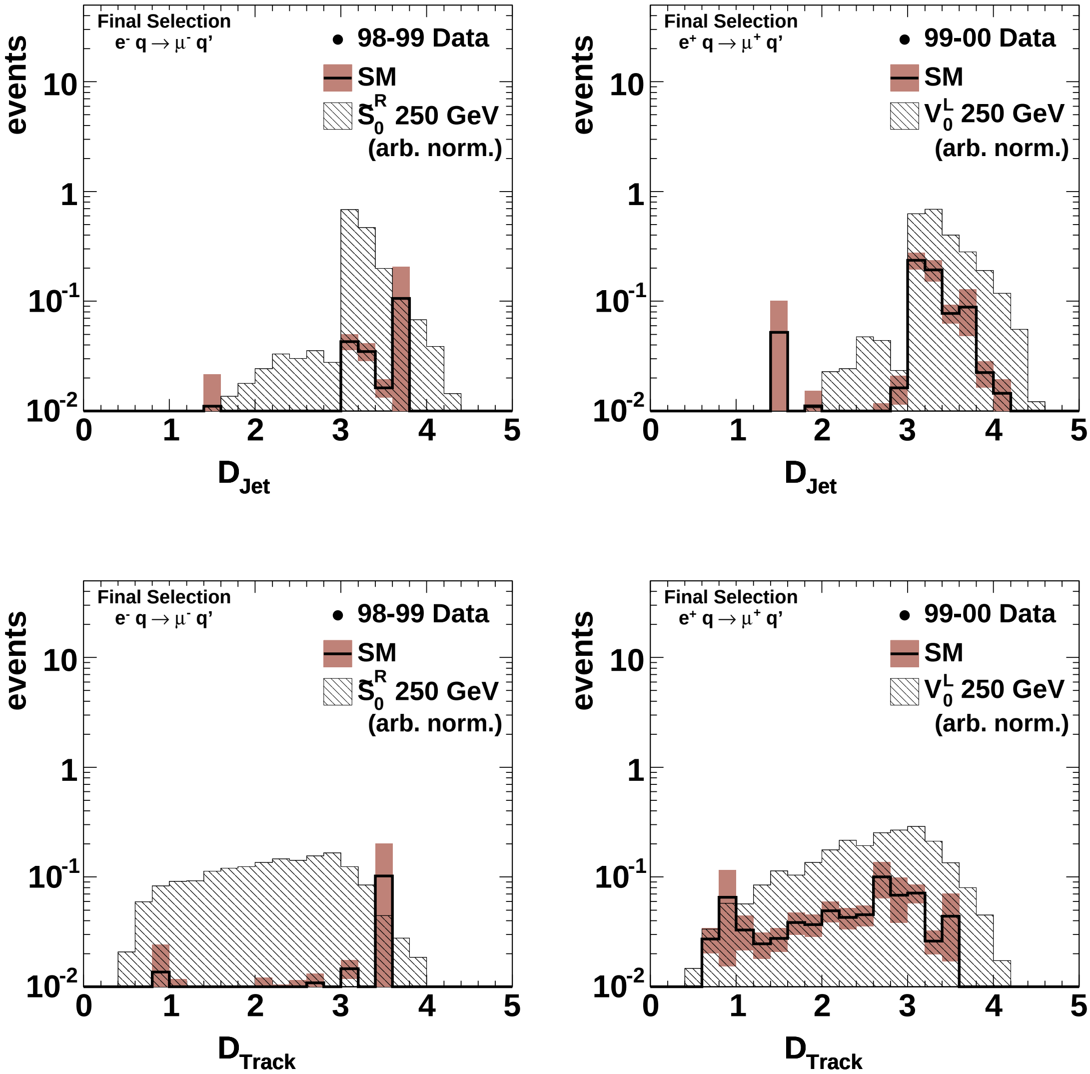

Figure 7.7: D_{jet} (top) and D_{track} (bottom) distributions after the final selections for e^-p (left) and e^+p (right) collisions.

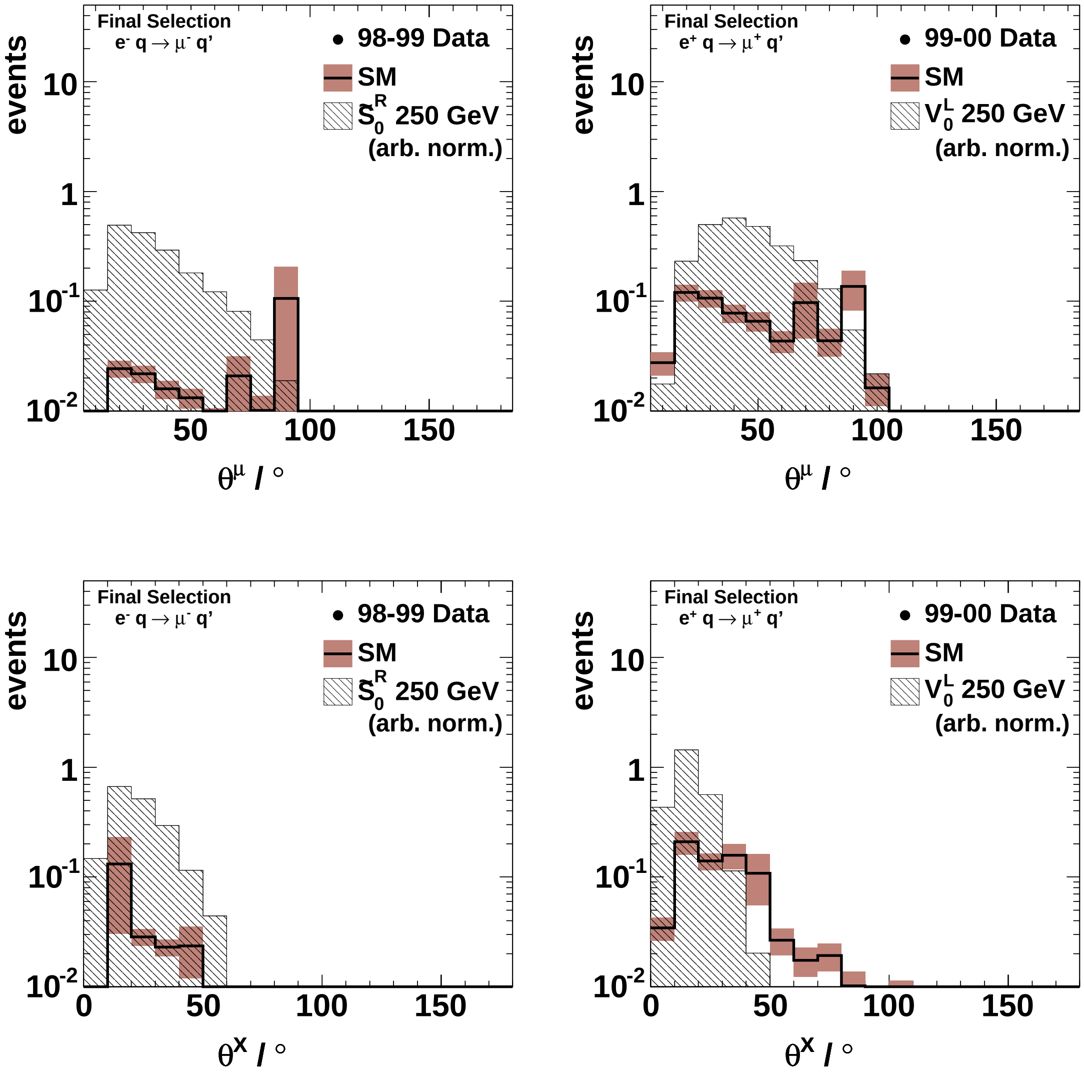

Figure 7.8: θ^μ (top) and θ^X (bottom) distributions after the final selections for e^-p (left) and e^+p (right) collisions. The signal events are for LQs with 250 GeV.

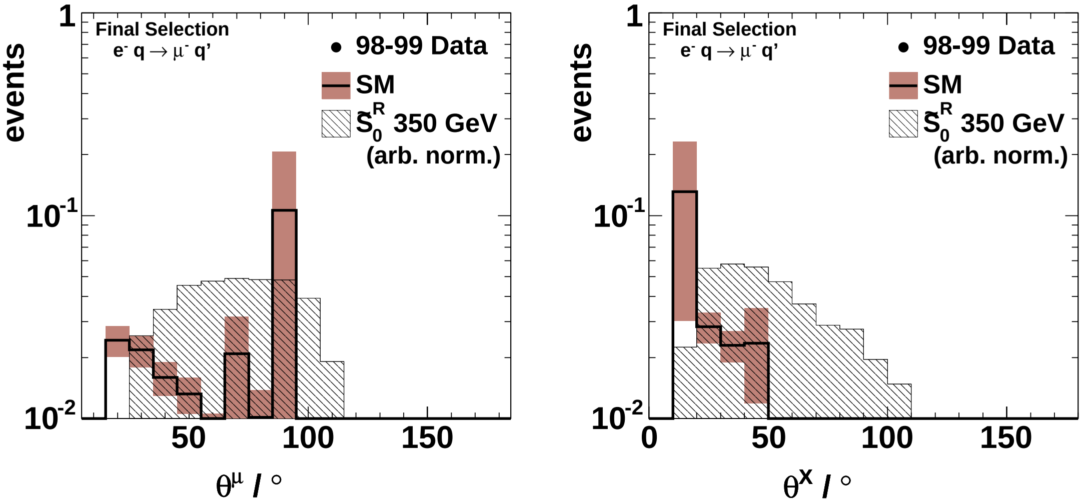

Figure 7.9: θ^{μ} (left) and θ^{X} (right) distributions after the muon selections for $e^{-}p$ collisions. The signal events are for LQs with 350 GeV.

SM process	events in $e^{-}p$ inter.	events in $e^{+}p$ inter.
NC	0.099 ± 0.100	0.099 ± 0.051
Lepton pair	0.105 ± 0.012	0.512 ± 0.057
W	0.015 ± 0.003	0.077 ± 0.013
Photoprod.	0.013 ± 0.011	0.055 ± 0.051
CC	< 0.0005	< 0.0005
Sum MC	0.232 ± 0.101	0.743 ± 0.093
Data	0	0

Table 7.2: Number of events for each SM MC process and data for the $e^{-}p$ and $e^{+}p$ interactions after applying the final selections.

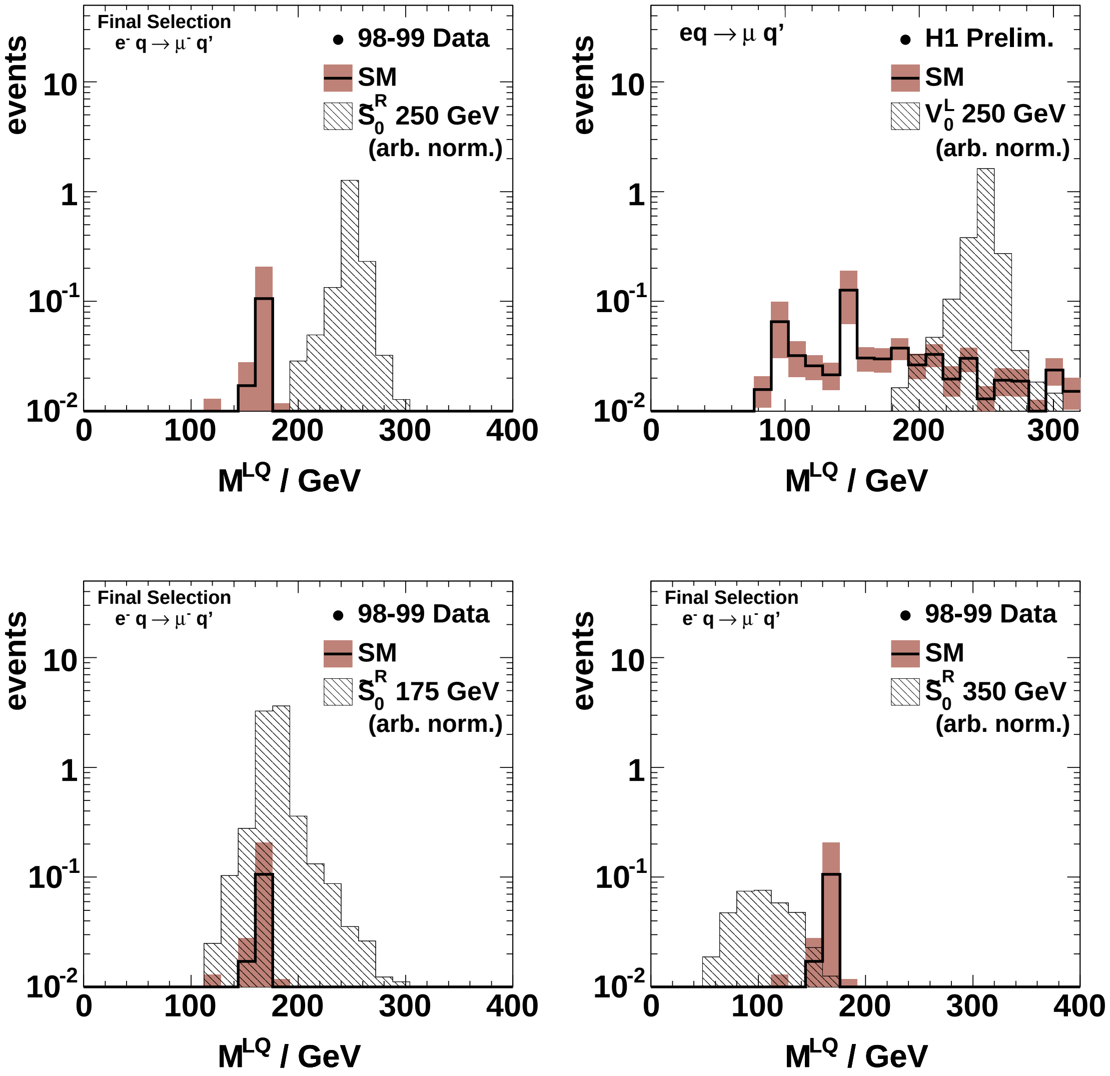

Figure 7.10: Different LQ mass distribution reconstructed using the double angle method after the final selections.

7.3 Selection Efficiency

The selection efficiency of the final event selections for a given LQ mass is defined as

$$\epsilon_{sel} = \frac{\text{Number of reconstructed events after applying cuts}}{\text{Number of generated events}}. \tag{7.1}$$

Different LQ types and masses have different efficiencies due to variations in their kinematic properties. Figure 7.11 shows the selection efficiencies for seven LQ types generated from e^-p interactions with $F = 2$ whereas Figure 7.12 shows the selection efficiencies for seven LQ types generated from e^+p interactions with $F = 0$. The error bars show the statistical errors. The fit function is a fifth order polynomial for the scalar LQs and a fourth order polynomial for the vector LQs at low masses and a hyperbolic function for high mass vector LQs. For LQs with masses far beyond the kinematic limit the selection efficiency differs for both e^-p and e^+p collisions for all 14 LQ types.

7.3.1 Low mass LQs

The selection efficiencies for low mass LQs are mass dependent as well as coupling constant dependent. Both vector and scalar LQs have low efficiency values at low masses due to their low P_T^{calo} values compared to the LQs in a mass range of 150-250 GeV. Events with low P_T^{calo} values are ruled out by the final P_T^{calo} selection. Near the kinematic limit the efficiency for selecting the vector LQs falls steeply. The fall observed for the vector LQs is due to the high P_T^{calo} and P_T^{μ} requirements and can be explained by the behaviour of the signal cross section near the kinematic limit [60]. As a LQ mass approaches the kinematic limit, events at the peak start to diminish due to the steep decrease of the parton density function at high values of x and the tail becomes more apparent as shown in Figure 5.10 and 5.11. u-channel and

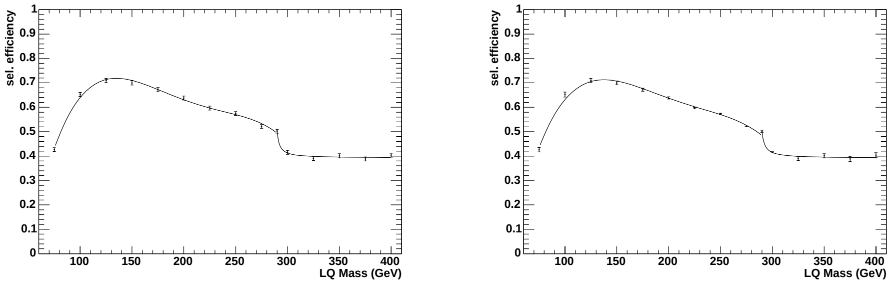

(a) $S_0^L(e^-\ u)$ **(b)** $S_0^R(e^-\ u)$

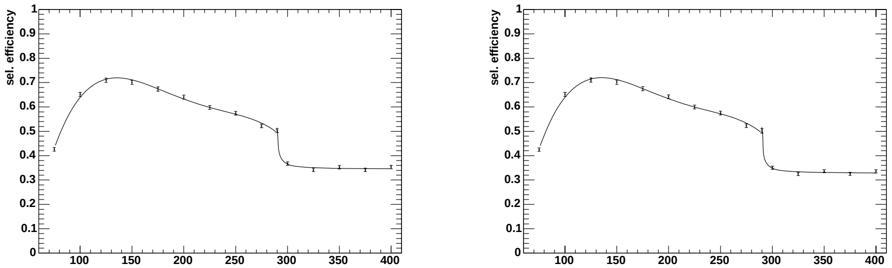

(c) $S_1^L(e^-\ u, d)$ **(d)** $\tilde{S_0}^R(e^-\ d)$

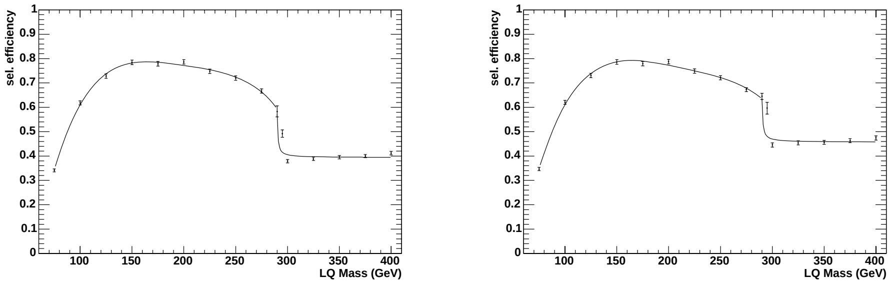

(e) $V_{1/2}^L(e^-\ d)$ **(f)** $V_{1/2}^R(e^-\ u, d)$

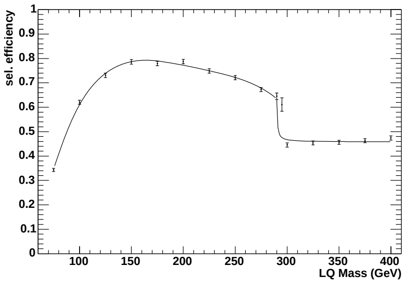

(g) $\tilde{V}_{1/2}^L(e^-\ u)$

Figure 7.11: Selection efficiencies for different LQs which may be produced in e^-p collisions after the final selections as a function of mass.

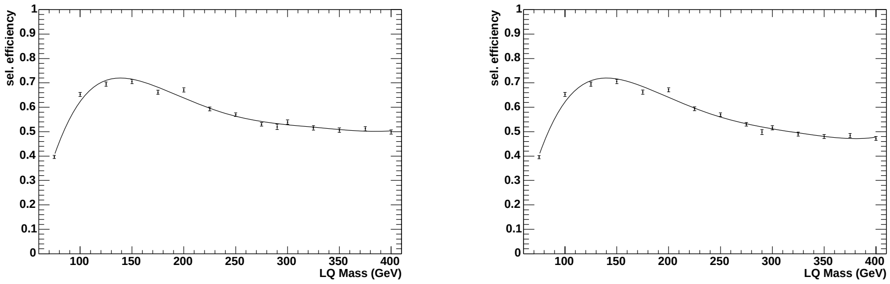

(a) $S^L_{1/2}(e^+\ u)$ **(b)** $S^R_{1/2}(e^+\ u, d)$

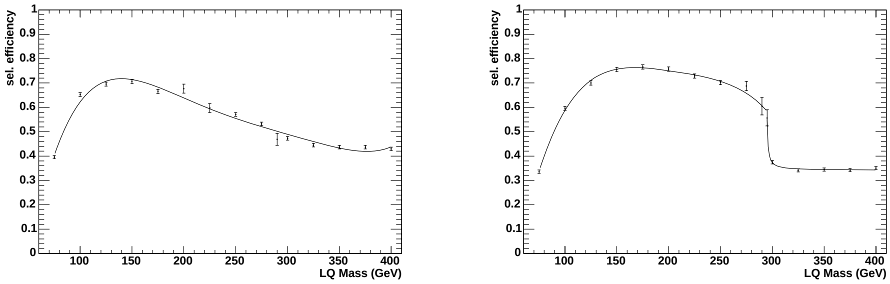

(c) $\tilde{S}^L_{1/2}(e^+\ d)$ **(d)** $V^R_0(e^+\ d)$

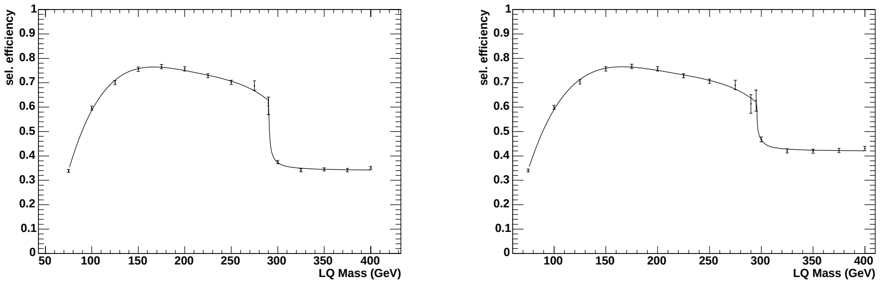

(e) $V^L_0(e^+\ d)$ **(f)** $V^L_1(e^+\ u, d)$

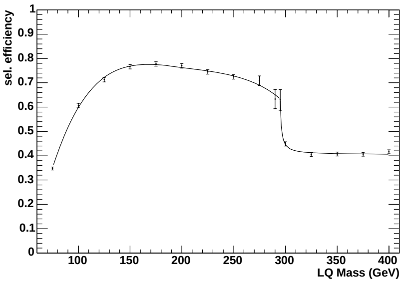

(g) $\tilde{V}^R_0(e^+\ u)$

Figure 7.12: Selection efficiencies for different LQs which may be produced in e^+p collisions after the final selections as a function of mass.

off-shell s-channel contributions to the signal cross section show a large off-resonant mass distribution at high LQ masses ($> \sqrt{s}$). The requirements for large P_T^{calo} and P_T^{μ} events reject most of these off-resonant events obtained from LQs coupling to low x-value quarks. This can be seen from

$$P_T \approx \frac{\sqrt{xs}}{2} \tag{7.2}$$

i.e. the decay products of these LQs have low P_T values resulting in lower selection efficiencies. At these masses LQs coupling to d-quarks show smaller efficiencies than those coupling to u-quarks. This is because u-quarks with higher x values are more abundant than d-quarks (Figure 3.5) and at high LQ mass values the LQs coupling to d-quarks start coupling to sea quarks which have smaller x values. On the other hand, LQs coupling to u-quarks have more chance to couple to higher x value quarks which result in events with higher P_T^{calo} values.

Both efficiency figures should in principle show similar efficiencies for LQs having the same decay branching ratios and coupling constants. The drop in the selection efficiency for the scalar LQs in the e^-p interactions at masses $> \sqrt{s}$ is due to slightly higher coupling constants used (which leads to larger decay width) than the e^+p LQs. As mentioned in chapter 5, at this mass range the efficiency is coupling constant dependent.

7.3.2 LQs with masses $\gg \sqrt{s}$

The selection efficiency of LQs with masses beyond the kinematic limit depends on their spin as well as the momentum fraction x of the quark coupling to them. Tables 7.3 and 7.4 show the selection efficiencies of LQs with different fermion numbers for e^-p and e^+p interactions respectively. In this regime all fourteen LQ types are involved in the reaction (Section 3.5.2). The tables show the three quark family contributions at the eq-vertex (q_i) and μq-vertex (q_j) where $q_1 = u$ or d, $q_2 = c$ or s

and $q_3 = b$ quarks. Scenarios involving a top quark are indicated by dashes since they are not produced at the given centre of mass energy because of their large mass. The efficiency for LQs which involve second and third generation LQs are less than the first generation because the higher generation LQs couple to low x-value quarks. From Eq. 7.2 it can be seen that the decay products of the LQs have low P_T values resulting in a lower selection efficiencies.

The efficiencies of the first generation $F = 2$ LQs in Table 7.3 are higher than the $F = 0$ LQs. This is attributed to the fact that the $F = 2$ LQs are mainly produced resonantly from the first generation quarks in the proton which have high Bjorken x values leading to higher P_T values. The second and third generation $F = 2$ LQs have lower efficiency values than the first generation LQs due to their low Bjorken x values leading to lower P_T values. The $F = 0$ LQs show high efficiencies when they are produced from the first generation quarks in the u-channel (1-1, 2-1, 3-1 scenarios). These are produced from quarks which have high Bjorken x values leading to higher P_T values. The cross section is strongly dependent on the u-channel in this case. Table 7.4 shows the efficiencies of LQs produced from the e^+p interaction. In this case the $F = 0$ ($F = 2$) LQs have efficiencies similar to the $F = 2$ ($F = 0$) LQs produced from the e^-p interactions. In the e^+p interaction the $F = 2$ LQs show high efficiencies when they are produced from the first generation quarks in the u-channel (1-1, 2-1, 3-1 scenarios) and the $F = 0$ LQs show more efficiency values when they couple to the first generation quarks in the s-channel. These quarks have high Bjorken x values leading to higher P_T values.

$q_i q_j$	$S^L_{1/2}$	$S^R_{1/2}$	$\tilde{S}^L_{1/2}$	V^L_0	V^R_0	$\tilde{V}^R_0$	V^L_1
	$e^-\bar{u}$	$e^-(\bar{u}+\bar{d})$	$e^-\bar{d}$	$e^-\bar{d}$	$e^-\bar{d}$	$e^-\bar{u}$	$e^-(\sqrt{2}\bar{u}+\bar{d})$
1 1	0.39	0.35	0.31	0.41	0.41	0.47	0.46
1 2	0.21	0.22	0.23	0.21	0.21	0.20	0.20
1 3	—	0.23	0.24	0.20	0.19	—	0.20
2 1	0.41	0.36	0.30	0.40	0.41	0.48	0.47
2 2	0.22	0.20	0.19	0.19	0.19	0.21	0.20
2 3	—	0.21	0.20	0.15	0.15	—	0.19
3 1	—	0.41	0.32	0.41	0.41	—	0.45
3 2	—	0.18	0.18	0.19	0.19	—	0.17
3 3	—	0.17	0.17	0.14	0.14	—	0.14

$q_i q_j$	S^L_0	S^R_0	$\tilde{S}^R_0$	S^L_1	$V^L_{1/2}$	$V^R_{1/2}$	$\tilde{V}^L_{1/2}$
	e^-u	e^-u	e^-d	$e^-(u+\sqrt{2}d)$	e^-d	$e^-(u+d)$	e^-u
1 1	0.47	0.47	0.36	0.40	0.32	0.36	0.39
1 2	0.48	0.48	0.36	0.40	0.31	0.37	0.41
1 3	—	—	0.37	0.41	0.33	0.41	—
2 1	0.21	0.21	0.20	0.20	0.22	0.22	0.21
2 2	0.21	0.22	0.19	0.19	0.19	0.20	0.21
2 3	—	—	0.20	0.20	0.15	0.17	—
3 1	—	—	0.18	0.18	0.22	0.21	—
3 2	—	—	0.16	0.15	0.19	0.16	—
3 3	—	—	0.17	0.17	0.14	0.14	—

Table 7.3: Selection efficiencies of $F = 0$ (top) and $F = 2$ (bottom) LQs coupling to the first, second and third quark generations for e^-p interactions. The dashes represent scenarios involving a top quark.

$q_i q_j$	$S^L_{1/2}$	$S^R_{1/2}$	$\tilde{S}^L_{1/2}$	V^L_0	V^R_0	$\tilde{V}^R_0$	V^L_1
	e^+u	$e^+(u+d)$	e^+d	e^+d	e^+d	e^+u	$e^+(\sqrt{2}u+d)$
1 1	0.47	0.43	0.36	0.32	0.32	0.39	0.38
1 2	0.48	0.44	0.36	0.31	0.31	0.41	0.39
1 3	—	0.45	0.37	0.33	0.33	—	0.45
2 1	0.21	0.20	0.20	0.22	0.22	0.21	0.21
2 2	0.22	0.20	0.19	0.19	0.19	0.21	0.20
2 3	—	0.21	0.20	0.15	0.15	—	0.19
3 1	—	0.19	0.18	0.20	0.22	—	0.21
3 2	—	0.18	0.16	0.19	0.19	—	0.20
3 3	—	0.17	0.17	0.14	0.14	—	0.14

$q_i q_j$	S^L_0	S^R_0	$\tilde{S}^R_0$	S^L_1	$V^L_{1/2}$	$V^R_{1/2}$	$\tilde{V}^L_{1/2}$
	$e^+\bar{u}$	$e^+\bar{u}$	$e^+\bar{d}$	$e^+(\bar{u}+\sqrt{2}\bar{d})$	$e^+\bar{d}$	$e^+(\bar{u}+\bar{d})$	$e^+\bar{u}$
1 1	0.39	0.39	0.31	0.33	0.41	0.45	0.47
1 2	0.21	0.21	0.23	0.22	0.21	0.21	0.20
1 3	—	—	0.24	0.23	0.19	0.19	—
2 1	0.41	0.41	0.30	0.33	0.41	0.45	0.48
2 2	0.22	0.22	0.19	0.19	0.19	0.20	0.21
2 3	—	—	0.20	0.20	0.15	0.17	—
3 1	—	—	0.32	0.36	0.41	0.46	—
3 2	—	—	0.16	0.17	0.19	0.19	—
3 3	—	—	0.17	0.17	0.14	0.14	—

Table 7.4: Selection efficiencies of $F = 0$ (top) and $F = 2$ (bottom) LQs coupling to the first second and third quark generations for e^+p interactions. The dashes indicate scenarios involving a top quark.

Chapter 8

Interpretation

The final results are discussed in this chapter. The full systematic uncertainties are introduced and the limits on the LQ signal coupling constants and branching ratios are set for low mass LQs. Also, limits on the four fermion interaction term ,$\frac{\lambda_{eq_i}\lambda_{\mu q_i}}{M_{LQ}^2}$, for different LQ scenarios with masses far beyond the centre of mass region are set.

8.1 Systematic Uncertainties

The systematic uncertainties on the background processes are described in section 6.3. The experimental uncertainties on the signal and background processes are determined by varying the experimental quantities by ±1 standard deviation and recalculating the cross section.

The systematic uncertainty on the muon energy scale is 5%. This is obtained from the P_T balance of a data sample of muon pair events [73]. Using the same data sample the muon identification efficiency is assigned an uncertainty of 6% and the uncertainty on the track finding efficiency is 3% [39]. The uncertainties on the muon polar and azimuthal angles are 3 and 1 mrad respectively. The muon trigger inefficiency is taken to be 6% [39].

Uncertainties on the hadronic system are obtained from the standard NC sample [81]. The uncertainty on the hadronic energy scale is 2% and the hadronic polar and azimuthal angle uncertainties are 10 mrad [82]. The uncertainty on the luminosity measurement of the data analysed is taken to be 1.5%. These uncertainties are combined in quadrature with the MC errors, the experimental systematic uncertainties described above and the statistical errors. After taking all these uncertainties into account the final selection results for different MC processes are shown in Table 8.1.

SM process	events in e^-p inter.	events in e^+p inter.
NC	0.099 ± 0.100	0.099 ± 0.052
Lepton pair	0.105 ± 0.058	0.512 ± 0.244
W	0.015 ± 0.006	0.077 ± 0.025
Photoprod.	0.013 ± 0.014	0.055 ± 0.060
CC	< 0.0005	< 0.0005
Sum MC	0.232 ± 0.117	0.743 ± 0.257
Data	0	0

Table 8.1: Number of events for each MC process and data for the e^-p and e^+p interactions after applying the final selections. The errors include all uncertainties described in the text.

The following uncertainties are related to the modelling of the LQ signal and the parametrisation of the parton density functions and add more uncertainty to the LQ cross section:

- The theoretical uncertainty on the signal cross section due to uncertainties in the parton densities varies from 7% for $e^+u \rightarrow$ LQ at low LQ masses up to 50% at high LQ masses for $e^+d \rightarrow$ LQ.
- Choosing either Q^2 or the square of the transverse momentum of the final

state muon instead of the centre of mass energy of the hard subprocess, $\sqrt{sx}$, as the hard scale at which the parton distributions are estimated, yields an uncertainty of 7% on the signal process.

8.2 Limit Procedure

A measurement of any true unknown quantity X may lead a result x. When there is no evidence for a signal above the background x is turned into limit on X. The background contribution as well as its uncertainty have to be included in the limit calculation. Different limit approaches are used in different analyses. In this analysis the *modified frequentist* [83] approach used at LEP for SM Higgs and MSSM Higgs searches [84] is used.

8.2.1 Confidence Level

In search experiments the probability distribution of observing x if X is expected is $p(x, X)$. For fixed values of α (where $0 < \alpha < 1$) and X, two boundaries for x can be observed: $x_-(X, \alpha)$ and $x_+(X, \alpha)$ such that the probability for x becomes:

$$p(x_- < x < x_+) = 1 - \alpha = \int_{x_-}^{x_+} p(x, X)\ dx.$$

From any measured value of x the *confidence level* (CL) interval of X for a given α has the limits $X_-(x_+(X, \alpha), x)$ and $X_+(x_-(X, \alpha), x)$. In other words the true value of X is sandwiched between two limits with the probability $1 - \alpha$. However, in a search experiment, only the upper limit is taken and consequently $X_- = 0$. Hence, the probability of getting the limits $(0, X_+)$ in a set of identical search experiments is $1 - \alpha$.

In research experiments the upper limits can be found from a Poisson distribution.

This is done by requiring the mean expected number N to lead to n observed events with α probability. If n events are observed and the number of expected events N is unknown, the 95% CL upper limit on N is N_+ such that:

$$\sum_{r=0}^{n} p(r; N_+) = 0.05.$$

In other words the probability of getting a result n smaller than N_+ is 5% or the true value of N_+ is not larger at 95% CL [85].

8.2.2 The Modified Frequentist Approach

From the outcome of searches which look for new particles signal, and background are indistinguishable. If more than one channel exists in the search the *test statistic,* Y is defined in order to distinguish between signal-like outcomes and background-like outcomes using the *likelihood ratio* method [86]. This is defined as the ratio of the probabilities for observing a signal + background $(s+b)$ hypothesis outcome to a background-only hypothesis outcome. The likelihood ratio of a selection channel i is given by

$$Y_i = \frac{e^{(s_i+b_i)}(s_i+b_i)^{d_i}}{d_i!} / \frac{e^{b_i} b_i^{d_i}}{d_i!} \tag{8.1}$$

where b_i is the estimated background, and d_i is the number of data candidate events. The expected number of signal events is $s_i = \epsilon N$ where N is the total number of signal events and ϵ is the selection efficiency.

For ℓ channels the likelihood ratio is given by:

$$Y = \prod_{i=1}^{\ell} Y_i \tag{8.2}$$

The 95% CL is the probability that the test statistic, $Y(d_i')$, would be less than or equal to those observed in the data given by the Poisson probabilities:

$$CL_{s+b} = P_{s+b}(Y \leq Y_{obs}) = \sum_{Y(d_i') \leq Y(d_i)} \prod_{i=1}^{\ell} \frac{e^{(s_i+b_i)}(s_i+b_i)^{d_i'}}{d_i'!}, \tag{8.3}$$

which is the CL for both signal and background outcomes. The CL for the background alone is given by

$$CL_b = P_b(Y \leq Y_{obs}) \tag{8.4}$$

The term in the bracket shows that the probability that background processes would give less than or equal to the number of data observed. From the above equations the CL is used to set exclusion limits and is evaluated by

$$CL_s = CL_{s+b}/CL_b. \tag{8.5}$$

Systematic uncertainties on signal and background are taken into account by averaging over possible values of the signal and background assuming a Gaussian distribution [83]. In this analysis only one channel (either e^-p interactions or e^+p interactions) contributes to the signal for low LQ masses. However, for masses far beyond the centre of mass energy both e^-p and e^+p LQs are considered and hence the two channels are combined in the limit calculations. All fourteen LQ types are involved in either collision type unlike the low mass LQ case where the resonant signal is required.

8.3 Limit Results

8.3.1 Low mass LQs

The number of data events, background events and the selection efficiency are used to calculate an upper limit on the signal cross section at 95% CL. These limits are converted into limits on the coupling constants, $\lambda_{\mu q}$, using the full cross section equation (Eq. 3.28 and 3.30). The obtained limits are shown in Figure 8.1 for scalar and vector LQs for the e^-p interaction. Figure 8.2 shows limits on the coupling constants, $\lambda_{\mu q}$, for scalar and vector LQs for the e^+p interaction. The decay of the LQ to electrons will be always finite since LQs are produced from them. The limits shown are for a LFV of a branching ratio of $BR_{\mathrm{LQ}\to\mu q} = 0.5$. The e^-p interaction limit is lower than the e^+p interaction limit because of its lower luminosity. H1 limits are compared to ZEUS limits [87] for one scalar and one vector LQ in each figure. The ZEUS limits add an additional 47 pb^{-1} with a total integrated luminosity of $\mathcal{L} = 113$ pb^{-1} taking all e^+p interaction data from 1994-2000. Limits at 95% CL from the ZEUS experiment were converted to limits on $\sqrt{BR} \times \lambda$ using the NWA (Eq. 3.31).

The limit calculation is extended to different branching ratios fixing λ_{eq} at the electromagnetic coupling strength of 0.3. The branching ratio is obtained from

$$BR = \frac{\lambda_\mu^2}{\lambda_e^2 + \lambda_\mu^2} \tag{8.6}$$

where λ_e is the coupling constant of the incoming electron to the LQ and λ_μ is the coupling constant of the outgoing muon to the LQ. Figure 8.3 shows limits on $BR_{\mathrm{LQ}\to\mu q}$ with different LQs types for both e^-p and e^+p collisions.

Searches for LFV in other experiments

Tevatron and HERA limits are complementary since the cross section at the $p\bar{p}$ Tevatron colliders does not depend on the Yukawa coupling. In addition, LQs are assumed to couple only with one lepton generation. The CDF and DØ collaborations exclude scalar LQs coupling exclusively to μq with masses up to 202 GeV [88] and 200 GeV [89], respectively. Searches for LFV interactions not mediated by LQs were performed by the LEP experiments, looking for $e\mu$ and $\mu\tau$ production in e^+e^- annihilation at the Z^0 peak; the OPAL collaboration extended the search to higher energy using LEP2 data [90]. Also in this case no significant deviation from the SM expectation was found.

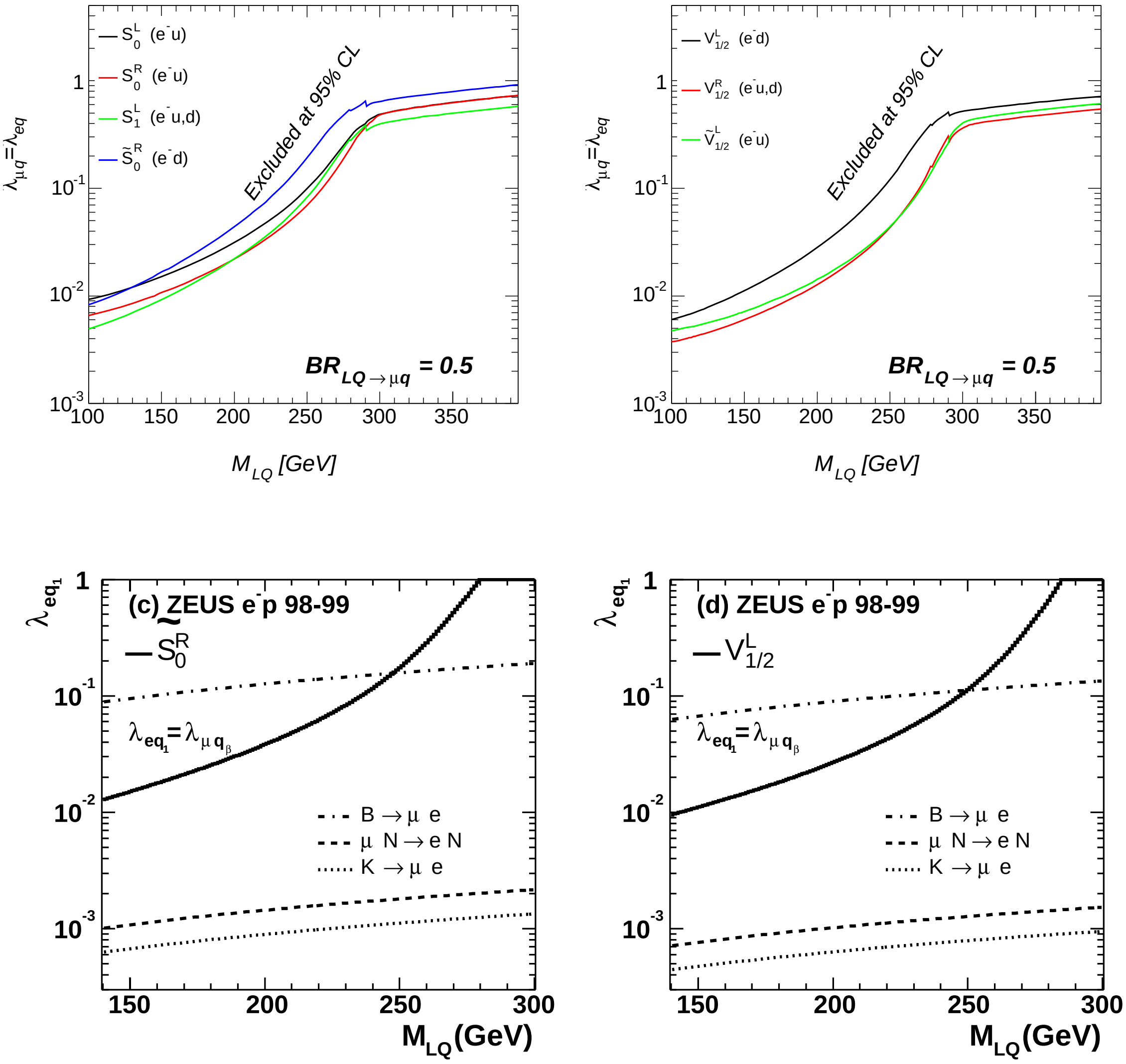

Figure 8.1: Exclusion limits from H1 (top) on λ_μ in terms of mass for scalar (right) and vector (left) LQs in e^-p interactions compared to ZEUS (bottom) taken from [87] for $\tilde{S}_0^R$ (left) and $V_{1/2}^L$ (right) LQs. The brackets show the quark(s) in the incoming proton contributing to the LQ formation. The ZEUS limits are for LQs between 140 and 300 GeV. H1 and ZEUS limits are very comparable for low mass LQs.

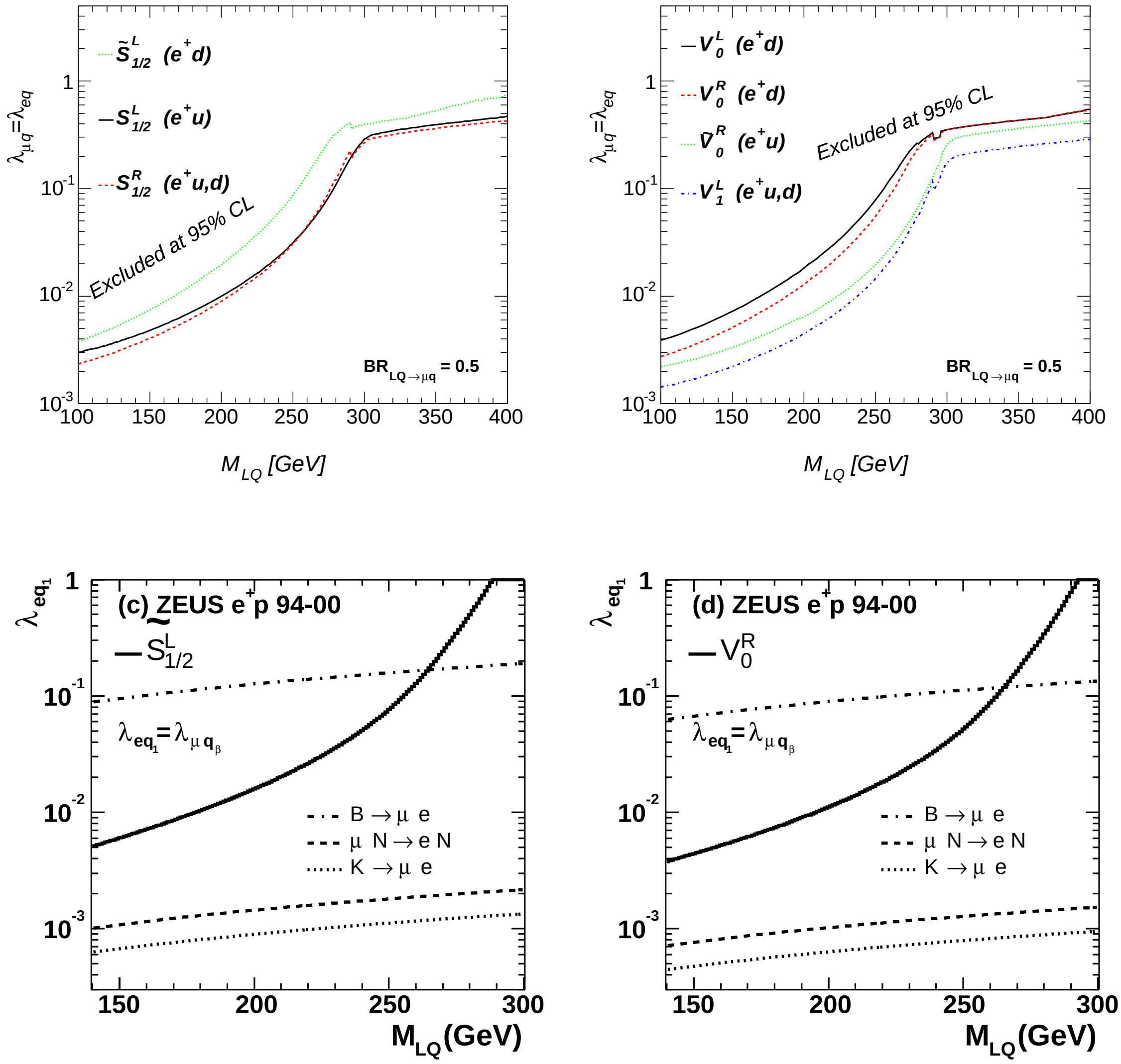

Figure 8.2: Exclusion limits from H1 (top) on λ_μ in terms of mass for scalar (left) and vector (right) LQs in e^+p interactions compared to ZEUS (bottom) taken from [87] for $\tilde{S}^L_{1/2}$ (left) and V^R_0 (right) LQs for 1994-2000 data with $\mathcal{L} = 113$ pb^{-1}. The brackets show the quark(s) in the incoming proton contributing to the LQ formation. The ZEUS limits are for LQs between 140 and 300 GeV. H1 and ZEUS limits are very comparable for low mass LQs.

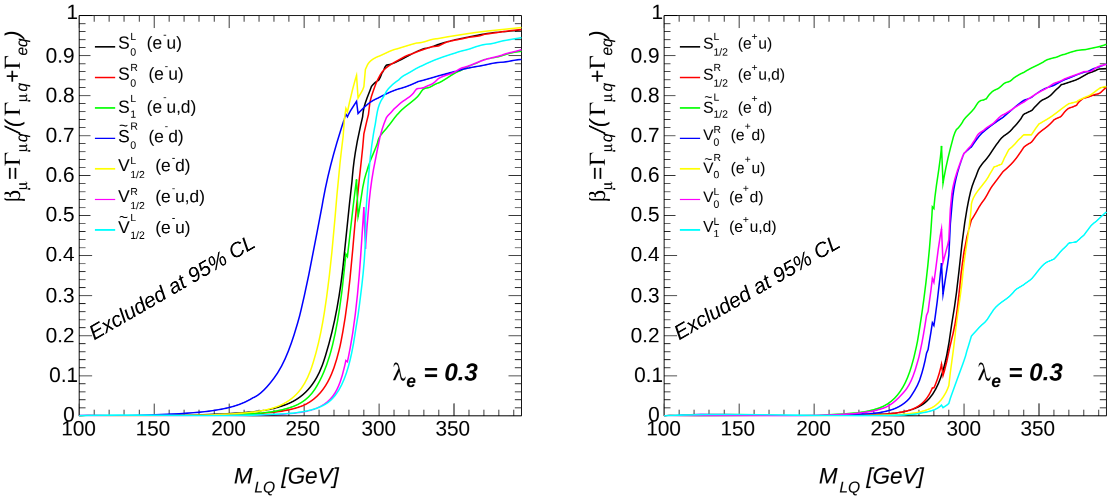

Figure 8.3: Branching ratio limit of all LQs involved in the e^-p (left) and e^+p interactions (right) at 95% CL in terms of mass for LQ $\rightarrow \mu q$ with a fixed coupling to first generation leptons at electromagnetic coupling constant strength, $\lambda_{eq} = 0.3$.

8.3.2 LQs with masses $\gg \sqrt{s}$

As was already discussed in chapter 3 the high mass approximation (HMA) is used to calculate the cross section for LQs with mass $\gg \sqrt{s}$. From Eq. 3.32 the cross section can be computed. q_i and q_j label the densities of the quarks that couple to the electron and the higher generation leptons, respectively (Figure 3.9). All information needed is contained in the term in the bracket in the equations, namely $\frac{\lambda_{eq_i}\lambda_{\mu q_i}}{M_{LQ}^2}$. Therefore, limits are found on this quantity. Table 8.2 and 8.3 list the upper limits on this quantity at 95% CL for all LQs coupling to the first, second and third generations quarks. Scenarios involving a top quark are indicated by '$*$' since it cannot be produced within the current centre of mass energy. Both e^-p and e^+p interactions are combined and hence LQs with $F = 0$ (Table 8.2) and $F = 2$ (Table 8.3) are listed. In order to include all these interactions 126 different scenarios were taken into account for these limit calculations. As can be seen in these tables the limits on first generation LQs are more stringent than the second generation. This can be explained by the higher selection efficiency of the first generation compared to the second generation. These limits are compared to the ZEUS [87] and low energy experiments limits [91–94]. ZEUS limits are more stringent than the H1 limits because they include the 1994-1997 data which adds 47.7 pb^{-1} more luminosity.

$e \to \mu$ 98-00 $e^{\pm}p$ $F = 0$

q_iq_j	$S^L_{1/2}$ $e^-\bar{u}$ e^+u	$S^R_{1/2}$ $e^-(\bar{u}+\bar{d})$ $e^+(u+d)$	$\tilde{S}^L_{1/2}$ $e^-\bar{d}$ e^+d	V^L_0 $e^-\bar{d}$ e^+d	V^R_0 $e^-\bar{d}$ e^+d	$\tilde{V}^R_0$ $e^-\bar{u}$ e^+u	V^L_1 $e^-(\sqrt{2}\bar{u}+\bar{d})$ $e^+(\sqrt{2}u+d)$
1 1	$\mu N \to eN$ 7.6×10^{-7} 0.011 **H1:0.015**	$\mu N \to eN$ 2.6×10^{-7} 0.009 **H1:0.013**	$\mu N \to eN$ 7.6×10^{-7} 0.016 **H1:0.024**	$\mu N \to eN$ 2.6×10^{-7} 0.010 **H1:0.014**	$\mu N \to eN$ 2.6×10^{-7} 0.010 **H1:0.014**	$\mu N \to eN$ 2.6×10^{-7} 0.008 **H1:0.010**	$\mu N \to eN$ 1.1×10^{-7} 0.004 **H1:0.005**
1 2	$D \to \mu\bar{e}$ 0.04 0.012 **H1:0.016**	$K \to \mu\bar{e}$ 2.7×10^{-7} 0.010 **H1:0.013**	$K \to \mu\bar{e}$ 2.7×10^{-7} 0.017 **H1:0.025**	$K \to \mu\bar{e}$ 1.3×10^{-7} 0.012 **H1:0.019**	$K \to \mu\bar{e}$ 1.3×10^{-7} 0.012 **H1:0.019**	$D \to \mu\bar{e}$ 0.02 0.010 **H1:0.014**	$K \to \mu\bar{e}$ 1.3×10^{-7} 0.005 **H1:0.007**
1 3	*	$B \to \mu\bar{e}$ 0.008 0.018 **H1:0.023**	$B \to \mu\bar{e}$ 0.008 0.018 **H1:0.025**	V_{ub} 0.002 0.015 **H1:0.022**	$B \to \mu\bar{e}$ 0.004 0.015 **H1:0.022**	*	V_{ub} 0.002 0.015 **H1:0.019**
2 1	$D \to \mu\bar{e}$ 0.04 0.036 **H1:0.047**	$K \to \mu\bar{e}$ 2.7×10^{-7} 0.024 **H1:0.035**	$K \to \mu\bar{e}$ 2.7×10^{-7} 0.032 **H1:0.051**	$K \to \mu\bar{e}$ 1.3×10^{-7} 0.013 **H1:0.019**	$K \to \mu\bar{e}$ 1.3×10^{-7} 0.013 **H1:0.019**	$D \to \mu\bar{e}$ 0.02 0.013 **H1:0.014**	$K \to \mu\bar{e}$ 1.3×10^{-7} 0.006 **H1:0.007**
2 2	$\mu \to 3e$ 5×10^{-5} 0.058 **H1:0.084**	$\mu \to 3e$ 7.3×10^{-5} 0.031 **H1:0.051**	$\mu \to 3e$ 1.6×10^{-4} 0.038 **H1:0.064**	$\mu \to 3e$ 8×10^{-5} 0.019 **H1:0.032**	$\mu \to 3e$ 8×10^{-5} 0.019 **H1:0.032**	$\mu \to 3e$ 2.5×10^{-5} 0.029 **H1:0.044**	$\mu \to 3e$ 1.5×10^{-5} 0.012 **H1:0.018**
2 3	*	$B \to \bar{\mu}eK$ 0.006 0.043 **H1:0.068**	$B \to \bar{\mu}eK$ 0.006 0.043 **H1:0.069**	$B \to \bar{\mu}eK$ 0.003 0.029 **H1:0.053**	$B \to \bar{\mu}eK$ 0.003 0.029 **H1:0.053**	*	$B \to \bar{\mu}eK$ 0.003 0.029 **H1:0.047**
3 1	*	$B \to \mu\bar{e}$ 0.008 0.044 **H1:0.060**	$B \to \mu\bar{e}$ 0.008 0.044 **H1:0.065**	V_{ub} 0.002 0.015 **H1:0.019**	$B \to \mu\bar{e}$ 0.004 0.015 **H1:0.019**	*	V_{ub} 0.002 0.015 **H1:0.019**
3 2	*	$B \to \bar{\mu}eK$ 0.006 0.058 **H1:0.095**	$B \to \bar{\mu}eK$ 0.006 0.058 **H1:0.099**	$B \to \bar{\mu}eK$ 0.003 0.022 **H1:0.035**	$B \to \bar{\mu}eK$ 0.003 0.022 **H1:0.035**	*	$B \to \bar{\mu}eK$ 0.003 0.022 **H1:0.035**
3 3	*	$\mu \to ee\bar{e}$ 7.3×10^{-5} 0.077 **H1:0.117**	$\mu \to ee\bar{e}$ 1.6×10^{-4} 0.077 **H1:0.117**	$\mu \to ee\bar{e}$ 8×10^{-5} 0.039 **H1:0.067**	$\mu \to ee\bar{e}$ 8×10^{-5} 0.039 **H1:0.067**	*	$\mu \to ee\bar{e}$ 1.5×10^{-5} 0.039 **H1:0.067**

Table 8.2: First row: Most stringent limits from low energy experiments; Second row: ZEUS limits for 1994-2000 ($e^{\pm}$) interactions; Third row: H1 limits for 1998-2000 ($e^{\pm}$) interactions giving a total integrated luminosity of 80.8 pb^{-1} for $F = 0$ type LQs. The ZEUS limits are more stringent because they include the 94-97 data as well giving a total integrated luminosity of 129.9 pb^{-1}. The cases marked with '$*$' refers to scenarios involving a top quark.

$e \to \mu$ 98-00 $e^{\pm}p$ $F = 2$

$q_i q_j$	S_0^L $e^- u$ $e^+ \bar{u}$	S_0^R $e^- u$ $e^+ \bar{u}$	$\tilde{S}_0^R$ $e^- d$ $e^+ \bar{d}$	S_1^L $e^- (u + \sqrt{2}d)$ $e^+ (\bar{u} + \sqrt{2}\bar{d})$	$V_{1/2}^L$ $e^- d$ $e^+ \bar{d}$	$V_{1/2}^R$ $e^- (u + d)$ $e^+ (\bar{u} + \bar{d})$	$\tilde{V}_{1/2}^L$ $e^- u$ $e^+ \bar{u}$
1 1	$\mu N \to eN$ 7.6×10^{-7} 0.016 **H1:0.021**	$\mu N \to eN$ 7.6×10^{-7} 0.016 **H1:0.021**	$\mu N \to eN$ 7.6×10^{-7} 0.021 **H1:0.029**	$\mu N \to eN$ 2.3×10^{-7} 0.009 **H1:0.012**	$\mu N \to eN$ 2.6×10^{-7} 0.009 **H1:0.011**	$\mu N \to eN$ 1.3×10^{-7} 0.005 **H1:0.006**	$\mu N \to eN$ 2.6×10^{-7} 0.006 **H1:0.007**
1 2	$K \to \mu \bar{e}$ 10^{-5} 0.024 **H1:0.030**	$D \to \mu \bar{e}$ 0.04 0.024 **H1:0.030**	$K \to \mu \bar{e}$ 2.7×10^{-7} 0.026 **H1:0.038**	$K \to \mu \bar{e}$ 2.7×10^{-7} 0.011 **H1:0.016**	$K \to \mu \bar{e}$ 1.3×10^{-7} 0.016 **H1:0.025**	$K \to \mu \bar{e}$ 1.3×10^{-7} 0.012 **H1:0.017**	$D \to \mu \bar{e}$ 0.02 0.017 **H1:0.024**
1 3	*	*	$B \to \mu \bar{e}$ 0.008 0.028 **H1:0.039**	V_{ub} 0.004 0.014 **H1:0.019**	$B \to \mu \bar{e}$ 0.004 0.021 **H1:0.032**	$B \to \mu \bar{e}$ 0.004 0.021 **H1:0.030**	*
2 1	$K \to \pi \nu \bar{\nu}$ 10^{-5} 0.021 **H1:0.028**	$D \to \mu \bar{e}$ 0.04 0.021 **H1:0.028**	$K \to \mu \bar{e}$ 2.7×10^{-7} 0.026 **H1:0.039**	$K \to \mu \bar{e}$ 2.7×10^{-7} 0.011 **H1:0.016**	$K \to \mu \bar{e}$ 1.3×10^{-7} 0.009 **H1:0.012**	$D \to \mu \bar{e}$ 1.3×10^{-7} 0.005 **H1:0.006**	$D \to \mu \bar{e}$ 0.02 0.006 **H1:0.008**
2 2	$\mu \to 3e$ 5×10^{-5} 0.057 **H1:0.084**	$\mu \to 3e$ 5×10^{-5} 0.057 **H1:0.084**	$\mu \to 3e$ 1.6×10^{-4} 0.038 **H1:0.064**	$\mu \to 3e$ 1.3×10^{-4} 0.018 **H1:0.030**	$\mu \to 3e$ 8×10^{-5} 0.019 **H1:0.032**	$\mu \to 3e$ 3.7×10^{-5} 0.016 **H1:0.025**	$\mu \to 3e$ 2.5×10^{-5} 0.029 **H1:0.044**
2 3	*	*	$B \to \bar{\mu} e K$ 0.006 0.043 **H1:0.069**	$B \to \bar{\mu} e K$ 0.003 0.021 **H1:0.034**	$B \to \bar{\mu} e K$ 0.003 0.029 **H1:0.053**	$B \to \bar{\mu} e K$ 0.03 0.029 **H1:0.050**	*
3 1	*	*	$B \to \mu \bar{e}$ 0.008 0.031 **H1:0.044**	V_{ub} 0.004 0.015 **H1:0.021**	$B \to \mu \bar{e}$ 0.004 0.009 **H1:0.012**	$B \to \mu \bar{e}$ 0.004 0.009 **H1:0.011**	*
3 2	*	*	$B \to \bar{\mu} e K$ 0.006 0.058 **H1:0.099**	$B \to \bar{\mu} e K$ 0.003 0.029 **H1:0.049**	$B \to \bar{\mu} e K$ 0.003 0.022 **H1:0.035**	$B \to \bar{\mu} e K$ 0.003 0.022 **H1:0.036**	*
3 3	*	*	$\mu \to ee\bar{e}$ 1.6×10^{-4} 0.076 **H1:0.117**	$\mu \to ee\bar{e}$ 1.3×10^{-4} 0.038 **H1:0.058**	$\mu \to ee\bar{e}$ 8×10^{-5} 0.04 **H1:0.067**	$\mu \to ee\bar{e}$ 3.7×10^{-5} 0.04 **H1:0.067**	*

Table 8.3: First row: Most stringent limits from low energy experiments; Second row: ZEUS limits for 1994-2000 ($e^{\pm}$) interactions; Third row: H1 limits for 1998-2000 ($e^{\pm}$) interactions with a total integrated luminosity of 80.8 pb^{-1} for $F = 0$ type LQs. The ZEUS limits are more stringent because they include the 94-97 data as well with a total integrated luminosity of 129.9 pb^{-1}. The cases marked with '$*$' refers to scenarios involving a top quark.

Chapter 9

Conclusions and Future Work

Since the contemporary topic of neutrino mixing suggests the possibility of mixing in the massive leptonic sector, a search for lepton flavour violation (LFV) has been performed for the data collected at HERA between 1998-1999 for e^-p collisions ($\mathcal{L} = 13.8$ pb^{-1}) and between 1999-2000 for e^+p collisions ($\mathcal{L} = 66.0$ pb^{-1}). The main signature for this process is an isolated muon (or tau) and a jet in the final state. Leptoquark (LQ) exchange can be a good candidate for such processes. The LQs considered are based on the Büchmuller-Rückl-Wyler model and a search for muons in the final state has been carried out. At first, initial selections have been applied to reject all non-ep backgrounds such as cosmic, beam-wall and beam-halo muons in addition to unwanted runs when parts of the detector relevant to the analysis were not fully on. A first level selection has been applied to select only events containing processes such as photoproduction, charged current (CC), neutral current (NC), W-decay and lepton pair as background processes which may mimic the signal process. The second level selection has been dedicated to selecting events with *isolated* muons to reject most of the photoproduction, NC and CC events. Finally, tighter cuts have been applied to reject lepton pair events. Since no data events remain after all these selections from both e^-p and e^+p data, limits at 95%

confidence level (CL) on coupling constants and branching ratios with respect to LQ mass have been set for all LQ types with masses below and above the kinematic limit (319 GeV). A similar search has been performed for LQs with masses far beyond the kinematic limit ($\sim$ 1 TeV) at 95% CL and limits have been set on the four fermion interaction term ,$\frac{\lambda_{eq_i}\lambda_{\mu q_i}}{M^2_{LQ}}$, using the high mass approximation (HMA) for combined e^-p and e^+p data ($\mathcal{L} = 80.8$ pb^{-1}). These limits have been compared to ZEUS limits ($\mathcal{L} = 129.9$ pb^{-1}) and low energy experiments.

9.1 Conclusions

A search for LFV mediated by LQs coupling to second generation leptons in e^-p and e^+p collisions has been performed at HERA using a data sample corresponding to an integrated luminosity $\mathcal{L} = 13.8$ and $\mathcal{L} = 66.0$ pb^{-1} collected with the H1 detector at a centre of mass energy $\sqrt{s} = 319$ GeV for e^-p and e^+p collisions respectively. No evidence has been found for LFV in the muon decay channel. Exclusion limits for coupling constants and branching ratios have been set in a LQ mass range of 100 to 400 GeV. Taking a Yukawa coupling constant of electromagnetic strength ($\lambda_{eq} = 0.3$), couplings of scalar (vector) LQs with masses up to 260-280 (270-290) GeV to muons in e^-p collisions and couplings of scalar (vector) LQs with masses up to 275-300 (288-330) GeV in e^+p collisions are excluded.

Exclusion limits at 95% CL on $\frac{\lambda_{eq_i}\lambda_{\mu q_i}}{M^2_{LQ}}$ have been set for masses far beyond the kinematic limit for LQs in contact interactions using a data sample corresponding to an integrated luminosity $\mathcal{L} = 80.8$ pb^{-1} collected for combined e^-p and e^+p collisions. This search covered LQs coupling to different quark generations and was compared to ZEUS results and low energy experiments.

9.2 Future Work

In order to improve the exclusion limits for low mass LQs this search can be combined with the previously published LFV publication [2]. By adding both data samples all HERA I data will be covered for this search. Also, HERA II data can be investigated and added to HERA I data to get more stringent exclusion limits.

For the contact interaction a search of the effect of the mass of the heavy quarks, such as c and b quarks, on the cross section and hence on the limits can be studied. This requires an understanding of the effect of the next to leading order correction to the b quark coupling to the LQ – a detailed process not included in the MC generator used. This might have an effect on the cross section [95]. This is expected from the factor $\ln^{-1}(\frac{Q^2}{\Lambda^2})$ in Eq. 3.22.

9.2.1 Future Potential

If all HERA I data with $\mathcal{L} = 101$ pb^{-1} and the expected HERA II data collected up to 2007 with $\mathcal{L} = 400$ pb^{-1} are included in the limit calculation for the e^+p collisions and assuming no events observed, more stringent limits on the coupling constants for seven LQs in the e^+p collisions can be set. Also including the complementary HERA II e^-p collision data to be collected up to 2007 with $\mathcal{L} = 400$ pb^{-1} and assuming no data candidates, limits on coupling constants for the other seven LQs will be improved.

Exclusion limits for coupling constants are expected to be as follows in a LQ mass range of 100 to 400 GeV. Taking a Yukawa coupling constant of electromagnetic strength, couplings of scalar (vector) LQs with masses up to 340 (400) GeV to muons in e^-p collisions and couplings of scalar (vector) LQs with masses up to 350 (400) GeV in e^+p collisions will be excluded.

Bibliography

[1] H1 Collaboration, *32nd International Conference on High Energy Physics*, **ICHEP04**, August 16, 2004, Beijing.

[2] H1 Collaboration, *A Search for Leptoquark Bosons and Lepton Flavor Violation in e^+p Collisions at HERA*, Euro Phys Jour **C**.

[3] H1 Collaboration; I. Abt *et al., The H1 Detector at HERA*, NIM, **A279**(1989) 217. I. Abt *et al.* [H1 Collaboration], Nucl. Instrum. Meth. A **386** (1997) 310; I. Abt *et al.* [H1 Collaboration], Nucl. Instrum. Meth A **386** (1997) 348.

[4] M. Müller *et al., Construction and performance of a Thin Cylindrical Wire Proportional Chamber with Cathode Pad Readout for the H1 Experiment*, NIM, **A312** (1992) 457.

[5] J. Bürger *et al., The Central Jet Chamber of the H1 Experiment*, NIM, **A279** (1989) 217.

[6] R. K. Bock and A. Vasilescu, *The Particle Detector Briefbook*, Springer (1998).

[7] S. Egli *et al., The Central Inner Z-Drift Chamber of of the H1 Experiment*, NIM, **A283** (1989) 487.

[8] S. Burke *et al., Track finding and Fitting in the H1 Forward Track Detector*, DESY Report, **DESY-95-132**.

[9] H1 Collaboration; I. Abt, *Technical Proposal for the Upgrade of the Backward Region of the H1 Detector*, DESY Internal Report, PRC-93-02.

[10] H1 Calorimeter Group; B. Andrieu *et al., The H1 Liquid Argon Calorimeter System*, NIM, **A336** (1993) 460.

[11] D. Perkins, *Introduction to High Energy Physics*, Addison-Wesley (1987).

[12] H. Wellisch *et al., Hadronic Calibration of the H1 LAr Calorimeter using Software Weighting Technique*, H1 Internal Note, **H1-IN-346 (02/1994)**.

[13] H1 Calorimeter Group; B. Andrieu *et al., Beam tests and Calibration of the H1 Liquid Argon Calorimeter with Electrons*, NIM, **A350** (1994)57.

[14] H1 Calorimeter Group; B. Andrieu *et al., Results from pion Calibration Runs for the H1 Liquid Argon Calorimeter and Comparisons with Simulations*, NIM, **A336** (1993) 499.

[15] H1 SpaCal Group; R. D. Appuhu *et al., The H1 Lead/Scintillating-fibre Calorimeter*, NIM, **A386** (1997) 397.

[16] H1 SpaCal Group; T. Nicholls *et al., Performance of an Electromagnetic Lead/Scintillating-fibre Calorimeter*, NIM, **A374** (1996) 149.

[17] H1 SpaCal Group; R. D. Appuhu *et al., H1 Backward Upgrade with a SPACAL Calorimeter: The Hadronic Section*, DESY Report, **DESY-96-013**.

[18] H1 SpaCal Group; R. D. Appuhu *et al., Hadronic Response and* e/π*-Separation with the H1 Lead/fibre Calorimeter*, NIM, **A382** (1996) 395.

[19] W. Hildesheim *et al., The Plug Calorimeter Users Guide*, H1 Internal Note, **H1-IN-372 (08/1994)**.

[20] J. Ebert, *The H1-Tail Catcher Hardware and Software Performance*, H1 Internal Note, **H1-IN-448 (08/1995)**.

[21] H. Itterbeck *et al., Improvement of the Trigger Timing of the H1 Digital Muon System*, H1 Internal Note, **H1-IN-427 (02/1995)**.

[22] H1 Collaboration; T. Ahmed *et al., The H1 Forward Muon Spectrometer*, NIM, **A340** (1994) 304.

[23] J. Heatherington *et al., Studies on the TOF FTDC Data*, H1 Internal Note, **H1-IN-307 (08/1993)**;
J. Heatherington *et al., Analysis of TOP FTDC Data*, H1 Internal Note, **H1-IN-362 (06/1994)**.

[24] H1 Collaboration; *Luminosity Measurement in the H1 Experiment at HERA*, contributed paper to *ICHEP96 Warsaw 1996*, **ICHEP96 pal17-026**.

[25] H. Bethe and W. Heitler, *On the Stopping of Fast Particles and on the Creation of Positive Electrons*, Proc. Roy. Soc. Lond. **A146** (1934) 83.

[26] E. Elsen, *The H1 Trigger and Data Aquisition*, contributed paper to *International Symposium on Electronic Instrumentation in Physics, Dubna 1991*, H1 Internal Note, **H1-IN-262 (01/1993)**. F. Sefkow, *et al, Experience with the First Level trigger of H1*, contributed paper to *The 1994 IEEE Nuclear Science Symposium, Virginia 1994*, H1 Internal Note, **H1-IN-407 (11/1994)**.

[27] J. C. Bizot, *et al., Status of Simulation for a Topological Level 2 Trigger*, H1 Internal Note, **H1-IN-212 (02/1992)**. J. C. Bizot, *et al, Strategy Studies for the H1 Topological L2 Triggr (L2TT)*, H1 Internal Note, **H1-IN-508 (01/1997)**.

[28] J. H. Köhne, *et al., Realization of a Second Level Network Trigger for the H1 experiment at HERA*, H1 Internal Note, **H1-IN-509 (01/1997)**.

[29] H1 Collaboration, S. Aid *et al., Guide to Simulation Program, H1SIM*, H1 Internal Report (1995).

[30] R. Burn *et al., GEANT3 User's Guide*, **CERN-DD/EE-84-1**.

[31] H1 Collaboration, S. Aid *et al, H1REC - H1 Reconstruction Program*, H1 Internal Report (1995).

[32] B. Povh, K. Rith, C. Schloz and F. Zetsche; *Particles and Nuclei*, Springer (1999).

[33] Super-Kamiokande Coll., Y. Fukuda et al., Phys. Rev. Lett. **81** (1998) 1562.

[34] R. Eisberg, R. Resnick; *Quantum Physics of Atoms, Molecules, Solids, Nuclei and Particles*, Wiley (second edition).

[35] E. D. Bloom et al., *High Energy Inelastic ep scattering at* 6° *and* 10°, Phys. Rev. Lett. **23** (1969) 930.

[36] M. Breidenbach et al., *Observed Behaviour of Highly Inelastic Electron-Proton scattering*, Phys. Rev. Lett. **23** (1969) 935.

[37] J. D. Bjorken and E. Paschos, *Inelastic Electron-Proton and γ-Proton Scattering and the Structure of the Nucleon*, Phys. Rev. **185** (1969) 1975.

[38] R. Feynman, *Very High Energy Collisions of Hadrons*, Phys. Rev. Lett. **23** (1969) 1415.

[39] B. Heinemann, *Measurement of Charged Current and Neutral Current Cross Sections in Positron-Proton Collisions at $\sqrt{s} \approx 300\ GeV$*, Dissertation, Fach-Bereich Physik der Universität Hamburg (1999).

[40] U. F. Katz, *Deep Inelastic Positron-Proton Scattring in the High Momentum Transfer Regime of HERA*, Springer Tracts in Modern Physics, Vol. 168. Springer, Berlin, Heidelberg 2000.

[41] H1 Collaboration; *et al, Measurement and QCD Analysis of Neutral and Charged Current Cross Sections at HERA*, Eur. Phys. **J. C.**.

[42] BCDMS Collaboration; A. C. Benevenuti *et al, Test of QCD and a Measurement of* λ *from Scaling Violations in the Proton Structure Function* $F_2(x,Q^2)$ *at High* Q^2, Phys. Lett. **B223** (1989) 485.

[43] NMC Collaboration; P. Amaudruz *et al, Proton and Deuteron* F_2 *Structure Functions in Deep Inelastic Muon Scattering*, Phys. Lett. **B295** (1992) 159;
NMC Collaboration; M. Arneodo *et al, Measurement of the Proton and the Deuteron Structure Functions,* F_2^p *and* F_2^d, Phys. Lett. **B364** (1995) 107.

[44] J. D. Bjorken *et al, Inequality for Backward Electron-Nucleon Scattering at High Momentum Transfer*, Phys. Rev. **163** (1967) 1767.

[45] H1 Collaboration; S. Aid *et al, A Direct Determination of the Gluon Density in the Proton at Low* x, Nucl. Phys. **B449** (1995) 3.

[46] G. Altarelli and G. Parisi, *Asymptotic Freedom in Parton Language*, Nucl. Phys. **B126** (1977) 298.

[47] R. Devenish and A. Cooper-Sarkar; *Deep Inelastic Scattering*, Oxford University Press (2004).

[48] Y. L. Dokshitzer, *Calculation of the Structure Functions for Deep Inelastic Scattering and* e^+ *and* e^- *Annihilation by Perturbation Theory in Quantum Chromodynamics*, Sov. Phys. JETP **46** (1977) 641;
V. N. Gribov and L. N. Lipatov, *Deep Inelastic ep Scattering in Perturbation Theory*, Sov. J. Nucl. Phys. **15** (1972) 438 and 675.

[49] E. L. Kuraev, L. N. Lipatov and V.S. Fadin, *The Pomeranchuk Singularity in Non-Abelian Gauge Theories*, Sov. Phys. JETP **45** (1977) 199;
I. I. Balitsky and L. N. Lipatov, *The Pomeranchuk Singularity in Quantum Chromodynamics*, Sov. J. Nucl. Phys. **28** (1978) 822.

[50] H1 Collaboration; C. Adloff *et al, Measurement of Di-jet Cross Sections in Photoproduction and Photon Structure*, Phys. Lett. **B483** (2000) 36.

[51] K. P. Jungmann, *Particle Physics and Cosmology: Proceedings*, ed. J.F. Nieves, in AIP Conference Proceedings, Vol. 444, Amer. Inst. Phys., 1998.

[52] R. E. Marshak, *Conceptual Foundations of Modern Particle Physics*, World Scientific, Singapore, 1993.

[53] T. B. Cheng and L.F. Li, *Gauge Theory of Elementary Particle Physics*, Clarendon Press, Oxford, 1984.

[54] Particle Data Group (PDG), *Particle Physics Booklet*, CERN (2004).

[55] J. L. Feng, *et al.*, *Prospects for indirect detection of neutrino dark matter*, Preprint MIT CTP 3066 **hep-ph/0101122** (2001).

[56] Z. K. Silagadze, Preprint **hep-ph/9907328** (1999).

[57] R. Kitano Phys. Lett. **B481** (2000) 39.

[58] W. Buchmüller, R. Rückl and D. Wyler, *Leptoquarks in Lepton-Quark Collisions*, Phys. Lett. **B191** (1987) 442.

[59] R. Kerger, *A Search for Lepton Flavor Violating Transitions* $e \leftrightarrow \tau$ *via Leptoquarks in* $e^{\pm}$ *Scattering with the Zeus Detector at HERA*, Thesis submitted to Universität Bonn (March 2001).

[60] K. Rosenbauer, *Suche nach Leptoquarks und Leptogluonen im H1-Experiment bei HERA*, Dissertation RWTH Aachen (in German), PITHA 95/16, July 1995.

[61] H.L. Lai *et al.* [CTEQ collaboration], Eur. Phys. J. C **12** (2000) 375 [hep-ph/9903282].

[62] B. Leissner, *Muon Pair Production in Electron-Proton Collisions*, Ph.D. Thesis, RWTH Aachen (2000).

[63] The H1 OO Group, *The H1 OO Physics Analysis Project*, (available on the H1 web page), Sep. 2004.

[64] T. Abe, GRAPE-Dilepton (Version 1.1): A generator for dilepton production in *ep* collisions, Comput. Phys. Commun. **136** (2001) 126 [hep-ph/0012029].

[65] S. Baranov *et. al., LPAIR: A Generator for Lepton Pair Production*, proceedings of the workshop *Physics at HERA, Vol.3*, eds W. Buchmüller, G. Ingelman, DESY (1983) 347.

[66] H. Jung, *The Monte Carlo Generator EPJPSI for J/ψ Mesons in High Energy Electron Proton Collisions*, proceedings of the workshop *Physics at HERA, Vol.3*, eds W. Buchmüller, G. Ingelman, DESY (1991) 1488. (*www-h1.desy.de/ jung/epjpsi.html*).

[67] T. Sjöstrand, PYTHIA 5.7, CERN-TH-6488 (1992), Comp. Phys. Comm. **82** (1994) 74.

[68] G. Ingelman, J. Rathsman and G. A. Schuler, *AROMA 2.2: A Monte Carlo Generator for Heavy Flavor Events in ep Collisions*, Comput. Phys. Commu. **101** (1997) 135. [hep-ph/0012029].

[69] H. Jung, Hard diffractive scattering in high-energy *ep* collisions and the Monte Carlo generator RAPGAP, Comput. Phys. Commun. **86** (1995) 147; RAPGAP program manual (1998) unpublished [http://www-h1.desy.de/∼jung/RAPGAP.html].

[70] G.A. Schuler and H. Spiesberger, DJANGO 2.1, Proc. of the Workshop “Physics at HERA” (1991), Eds. W. Buchmüller and G. Ingelman, Vol. 3, p. 1419.

[71] C. Diaconu *et al., H1EPVEC – $W^{\pm}$ and Z Production Monte Carlo Generator Based on EPVEC*, CPPM Marseille (1999).

[72] K. P. O. Diener, C. Schwanenberger and M. Spira, *Photoproduction of W Bosons at HERA; Reweighting Method for Implementing QCD Corrections in Monte Carlo Programs*, **hep-ex/0302040**;

K. P. O. Diener, C. Schwanenberger and M. Spira, *Photoproduction of W Bosons at HERA; QCD Corrections*, **C25** (2002) 405;

P. Nason, R. Rückl and M. Spira, *A Note on W Boson Production at HERA*, J. Phys. **G25** (1999) 1434;

M. Spira, *W Boson Production at NLO*, contributed paper to *Workshop on Monte Carlo Generators for HERA Physics, Hamburg 1998*, **hep-ex/9905469**.

[73] V. Andreev *et al.* [H1 Collaboration], *Isolated electrons and muons in events with missing transverse momentum at HERA*, Phys. Lett **B651** (2003) 241;

D. South, *Events with Isolated Leptons and Missing Transverse Momentum in e^+p Collisions at HERA*, PhD Thesis, University of Manchester (2003).

[74] I. Negri *et al., A Minimal Comprehensive Set of Muon Background Topological Finders for High P_T Physics Analysis*, H1 Internal Notes, **H1-IN-498 (10/1996)**;

E. Chabert *et al., QBGFMAR: An Updated PHAN Package for Cosmic and Hello Muon Topological Rejection in High P_T Physics Analysis*, H1 Internal Notes, **H1-IN-556 (10/1998)**.

[75] P. Bruel, *Recherche d'interactions au-delà du Modèle Standard à HERA*, PhD Thesis, Orsay (1998).

[76] H1 Collaboration, C. Adloff *et al., Diffractive Dissociation in Photoproduction at HERA*, Z. Phys. **C74** (1997) 221.

[77] J.M. Butterworth, J.P. Couchman, B.E. Cox, B.M. Waugh, KTJET: A C++ implementation of the k-perpendicular clustering algorithm, Comput. Phys. Commun. **153** (2003) 85 [hep-ph/0210022].

[78] H1 Collaboration, C. Adloff *et al., Measurement of Neutral Current and Charged Current Cross-Section in Positron-Proton Collisions at Large Transverse Momentum Transfer*, Eur. Phys. J. **C13** (2000) 609.

[79] L. Goerlich and H. P. Wellisch, *Documentation of the LAr Clustering*, H1 Internal Notes, **H1-IN-204 (12/1991)**.

[80] C. Adloff *et al.* [H1 Collaboration], *A Search for Leptoquark Bosons in ep Collisions at HERA*, Int. Europhysics Conf. on High Energy Physics, Jul 17-23, 2003, Aachen, Abstract 105, Parallel Session 13 .

[81] J. Dingfelder, *A Search for Anomalous Production of Single Top Quarks with the H1 Experiment at HERA*, Dissertation, Universität Heidelberg (2003).

[82] Matti Peez, Private Communication.

[83] T. Junk, *Confidence Level Computation for Combining Searches with Small Statistics*, Nucl. Instrum. Meth. A **434** (1999) 435.

[84] The LEP Working Group for Higgs Boson Searches, *Search for Standard Model Higgs Boson at LEP*, Submitted to Phys. Lett. B, CERN-EP/2003-011 (2003).

[85] R. Barlow, *Statistics*, Manchester Physics Series, J. Wiley and Sons, Chichester (England).

[86] A. L. Read *Optimal Statistical Analysis of Search Results Based on the Likelihood Ratio and its Application to the Search for the MSSM Higgs Bosons at* $\sqrt{s} = 161$ *and 172 GeV*, DELPHI 97-158 PHYS 737, 1997.

[87] ZEUS Collaboration, *Search for Lepton-Flavor violation in ep collisions at HERA*, Submitted to the XXXIst International Conference on High Energy Physics 24-31 July 2002, Amsterdam, The Netherlands.

[88] CDF Collaboration, F. Abbe *et al.*, *Search for Second Generation Leptoquarks in the Dimuon Plus Dijet Channel of* $\bar{p}p$ *Collisions at* $\sqrt{s} = 1.8\ TeV$, Phys. Rev. Lett. **B 81**, 4806 (1998).

[89] D0 Collaboration, F. Abbott *et al.*, *Search for Second-Generation Leptoquark Pair in* $\bar{p}p$ *Collisions at* $\sqrt{s} = 1.8\ TeV$, Phys. Rev. Lett. **B 84**, 2088 (2000).

[90] OPAL Collaboration, M. Z. Akrawy *et al.*, *A Search for lepton flavour violation in Z° decays*, Phys. Lett. **B 254**, 293 (1991);

OPAL Collaboration, G. Abbiendi *et al.*, *Search for lepton flavour violation in e^+e^- collisions at $\sqrt{s} = 189 - 209$ GeV*, Phys. Lett. **B 519**, 23 (2001).

[91] S. Davison, D. Bailey and B.A. Campell, *Model independent constraints on leptoquarks from rare processes* , Z. Phys. C **61**, 613 (1994).

[92] CLEO Collaboration, A. Bornheim *et al.*, *Search for the Lepton-Flavor-Violating Leptonic $B^\circ \to \mu^\pm\tau^\mp$ and $B^\circ \to e^\pm\tau^\mp$*, Phys. Rev. Lett. **93**, 241802 (2004).

[93] E. Gabrielli, *Model-independent constraints on leptoquarks from rare μ and τ lepton processes*, Phys. Rev. **D** 62, 055009 (2002).

[94] Particle Data Group, D.E. Groom *et al.*, Eur. Phys. **J. C. 15**, 1 (2002).

[95] Emmanuelle Perez, Private Communication.

Acknowledgements

I would like to thank my supervisor, Robin Marshall, who introduced me to the research at H1 in the first place. Also, special thanks to Fred Loebinger for his continuous help from the first day in the department.

The UK group in H1: Andrew Mehta, Andrew Rimmer, Aweys Mohammed, Carl Gwilliam, Christian Veelken, Dan Traynor, Dave South, Eram Rizvi, Matthew Beckingham, Nick Malden, Oliver Henshaw, Paul Laycock, Paul Newman and Yves Fleming all helped me a lot to commence the analysis, continue and finish it. Thanks to Dave for his help using the basics of his code, to Nick for his care from the first minute up to the last minute and Christian for spending fascinating hours discussing physics.

My great thanks to the referees for this analysis: Ulrich Martyn and Matti Peez.

The work could not be achieved without the help of Stefan Schmitt and Linus Lindfeld for the time they spent in fruitful discussions related to this analysis.

A special thank to Emmanuelle Perez who devoted her time to explain the basics of the leptoquark interaction and LFV and that she provided her code for me to continue the work.

Johannes Haller and Anja Vest deserve a lot of thanks for their help in limit calculations.